

# Simulating AGN-inflated bubbles with anisotropic viscosity on a moving mesh

Oliver Franke

Institute of Physics and Astronomy  
University of Potsdam

A thesis submitted for the degree of  
Master of Science  
in Astrophysics



Supervisor:

Prof. Dr. Christoph Pfrommer  
University of Potsdam, Institute of Physics and Astronomy  
Cosmology and High-energy Astrophysics, AIP, An der Sternwarte 16, 14482 Potsdam, Germany

Co-Supervisor:

Prof. Dr. Martin Pohl  
University of Potsdam, Institute of Physics and Astronomy  
Theoretical Astroparticle Physics, DESY, Platanenallee 6, 15738 Zeuthen, Germany

Potsdam, August 20, 2020



# Abstract

Feedback of the active galactic nucleus (AGN) to the ambient intracluster medium (ICM) leads to complex structures in the center of a galaxy cluster and is of crucial importance for solving the cooling-flow problem. Dynamics of AGN-inflated underdense bubbles provide an important source of heating as they buoyantly rise through the cluster atmosphere. The evolutionary effects and heating of the ICM thereby critically depend on the bubble morphology. Ideal inviscid hydrodynamical simulations cannot reproduce the observed coherent morphology, because the artificial bubbles become unstable to Rayleigh-Taylor instability (RTI) and Kelvin-Helmholtz instability (KHI) and dissolve into the ICM on much shorter time-scales than their observed lifetimes. Therefore, additional physics have been considered to be important to preserve the bubble stability, including magnetic fields and viscosity. Since the ICM is a weakly collisional, magnetized plasma, where the collision mean free path of the ions is much larger than their Larmor radius, microscopic transport of momentum and heat becomes highly anisotropic. Hence, we perform Braginskii-magnetohydrodynamic simulations in an isothermal cluster core employing the moving-mesh code *AREPO* while applying adaptive mesh refinement. For the first time, we quantify parallel viscous heating rates of buoyantly rising bubbles to clarify whether viscous heating can offset radiative cooling and study the significance of Braginskii viscosity on the bubble dynamics. We show that Braginskii viscosity mainly suppresses RTI and KHI parallel to the magnetic field lines, while having minor effects on modes perpendicular to the field. We find that anisotropic viscous dissipation of turbulent motions is not very efficient in heating the ICM in a volume filling fashion. Since the viscous heating rate is sensitive to pressure anisotropy, it can be suppressed if microscopic plasma instabilities are triggered, which pin the pressure anisotropy down to certain limits for marginal stability. Simulating cluster atmospheres with magnetic fields having  $\beta = 100$  reveals an invariance in bubble evolution in terms of mixing efficiency and viscous heating rates regardless of whether pressure anisotropy is limited or not. If so, micro-scale instabilities are rarely triggered effectively resulting in unsuppressed Braginskii viscosity. If however the magnetic tensions are negligibly weak ( $\beta = 10^6$ ) the bubble evolution is drastically altered depending on whether the pressure anisotropy is bounded within levels of marginal stability. If so, viscous stresses are highly suppressed by the microinstabilities such that they can no longer prevent the bubbles from disruption, resembling the inviscid case.

## Zusammenfassung

Die Rückkopplung eines aktiven galaktischen Kerns (AGN) zum umgebenen Intracluster-Medium (ICM) führt zu komplexen Strukturen im Zentrum eines Galaxienhaufens und ist von wesentlicher Bedeutung um das Abkühlungsfluss -Problem zu lösen. Die Dynamiken von AGN-aufgeblähten Blasen geringer Dichte stellen eine wichtige Quelle zur Wärmeentwicklung bereit, während diese in der Atmosphäre des Haufens auftreiben. Dabei hängen die evolutionären Effekte und das Erwärmen des ICMs kritisch von der Gestalt der Blase ab. Ideale, nicht-viskose, hydrodynamische Simulationen können die beobachtete, einheitliche Form nicht reproduzieren, weil die synthetischen Blasen aufgrund von Rayleigh-Taylor (RTI) und Kelvin-Helmholtz Instabilität (KHI) gestört werden und sich bereits innerhalb von Zeitskalen kleiner als ihre beobachtete Lebensdauer im ICM auflösen. Daher werden zusätzliche physikalische Eigenschaften angenommen, unter anderem Magnetfelder und Viskosität, um die Blasenstabilität zu gewährleisten. Da das ICM ein schwach kollisionsgetriebenes, magnetisches Plasma ist, wo die mittlere freie Weglänge zwischen Ionenkollisionen viel größer ist als deren Larmorradius, werden der mikroskopische Transport von Impuls und Wärme anisotropisch. Darum führen wir Braginskii-magnetohydrodynamische Simulationen in einem isothermischen Clusterkern aus unter Einsatz des dynamischen Meshcodes *AREPO* und Anwendung einer adaptiven Meshverfeinerung. Erstmalig quantifizieren wir viskose Wärmeraten von aufreibenden Blasen um zu klären, ob viskose Erwärmung das Abkühlen durch Strahlung ausgleichen kann und um heraus zu finden, welche Signifikanz Braginskii-Viskosität auf die Blasendynamiken hat. Wir zeigen, dass Braginskii-Viskosität vorrangig RTI und KHI entlang der Magnetfeldlinien unterdrückt, jedoch verschwindenden Einfluss auf die Moden senkrecht zum Feld hat. Wir stellen fest, dass anisotropische, viskose Dissipation von turbulenten Bewegungen nicht sehr effizient ist, um das ICM in einer volumenfüllenden Weise zu erwärmen. Da die viskose Wärmerate stark mit der Druckanisotropie korreliert, kann diese unterdrückt werden, sobald mikroskopische Plasmainstabilitäten getriggert werden, welche wiederum die Druckanisotropie auf bestimmte Grenzen der Randstabilität festsetzen. Die simulierten Clusteratmosphären mit Magnetfeldern der Stärke  $\beta = 100$  zeigen eine Invarianz der Blasenevolution auf bezüglich der Vermischungseffizienz und der viskosen Wärmeraten unabhängig des Falles, ob die Druckanisotropie begrenzt gehalten wurde oder nicht. Gesetzt diesen Fall, werden die mikroskopischen Instabilitäten nur sehr selten getriggert, was effektiv in eine nicht unterdrückte Braginskii-Viskosität resultiert. Falls die magnetischen Kräfte allerdings vernachlässigbar schwach sind ( $\beta = 10^6$ ), wird die Blasenentwicklung drastisch verändert, je nachdem ob die Druckanisotropie innerhalb der Randstabilität begrenzt wurde. Dies vorausgesetzt, werden die viskosen Spannungen stark unterdrückt und können nicht länger verhindern, dass die Blasen zerrissen werden, was wiederum den nicht-viskosen Fall widerspiegelt.

# List of Abbreviations

<b>AGN</b>	active galactic nucleus
<b>AIP</b>	Leibniz Institute of Astrophysics Potsdam
<b>AMR</b>	adaptive mesh refinement
<b>BCG</b>	brightest cluster galaxy
<b>CC</b>	cool-core cluster
<b>CF</b>	cooling flow
<b>CGL</b>	Chew, Goldberger & Law
<b>CR</b>	cosmic ray
<b>DM</b>	dark matter
<b>FR</b>	Fanaroff-Riley
<b>HD</b>	hydrodynamic
<b>HE</b>	hydrostatic equilibrium
<b>IC</b>	initial condition
<b>ICM</b>	intracluster medium
<b>JFM</b>	jet feedback mechanism
<b>KHI</b>	Kelvin-Helmholtz instability
<b>MHD</b>	magnetohydrodynamic
<b>NFW</b>	Navarro-Frenk-White
<b>RTI</b>	Rayleigh-Taylor instability
<b>SMBH</b>	super-massive black hole

# List of Tables

3.1. Fixing physical parameters that characterize the ICM.	37
3.2. Fixing physical parameters that characterize the ICM, continued.	37
3.3. Parameter study of the simulations presented in this thesis.	39
A.1. List of common physical quantities used in this thesis.	83
A.2. List of common physical quantities, continued.	83

# List of Figures

2.1. <i>Left:</i> Deep <i>Chandra</i> X-ray surface brightness map of the Perseus cluster showing its inner 260 kpc in both dimensions. <i>Right:</i> Matched optical image with $H\alpha$ line-emitting filaments around the central giant elliptical galaxy NGC 1275.	11
2.2. Large-scale <i>Chandra</i> final composite residual surface brightness map of the Perseus cluster in the X-ray band.	16
2.3. Sketch how firehose and mirror instabilities emerge by bending the magnetic field lines.	28
2.4. Sketch showing the geometry of the flux calculation.	31
3.1. Radial profiles of our ICs for a uniform magnetic field at $t/t_0 = 0$ .	36
3.2. Projected slices of the $x$ - $y$ midplane for our model $tB2N2$ at $t/t_0 = 0$ with mean magnetic field strength $\ \mathbf{B}\  = 0.5 B_0$ and $\beta = 100$ showing $B_x$ and $B_r$ .	41
3.3. Mass-weighted radial profiles of the initial turbulent magnetic field after rescaling and relaxing the mesh but before setting the bubbles.	41
3.4. Comparison of initial non-relaxed grid with relaxed mesh after applying Lloyd's algorithm.	41
3.5. Slices of the $x$ - $y$ midplane showing the passive scalars and the volume of the grid cells at $t/t_0 = 4$ for the hydrodynamical setup of our highest resolution.	42
4.1. Projected slices of the $x$ - $y$ midplane showing the tracer mass fraction $X_{\text{bub}}$ , the density $\rho$ , the velocity in units of the sound speed $c_s$ , the kinetic-to-thermal pressure ratio $X_{\text{kin}} = P_{\text{kin}}/P_{\text{th}}$ and the magnetic-to-thermal pressure ratio $\beta^{-1} = P_B/P_{\text{th}}$ for our fiducial run $xB6N2$ .	48
4.2. Same quantities as in figure 4.1, but now showing projected slices of the $y$ - $z$ midplane.	49
4.3. Projected slices of the $x$ - $y$ midplane for our fiducial run $xB6N2$ showing from left to right the magnetic energy density, thermal energy density and kinetic energy density normalised to the total energy density.	50
4.4. <i>Left:</i> Evolution of the energy components volume-averaged over time covering the entire spatial domain. <i>Right:</i> Relative energy changes such that $\Delta E(t) = E(t) - E(0)$ .	51
4.5. <i>Left:</i> Mass-weighted gas clumping factor $C_\rho$ averaged over thin radial shells. <i>Right:</i> Volume-integrated dye entropy $S$ as a function of time.	53
4.6. Projected slices of the $x$ - $y$ midplane for our fiducial run $xB6N2$ showing the magnetic field strength in micro Gauss, the plasma beta and the unlimited and limited pressure anisotropy.	55
4.7. Projected slices of the $x$ - $y$ midplane for our fiducial run $xB6N2$ showing the synthetic X-ray surface brightness map, the departure from marginal stability and the parallel viscous heating rate.	57
4.8. Time evolution of the volume-weighted averaged heating and cooling rate in physical units for $xB6N2$ .	58
4.9. Mass-weighted radial profiles of the ratio between heating and cooling rate at specific times.	58
4.10. Projected slices of the $x$ - $y$ midplane showing the tracer mass fraction $X_{\text{bub}}$ for several models including from left to right <i>hydro</i> , $xB6N2lim$ , $xB6N3$ and the fiducial run $xB6N2$ .	60
4.11. Volume-integrated dye entropy $S$ as a function of time, normalised by the maximum entropy $S_{\text{max}}$ .	60
4.12. Projected slices of the $x$ - $y$ midplane showing $\Delta p$ , $\text{fp}$ and $Q^+$ for $xB6N2lim$ and $xB6N3$ .	62
4.13. Projected slices of the $x$ - $y$ midplane showing $X_{\text{bub}}$ , $I_X$ , $\ (\nabla \times v)\ $ , $\beta$ and $B \mu G$ for run $xB6N2iso$ .	64
4.14. Projected slices of $tB2N2lim$ alternating between the $x$ - $y$ and the $y$ - $z$ midplane showing $X_{\text{bub}}$ , $I_X$ and $\ (\nabla \times v)\ $ .	65
4.15. Projected slices of $xB2N2lim$ alternating between the $x$ - $y$ and the $y$ - $z$ midplane showing $B \mu G$ , $\Delta p$ and $\text{fp}$ .	67
4.16. Projected slices alternating between the $x$ - $y$ and the $y$ - $z$ midplane showing $Q^+$ for $xB2N2$ and $xB2n2lim$ .	68
4.17. Time evolution of the volume-weighted averaged heating and cooling rate in physical units for $xB2N2$ and $xB2n2lim$ .	69
4.18. Volume-averaged viscous heating rate and radiative cooling rate for the entire cluster domain as if for each cell $\text{fp} = 8\pi\Delta p_{\text{lim}}/B^2$ .	69
4.19. Projected slices of $tB2N2lim$ alternating between the $x$ - $y$ and the $y$ - $z$ midplane showing $X_{\text{bub}}$ , $I_X$ and $v/v_0$ .	70
4.20. Projected slices of the $x$ - $y$ midplane of $tB2N2lim$ showing $B \mu G$ , $\beta$ , $\ (\nabla \times v)\ $ , $\Delta p$ , $\text{fp}$ and $Q^+$ .	72
4.21. Time evolution of the volume-weighted averaged heating and cooling rate in physical units, restricted to cells with vorticity levels exceeding $\ (\nabla \times v)\  > 5 t_0$ .	72
4.22. Percentage change in $E_{\text{tot}}$ and $M_{\text{tot}}$ over time.	73
4.23. Convergence test plotting $E_{\text{kin}}$ and $\langle v_y \rangle_M$ for each of our hydrodynamic resolutions.	74
4.24. Projected slices of the $x$ - $y$ midplane showing $X_{\text{bub}}$ for each of our hydrodynamic resolutions.	75
4.25. Volume covering fraction of a given tracer mass fraction for each of our numerical resolutions at $t/t_0 = 8$ .	76
A.1. Low resolution simulations of the <i>hydro</i> model showing different values of the smoothing parameter $a$ .	83

# Contents

<b>Abstract</b>	I
<b>List of Abbreviations</b>	III
<b>List of Tables</b>	III
<b>List of Figures</b>	IV
<b>Contents</b>	VI
<b>1. Introduction</b>	7
<b>2. Theoretical Background</b>	9
2.1. Galaxy Clusters . . . . .	9
2.1.1. Properties in the optical window . . . . .	9
2.1.2. Properties in the X-Ray window . . . . .	10
2.1.3. Modelling the X-ray emission . . . . .	11
2.1.4. Dark matter halos . . . . .	12
2.1.5. Cooling Flow Problem . . . . .	13
2.2. AGN feedback . . . . .	15
2.2.1. Jet-inflated bubble properties . . . . .	15
2.2.2. Bubble stability . . . . .	16
2.2.3. Cavity power . . . . .	17
2.2.4. Heating by AGN feedback . . . . .	19
2.2.5. Other Heating Mechanisms . . . . .	19
2.3. Plasma Physics . . . . .	21
2.3.1. Plasma Parameters . . . . .	21
2.3.2. ICM as a weakly collisional plasma . . . . .	22
2.3.3. Turbulence . . . . .	23
2.3.4. Reynolds Number . . . . .	24
2.3.5. Braginskii-MHD . . . . .	25
2.3.6. Micro-scale Instabilities . . . . .	27
2.4. AREPO . . . . .	30
2.4.1. Braginskii Module . . . . .	32
<b>3. Methods</b>	35
3.1. Model Setup . . . . .	35
3.1.1. Magnetic Field Configuration . . . . .	39
3.2. Initial Conditions . . . . .	40
3.2.1. Mesh Relaxation . . . . .	40
3.2.2. Passive Scalars and Refinement Criteria . . . . .	42
3.2.3. Boundary Conditions . . . . .	43
<b>4. Analysis</b>	45
4.1. Bubble Evolution . . . . .	45
4.1.1. Energy Content . . . . .	49
4.1.2. Mixing . . . . .	51
4.1.3. Cooling and Heating . . . . .	53
4.2. Uniform $\mathbf{B}$ , $\beta = 1e6$ . . . . .	59
4.2.1. Parameter Study - Reducing and Limiting $\eta$ . . . . .	59
4.2.2. Isotropic Viscosity . . . . .	63
4.3. Uniform $\mathbf{B}$ , $\beta = 100$ . . . . .	65
4.4. Turbulent $\mathbf{B}$ , $\beta = 100$ . . . . .	70

4.5. Sanity Check and Convergence Test . . . . .	73
<b>5. Discussion</b>	<b>77</b>
5.1. Effective Reynolds Number . . . . .	78
5.2. Limitations . . . . .	79
<b>6. Conclusions and Future Perspective</b>	<b>81</b>
<b>A. Supplementary Figures</b>	<b>83</b>
<b>B. Bibliography</b>	<b>84</b>
<b>Statement of Academic Integrity</b>	<b>93</b>

# Chapter 1.

## Introduction

Deep images of *Chandra* and *XMM-Newton* observations of galaxy clusters have revealed complex structures in their cores such as cavities in X-ray surface brightness maps (Birzan et al., 2004). These cavities are inflated by the interaction of powerful radio jets, which are driven by an accreting super-massive black hole (SMBH) in the central brightest cluster galaxy (BCG), with the ambient intracluster medium (ICM) (Worrall, 2009). The ICM is a diffuse, hot plasma, which radiates thermal bremsstrahlung in X-rays (Voit, 2005) on time-scales considerably shorter than the Hubble time in the very centers of then so-called cool-core clusters (CCs) (Fabian and Sanders, 2007). Such expected cooling flows are not observed in form of significant levels of star formation (Peterson and Fabian, 2006). Feedback of the active galactic nucleus (AGN) to the ICM might be the most promising mechanism for solving the cooling flow problem in CCs (McNamara and Nulsen, 2012). Dynamics of AGN-inflated underdense, high entropy bubbles provide an important source of heating as they buoyantly rise through the cluster atmosphere (Fabian, 2012), because inferred heating rates are capable of balancing radiative cooling of the ICM (Rafferty et al., 2006). Numerical simulations of AGN feedback have been used in order to study the underlying physics needed to reproduce the observed evolution of buoyant bubbles (Soker, 2016; Ehlerl et al., 2018). Such bubbles, like the northwest cavity of the Perseus cluster, remain coherent and avoid being shredded by Rayleigh-Taylor instability (RTI) and Kelvin-Helmholtz instability (KHI) over the bubble lifetime,  $\lesssim 100$  Myr (Fabian et al., 2011). However, ideal inviscid hydrodynamical simulations cannot reproduce the observed morphology as the bubbles become unstable to RTI and KHI and dissolve into the ICM on much shorter time-scales (Scannapieco and Brüggen, 2008; Brüggen and Scannapieco, 2009). Therefore, additional physics have been considered to be important to preserve the bubble stability, including magnetic fields (Ruszkowski et al., 2007; Dursi and Pfrommer, 2008), viscosity (Reynolds et al., 2005; Gardini, 2007) or both (Dong and Stone, 2009; Kingsland et al., 2019).

Since the ICM is weakly magnetized (Carilli and Taylor, 2002), a magnetohydrodynamical (MHD) description of the plasma might be inevitable. Ideal MHD simulations with simplistic field topologies show that buoyant bubbles can be sufficiently stabilized suppressing fluid instabilities at the interface if the magnetic field lines are aligned parallel to the bubble surface (O'Neill et al., 2009; Dong and Stone, 2009). Real cluster atmospheres however likely contain a turbulent magnetic field (Schekochihin and Cowley, 2007), which enhances mixing of bubble material with the ambient gas compared to a quiescent ICM. Hence, viscous effects might also be important for the bubble dynamics, which is also indicated by the low estimates of the Reynolds number of the intracluster gas,  $Re \approx 50\text{-}100$ , if assuming the standard Spitzer coefficient of viscosity (Spitzer, 1962). Although hydrodynamical simulations including viscosity show that viscous stresses can quench the growth rates of RTI and KHI perturbations and maintain the observed bubble morphology (Reynolds et al., 2005), these studies suffer from the simplified assumption that momentum transport in the ICM is isotropic. In fact, the ICM is a weakly collisional, magnetized plasma, where the collision mean free path of the ions is much larger than their Larmor radius (Kunz et al., 2012). Thus, microscopic transport of momentum and heat becomes highly anisotropic as the ions are basically tied to the magnetic field lines and are only scattered in between at each Coulomb collision. To account for these fundamental property changes, ideal MHD is extended by anisotropic heat conduction and viscosity to become so-called Braginskii-MHD (Braginskii, 1965).

So far, there have not been many studies of AGN-inflated buoyant bubbles including the effects of Braginskii-MHD. [Dong and Stone \(2009\)](#) considered Braginskii viscosity along magnetic field lines and studied the dynamics and lifetimes of initially static bubbles depending on different (uniform) field topologies. They find that models using isotropic versus anisotropic viscosity produce quite different results. The latter only suppresses RTI and KHI parallel to the magnetic field lines on macroscopic scales, while having minor effects on interchanging modes perpendicular to the field. [Kingsland et al. \(2019\)](#) studied anisotropic viscosity of self-consistently jet-inflated cavities in a turbulent environment. They find that the evolutionary dynamics drastically depend on whether the anisotropic viscous dissipation of momenta is suppressed by plasma instabilities on microscopic scales. Such microinstabilities are triggered where pressure anisotropies caused by turbulent stresses and concomitant changes in magnetic field strength exceed certain thresholds for marginal stability ([Schekochihin et al., 2005](#)). If the production of pressure anisotropy is pinned down to these limits, which is motivated from kinetic theory ([Rosin et al., 2011](#)), effects due to Braginskii viscosity might also be limited and considerably overestimated otherwise ([Schekochihin et al., 2008](#)).

The two previous simulation studies by [Dong and Stone \(2009\)](#) and [Kingsland et al. \(2019\)](#) did not estimate the parallel viscous heating rates arising from the pressure anisotropy with respect to the local direction of the magnetic field. As theoretical studies find, viscous heating is assumed to be comparable with radiative bremsstrahlung cooling in a weakly collisional, magnetized ICM ([Kunz et al., 2011](#)). Furthermore, this heating-cooling balance is thermally stable in a probably self-regulating manner. Therefore, we study parallel viscous heating as a promising heating mechanism for quenching cooling flows and preventing cluster core collapse. For the first time, in this thesis we estimate viscous heating rates for simulations of buoyantly rising bubbles in a cluster atmosphere. We perform a number of different simulations designed to have comprehensible initial conditions (ICs) with a controllable set of parameters in order to study the significance of pressure anisotropy. This allows us to isolate the effects of Braginskii-MHD in our simulations. Our first set of ICs aims to reproduce the findings of [Dong and Stone \(2009\)](#) by employing the moving-mesh code *AREPO* ([Springel, 2010](#)) while applying adaptive mesh refinement (AMR). Thereby, we study both a weak and a strong magnetic field, and whether pressure anisotropy is limited or unlimited by kinetic instabilities. Our second set of ICs is identical to the first one, now enhanced by introducing a turbulent magnetic field. This allows us to advance to more and more sophisticated cluster properties, while studying the impact of Braginskii viscosity on the bubble dynamics and quantifying whether viscous heating rates can offset radiative cooling rates.

The structure of this thesis is as follows. In chapter 2 we introduce the basic physics of galaxy clusters, AGN-inflated bubbles and the weakly collisional ICM and give an overview of *AREPO*, the numerical code we have used to perform our simulations. We present our numerical setup and describe our treatment of viscosity in chapter 3. The subsequent analysis of our simulations is discussed in chapter 4 including the bubble evolution, the mixing efficiency and estimates of the viscous heating rate for different ICM parameters. We discuss our results in chapter 5 and conclude our findings in chapter 6.

# Chapter 2.

## Theoretical Background

In this chapter we set the fundamental framework needed in order to be able to understand the methods used throughout this thesis and to comprehend our obtained results. We start by describing basic properties of galaxy clusters and segue from the cooling flow problem into AGN feedback and how AGN-inflated bubbles theoretically contribute to solving the cooling catastrophe. In the next section we characterize the physics of the plasma in which the bubbles are inflated into and how anisotropic viscosity enters the Braginskii-MHD equations describing this ICM. The last section gives an overview on the numerical code *AREPO* we have used to compute our set of simulations presented later on.

### 2.1. Galaxy Clusters

#### 2.1.1. Properties in the optical window

Galaxy clusters are the largest gravitationally bound objects in the Universe. They extend out to virial radii of  $R_{200} \sim 1\text{-}3 \text{ Mpc}$  (Peterson and Fabian, 2006), where  $R_{200}$  is the radius at which the mean cluster density equals 200 times the critical density of the universe  $\rho_{\text{crit}}$ . They can have number of member galaxies anywhere from 50 (poor cluster) to several thousand (rich cluster). Cluster galaxies are collisionless tracers of the gravitational potential and its dynamical state. They have to a good approximation a Gaussian velocity distribution with dispersions around  $\sigma_v \approx 1000 \text{ km/s}$  for a rich cluster (Carroll and Ostlie, 2014). For a relaxed cluster, using Maxwell's equipartition theorem, the galaxy dispersion along the line of sight can be related to the temperature of the cluster as  $T \propto \sigma_v^2$  (Voit, 2005).

Approximating the dynamical time-scale of clusters yields  $t_{\text{dyn}} \sim R_G/\sigma_v \approx 1 \text{ Gyr} \ll t_H$ , where  $R_G = GM_{\text{cl}}/\sigma_v^2 \approx 1 \text{ Mpc}$  is the gravitational radius and  $t_H = 1/H_0$  is the Hubble time (Schneider, 2015). The dynamical time-scale is defined as the amount of time it takes for a typical galaxy to traverse the cluster along its diameter. Since  $t_{\text{dyn}}$  is much shorter than the age of the universe, a typical cluster can be assumed to be in dynamical equilibrium. This justifies using the virial theorem for estimating the mass of a typical galaxy cluster, adopting the notation from Pfrommer (2020),

$$2E_{\text{kin}} = -E_{\text{pot}} \Rightarrow M_{\text{gal}}\sigma_v^2 = \frac{GM_{\text{cl}}M_{\text{gal}}}{r_{\text{cl}}} \Rightarrow M_{\text{cl}} \approx 10^{15} M_{\odot} \quad (2.1)$$

In fact, a typical mass range for clusters is  $10^{13}\text{-}10^{15} M_{\odot}$  (Schneider, 2015). However, adding up all the luminous stellar mass within the galaxies only unveils a fraction of the cluster mass ( $M_{\star} = 1/50 M_{\text{cl}}$ ). This was the original technique used by Fritz Zwicky in 1933 to arrive at a large mass-to-light ratio of the Coma cluster ( $M_{\odot}/L_{\odot} \approx 400$ , Zwicky 1933). From this he concluded that clusters must contain considerably more mass than indicated by their individual galaxies, otherwise they would have been dispersed long ago. This discrepancy of the gravitating and luminous mass in galaxy clusters led Zwicky to the postulation of the existence of dark matter. The question arises as to whether the application of the virial theorem is still justified considering that the main fraction of mass is not contained in the luminous galaxies themselves. The mass derivation sketched in equation (2.1) remains valid as long as the spatial distribution of galaxies follows the total mass distribution. If the latter is non-spherical or the velocity distribution of

member galaxies is anisotropic, projection effects need to be considered ([Schneider, 2015](#)).

### 2.1.2. Properties in the X-Ray window

A portion of Zwicky's postulated missing mass was discovered with the Einstein Observatory (HEAO-2) in 1978 ([Giacconi et al., 1979](#)). They revealed that clusters of galaxies contain an intracluster medium (ICM) emitting X-rays from much of the cluster's volume and not just by individual point sources. In fact, galaxy clusters are the brightest, extended extragalactic X-ray emitting sources with luminosities around  $L_X \sim 10^{43}\text{-}10^{45}$  erg/s ([Schneider, 2015](#)). This radiation can be detected throughout the cluster out to several megaparsecs. The ICM can be described as a hot ( $T \sim 10^7\text{-}10^8$  K), dilute ( $n_e \sim 10^{-3}\text{-}10^{-2}$  cm $^{-3}$ ) intracluster gas that is distributed homogeneously and filling the cluster's gravitational potential well ([Schneider, 2015](#)). The observed X-ray spectrum resembles the characteristics for optically thin thermal bremsstrahlung emission. Describing the gas temperature in terms of particle energies,  $k_B T \approx 1\text{-}10$  keV, most of the elements of the ICM are fully ionized, except for recombination lines of highly-ionized metals like iron (Fe XXV at 8.8 keV and Fe XXVI at 9 keV), silicon and neon ([Carroll and Ostlie, 2014](#)). We will neglect the line emissions and treat the ICM further on as a fully ionized, pure hydrogen plasma, where number densities and temperatures ([Hitomi Collaboration et al., 2018](#)) of the electrons and the ions are the same. The emissivity via thermal bremsstrahlung (free-free radiation) is defined as ([Schneider, 2015](#))

$$\epsilon_\nu^{\text{ff}} = \frac{32\pi Z^2 e^6 n_i n_e}{3m_e c^3} \sqrt{\frac{2\pi}{3k_B T m_e}} \exp\left(-\frac{\hbar\omega}{k_B T}\right) g_{\text{ff}}(T, \nu) \propto n^2, \quad (2.2)$$

where  $Ze$  is the electrical charge of the ion species with  $Z = 1$  for hydrogen,  $n_{i,e}$  are the number densities for the ions and electrons,  $T$  is the gas temperature and  $g_{\text{ff}}$  is the Gaunt factor depending on the collision frequency  $\nu$ . The Gaunt factor is usually of order unity in classical physics and only varies from one if quantum effects play an important role ([Dopita and Sutherland, 2003](#)). The remaining quantities are constants with their usual meaning,  $m_e$  is the electron mass,  $c$  is the speed of light,  $k_B$  is the Boltzman constant and  $\hbar$  is Planck's constant, which are also summarized in table A.1. The right-hand side of equation (2.2) clarifies the proportionality of bremsstrahlung emission to be  $\epsilon_\nu^{\text{ff}} \propto n_i n_e = n^2$ . Since these emission processes are collisional, the power radiated per unit volume scales with the number density squared, projection effects by measuring surface brightness become irrelevant. In addition, the gas temperature seems to be a very good measure for the cluster mass, meaning that it is equal to the virial temperature of the cluster potential. We can now estimate the mass for a typical, relaxed galaxy cluster following [Pfrommer \(2020\)](#),

$$E_{\text{th}} = E_{\text{pot}} \Rightarrow \frac{3}{2} k_B T = \mu m_p \frac{GM_{\text{cl}}}{r_{\text{cl}}} \Rightarrow M_{\text{cl}} \approx 10^{15} \text{ M}_\odot, \quad (2.3)$$

where  $m_p$  is the proton mass and  $\mu = 0.5$  is the mean molecular weight for a pure hydrogen plasma. Integrating equation (2.2) over all frequencies and along the line-of-sight through the cluster results in X-ray surface brightness maps, from which the mass density profile can be inferred ([Longair, 2011](#)). Integrating the latter over the cluster volume yields the total gas mass, which is approximately  $M_{\text{gas}} \approx 1/7 M_{\text{cl}}$  ([Voit, 2005](#)). Hence, some of Zwicky's postulated dark matter is found in the form of the hot ICM, observed via its electromagnetic emission by looking at a different waveband. This becomes more clear in figure 2.1, where we compare the observed X-ray and optical images of the Perseus cluster core. Since no significant amounts of the remaining missing matter can be directly seen in any other waveband, this matter must be

non-baryonic, only interacting gravitationally. Summarizing the components of the cluster mass shows, that around 2% is made up of stars, around 13% is due to hot gas and the remaining 85% is contributed by dark matter ([Carroll and Ostlie, 2014](#)).

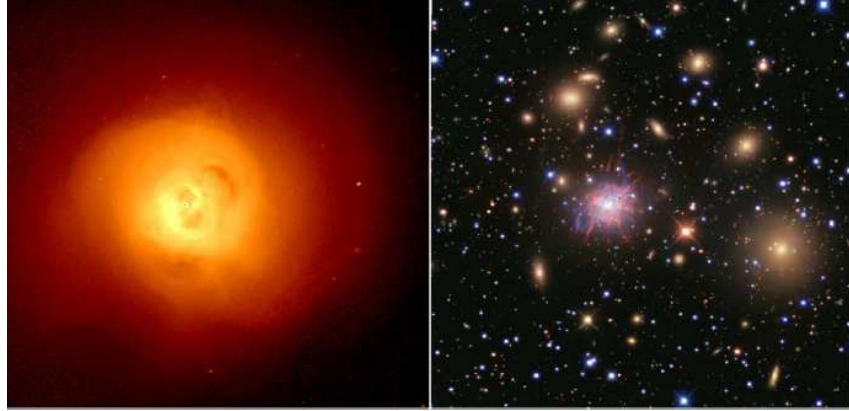


Figure 2.1.: *Left:* Deep *Chandra* X-ray surface brightness map of the Perseus cluster showing its inner 260 kpc in both dimensions. The highly-resolved diffuse X-ray emission reveals bulk gas motions and distinct substructures at the cluster core. Regions of displaced emissivity are called X-ray cavities. *Right:* Matched optical image with  $H\alpha$  line-emitting filaments around the central giant elliptical galaxy NGC 1275. Both figures are taken from [Fabian et al. \(2011\)](#).

### 2.1.3. Modelling the X-ray emission

By using numerical simulations astrophysicists are interested in how to infer the gas and mass distribution of the cluster, which is to model, to match with the properties of the ICM from the observed X-ray radiation. The derivations presented in this section are following [Schneider \(2015\)](#). Consider the adiabatic speed of sound in the cluster gas to be

$$c_s \approx \sqrt{\gamma \frac{p}{\rho_g}} = \sqrt{\gamma \frac{k_B T}{\mu m_p}} \approx 1000 \frac{\text{km}}{\text{s}} \left( \frac{T}{10^8 \text{K}} \right)^{1/2} \quad (2.4)$$

for a typical gas temperature of  $T = 10^8 \text{ K}$ , where  $\gamma = 5/3$  is the adiabatic index,  $p = nk_B T$  is the gas pressure and  $\rho_g = n\mu m_p$  is the gas density. The sound-crossing time of the cluster is thus  $t_{\text{sc}} \approx 2R_G/c_s \approx 1 \text{ Gyr}$ , which is considerably shorter than the lifetime of the cluster, whereas the latter can be approximated by the age of the universe.  $t_{\text{sc}}$  is also roughly the time-scale on which deviations from the pressure equilibrium are evened out. Therefore, the gas can be in hydrostatic equilibrium, under the premise that the last major merger happened longer ago than the sound-crossing time itself and the AGN has not injected energy into the ICM via jet feedback during such a time period (see section 2.2.4). Under these conditions, the galaxy cluster is called to be relaxed. The application of hydrostatic equilibrium requires to assume that the net acceleration  $dv/dt$  of the gas at any point is zero and that we can neglect external forces. The Euler equation for conservation of momentum for an ideal, incompressible fluid then reads

$$\frac{dv}{dt} = -\frac{\nabla p}{\rho_g} + g = 0 \quad (2.5)$$

where  $P$  is the gas pressure,  $\rho_g$  is the gas density and  $g$  is the gravitational acceleration which is related to the gravitational potential  $\Phi$  by  $g = -\nabla\Phi$ . This relation describes how the gravitational force is balanced by the pressure force. In a spherically symmetric case equation (2.5)

becomes

$$\frac{1}{\rho_g} \frac{dp}{dr} = -\frac{d\Phi}{dr} = -\frac{GM(r)}{r^2}, \quad (2.6)$$

where  $M(r)$  is the total mass contained within radius  $r$  from all forms of matter. Plugging in  $p = \rho_g k_B T_g / (\mu m_p)$  from the ideal gas law yields

$$M(r) = -\frac{k_B T_g r^2}{G \mu m_p} \left( \frac{d \ln \rho_g(r)}{dr} + \frac{d \ln T_g(r)}{dr} \right). \quad (2.7)$$

Assuming that the gas temperature is spatially constant, equation (2.7) simplifies using  $T(r) = T_g$ , and the mass profile of the cluster can be determined solely from the density profile of the gas. Considering such an isothermal gas distribution, a commonly used method of fitting the X-ray data is the so called  $\beta$ -model (Cavaliere and Fusco-Femiano, 1976).

$$\rho_g(r) = \rho_{g,0} \left[ 1 + \left( \frac{r}{r_0} \right)^2 \right]^{-3\beta/2} \quad (2.8)$$

Here,  $\rho_{g,0}$  is the central gas density and  $r_0$  is the core radius, the characteristic length scale within which the density profile flattens out. The index  $\beta$  is the ratio of the kinetic energies of tracers of the gravitational potential and the mean thermal energies of the ICM gas particles:  $\beta = \sigma_{\text{gal}}^2 / \sigma_{\text{gas}}^2$ . Using  $\beta \approx 2/3$  is a good fit for the X-ray emission of many clusters (Schneider, 2015). However, especially for cool-core clusters (see section 2.1.5) a better fit for the density distribution is given by the double  $\beta$ -model (Xue and Wu, 2000; Santos et al., 2008).

#### 2.1.4. Dark matter halos

Galaxy clusters form where waves of primordial density fluctuations interfere constructively after the Big Bang (Kravtsov and Borgani, 2012). Most of the clusters mass is contained in form of dark matter (DM), which clumps in dark matter halos. These halos assemble in filamentary structures throughout the universe. According to this hierarchical structure formation model, clusters form at the intersection of these filaments through mergers of smaller groups of galaxies and inflowing gas. The richest clusters are formed the latest and are generally found in the densest regions of the cosmic web (Longair, 2011). The evolution of the cosmic web is highly non-linear and must be modeled by numerical simulations.

The primordial gas collapses following the DM potential. The diffuse and relatively cold-inflowing gas is then accreted and shock-heated. The higher temperature of the gas slows down the gravitational collapse and the gas starts to virialize. Although the gas is heated by the accretion shocks, they alone are not sufficient to reach the observed temperatures of the ICM of about  $10^8$  K. Secondary accretion shocks develop if substructures merge at the inner region of a cluster that was already heated. The collisional shocks propagate through the dense hot gas and heat it to the observed values (Dolag et al., 2008; Ha et al., 2018).

In 1997, Navarro, Frenk & White (NFW) showed that cold dark matter halos in N-body simulations have a universal density profile, well fit by a double power-law (Navarro et al., 1997). This is the so called NFW profile, which is the most popular parametrization model of dark matter halos. Its density profile is given by

$$\rho(r) = \frac{\rho_{\text{crit}} \delta_c}{\frac{r}{r_s} \left( 1 + \frac{r}{r_s} \right)^2}, \quad (2.9)$$

where  $\rho_{\text{crit}} = 3H_0^2/(8\pi G)$  is the critical density of the universe,  $r_s = r_{200}/c$  is the scale radius,  $\delta_c$  is the characteristic overdensity of the halo and  $c$  is the so called concentration, which is higher the earlier halos form.  $H_0$  is the Hubble constant given by  $H_0 = 100h \text{ km/s/Mpc}$ , where  $h$  is the dimensionless Hubble parameter. Beyond radii  $r_s$  the profile falls off  $\propto r^{-3}$  and within  $r_s$  it flattens considerably proportional to  $r^{-1}$ .

The virial radius  $r_{200}$  is enclosing a mean overdensity of 200 times the critical density. This implies for the total halo mass  $M_{200}$  that

$$M_{200} \left( \frac{4\pi}{3} r_{200}^3 \right)^{-1} = 200 \times \rho_{\text{crit}} \quad (2.10)$$

and the mean density of the halo is given as

$$\rho_{\text{halo}} = \frac{M(< r_{200})}{V_{200}} = \frac{\int_0^{r_{200}} 4\pi r^2 \rho(r) dr}{\left( \frac{4\pi}{3} r_{200}^3 \right)}. \quad (2.11)$$

### 2.1.5. Cooling Flow Problem

By modelling the ICM in section 2.1.3, we assumed hydrostatic equilibrium, but neglected that the gas continuously loses internal energy due to its emission. Therefore we need to consider the cooling time-scale  $t_{\text{cool}}$ , defined as the time the gas would need until all of its thermal energy  $E_{\text{th}} = \frac{3}{2}nk_B T$  is radiated away by equation (2.2) (Schneider, 2015),

$$t_{\text{cool}}(r_{200}) = \frac{E_{\text{th}}}{\epsilon^{\text{ff}}} \approx 7.5 \times 10^{10} \text{ yr},$$

where  $\epsilon^{\text{ff}}$  is the emissivity integrated over all frequencies, which is calculated in equation (2.13) below. Hence,  $t_{\text{cool}}(r_{200}) > t_H \approx 13.8 \text{ Gyr}$  is larger than the age of the universe, which allows a hydrostatic equilibrium to be established throughout the cluster. However, since  $\epsilon_{\nu}^{\text{ff}} \propto n^2$ , the density may become sufficiently large in centers of clusters to yield  $t_{\text{cool}} < t_H$  at a certain threshold, where the gas is able to cool quite efficiently. We can estimate the cooling time-scale at the cluster core, normalised to quantities in our ICs (see section 3.1) to

$$t_{\text{cool}}(r_0) \approx 0.96 \times 10^9 \text{ yr} \left( \frac{n}{0.03 \text{ cm}^{-3}} \right)^{-1} \left( \frac{T_g}{3.88 \times 10^7 \text{ K}} \right)^{1/2} \quad (2.12)$$

Therefore, after exceeding the threshold, the hydrostatic equilibrium cannot be maintained in those cluster cores. This means, that the cluster gas has to flow inwards, where it gets compressed. By this, the inflowing masses build a counterpart to the gravitational force due to the increased gas pressure. A new hydrostatic equilibrium is set up with higher core density but lower temperature (Schneider, 2015). But the increased density will further accelerate the described cooling process once again, leading into a cooling catastrophe.

These so-called cooling flows (CFs) have indeed been observed in the centers of massive clusters, in the form of a sharp central peak in X-ray emission. Those clusters are called cool-core clusters (CCs). CCs are characterized by low cooling times  $t_{\text{cool}} \lesssim 1 \text{ Gyr}$  (Hudson et al., 2010; Voigt and Fabian, 2004) and low entropies  $S_0 = k_B T n^{-2/3} \sim 10 \text{ keV cm}^2$  (Voit and Donahue, 2005; Pfrommer et al., 2012) in their inner core radius  $r_0 \sim 10 \text{ kpc}$ . However, the expected high star formation rates and mass deposition rates  $\dot{M}$ , at which the gas should cool and flow inwards due to this cooling, have not been measured observationally on large-scales by *Chandra* or *XMM-Newton* and are significantly overestimated. According to the standard cooling flow model, one also expects to find gas at ever decreasing gas temperatures down to  $T_g \gtrsim 0 \text{ keV}$ . Instead, as

revealed spectroscopically, a minimum temperature seems to exist, below which the gas cannot cool (Peterson et al., 2003). This threshold is usually at one half to one third of the cluster's virial temperature at around 1 keV (Fabian and Sanders, 2007; Blanton et al., 2010).

These findings point to a local heating process, which prevents the gas temperature to fall below a certain threshold, while not dominating the cooling process. In fact one observes a quasi-balance between heating and cooling (McNamara and Nulsen, 2012). Since the cooling floor is kept constant over long periods (Bauer et al., 2005), we are looking for a relatively gentle, quasi-continuous distributed heat source. This is pointing towards a self-regulated feedback loop via active galactic nuclei (AGNs) (see section 2.2.4).

To see how much feedback is needed to counter the cooling catastrophe in the core region, we consider the total X-ray luminosity as a proxy for the cooling luminosity. In order to do that we redefine the volume emissivity  $\epsilon^{\text{ff}}$  as an energy cooling rate by integrating equation (2.2) over all frequencies, which yields

$$\epsilon^{\text{ff}} = \int_0^\infty \epsilon_\nu^{\text{ff}} d\nu = \int_0^\infty \frac{Cn^2}{\sqrt{k_B T}} e^{-h\nu/k_B T} d\nu = Ch^{-1} n^2 \sqrt{k_B T} = \Lambda(T) n^2, \quad (2.13)$$

where  $Ch^{-1}k_B^{1/2}$  is a constant and  $\Lambda(T)$  is a cooling function depending on the temperature of the gas. It is dominated by bremsstrahlung above  $T \sim 1$  keV and by metal lines below  $T \sim 1$  keV. In our isothermal cluster model, we have

$$\Lambda(T) = 8.9 \times 10^{-24} \text{ erg cm}^3 \text{ s}^{-1} \left( \frac{T}{3.88 \times 10^7 \text{ K}} \right)^{1/2}. \quad (2.14)$$

For a more sophisticated cooling function of the ICM, we refer to Kunz et al. (2011) and references therein. Now we can estimate the cooling luminosity  $L_X$  by integrating the cooling rate  $\epsilon^{\text{ff}}$  over the cluster volume assuming spherical symmetry. By following the derivations by Pfrommer (2020) and normalising the cooling luminosity to quantities in our ICs (see section 3.1), we get

$$\begin{aligned} L_X &= \int_V \epsilon^{\text{ff}} dV = \Lambda_0 \sqrt{\frac{k_B T}{k_B T_0}} 4\pi \int_0^\infty n^2(r) r^2 dr \\ &\approx 4 \times 10^{44} \left( \frac{r_0}{80 \text{ kpc}} \right)^3 \left( \frac{n_0}{0.03 \text{ cm}^{-3}} \right)^2 \left( \frac{k_B T}{3.34 \text{ keV}} \right)^{1/2} \text{ erg s}^{-1}, \end{aligned} \quad (2.15)$$

where  $\Lambda_0$  is the cooling function with  $T_0$  at the very cluster center and  $n^2(r)$  is adopted by a  $\beta$ -profile (see equation 2.8). Hence, we are looking for a heating process with an average rate of  $\sim 10^{44}$  erg/s in order to balance the cooling losses in the ICM.

## 2.2. AGN feedback

As already described phenomenologically in section 2.1.5, hydrodynamic simulations modelling the gas dynamics of DM halos incorporating solely radiative cooling and gravitational heating cannot reproduce the central gas densities, temperatures and baryon fractions of the hot ICM (McNamara and Nulsen, 2012). Baryons respond to more complex processes like energetic feedback from supernova explosions and AGNs. Multiple studies of observational X-ray data by *XMM-Newton* and *Chandra* have shown that radio AGN are probably the principal driving mechanism heating the hot atmospheres of galaxy clusters and suppressing cooling rates (see Soker (2016) and references therein). Other heating mechanisms have been suggested over the years and are briefly discussed in section 2.2.5.

As the cluster atmosphere cools and condenses into molecular clouds and cold clumps, stars are able to form and the ambient gas is accreted by a super-massive black hole (SMBH) found in the central brightest cluster galaxy (BCG) of almost all CCs. From a simplified point of view, the accretion flow onto the black hole launches collimated outflows whenever the accreted gas has a large enough specific angular momentum (Soker, 2016). More specifically, these outflows are relativistic jets powered by the central AGN. The jets are composed of cosmic rays and toroidal magnetic fields, which causes non-thermal radio-synchrotron and  $\gamma$ -ray emission via particle acceleration. At some point the momentum of the relativistic outflow slows down due to the ram pressure of the ambient ICM. The cluster gas gets pushed away by the jet fluid, thereby inflating large radio-emitting lobes on either side of the nucleus. These lobes coincide with cavities observed in the X-ray band, as in e.g. Hydra A (McNamara et al., 2000), Perseus (Fabian et al., 2000) or Abell 2052 (Blanton et al., 2001). We will further on use the terms cavity and lobes, referring to bubble observations in the X-ray or the radio regime, respectively. The whole picture is shown in figure 2.2 for the Perseus cluster. As the jets terminate, the bubbles detach and are now injected at the bottom of the gravitational cluster potential. The bubbles are hotter ( $T_{\text{bub}} \approx 100 \times T_{\text{amb}}$  estimated observationally (Soker, 2016)) and underdense ( $\rho_{\text{bub}} \approx 0.01 \times \rho_{\text{amb}}$  used numerically (Dong and Stone, 2009)) compared to the ambient gas of the ICM. Hence, the bubbles are not static and start to rise buoyantly and subsonically up the cluster atmosphere (Pfrommer, 2020). Subsonically, because the bright rims surrounding many active cavities are observed to be cooler than the ambient ICM. This implies that they have been uplifted without being strongly shocked (Boettcher et al., 2012).

### 2.2.1. Jet-inflated bubble properties

In order to reproduce a proper evolution of bubbles, numerical simulations show that jet inflation can sufficiently stabilize the bubbles (Sternberg and Soker, 2008) in order to match their longevity with observations (see section 2.2.2). The morphology and geometry of the bubbles is strongly affected by the properties of the jets inflating them. The primary parameter thereby is jet power (Ehlert et al., 2018).

Cavity systems show a large spread in terms of their sizes. Typical observed radii have values of  $r_{\text{bub}} \sim 10\text{-}15 \text{ kpc}$  (Rafferty et al., 2006), but can go up to 200 kpc in diameter for the Hydra A cluster or MS0735.6+7421 (Nulsen et al., 2005; McNamara et al., 2005). The distribution of the ratio between the projected distance  $R$  between cavity center and the nucleus and the cavity radius  $r_{\text{bub}}$  shows a strong peak at  $R/r_{\text{bub}} \simeq 2$ . Meaning that jet-inflated bubbles travel their own diameters after they have detached from the jet and before they will dissipate into the atmosphere and will not be detectable any longer (McNamara and Nulsen, 2007).

Looking at the buoyancy time-scale, cavities have typical ages of  $t_{\text{buoy}} \sim 10^7 - 10^8 \text{ yr}$ . The time taken between single injections of bubbles is of the same order of magnitude, e.g. in Perseus

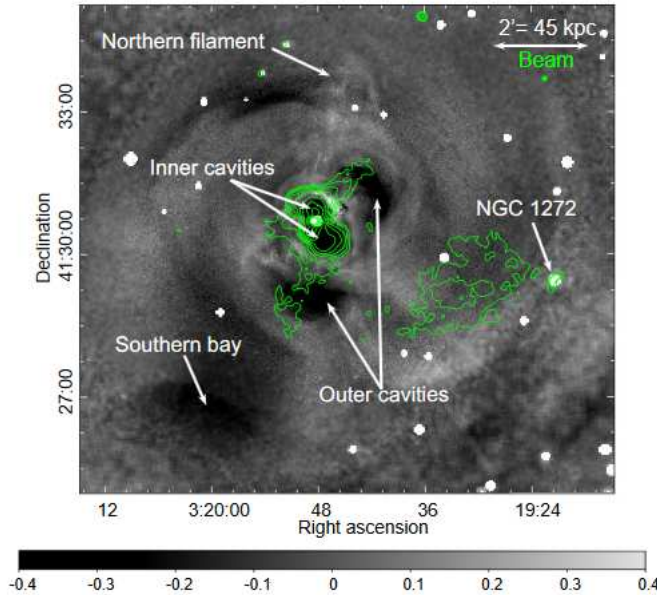


Figure 2.2.: Large-scale *Chandra* final composite residual surface brightness map of the Perseus cluster in the X-ray band taken from [Fabian et al. \(2011\)](#). Overlaid are low-frequency radio contours taken from data of the Very Large Array (VLA) ([Weeren et al., 2020](#)). The beam size is shown on the top-right corner. In the center lies the giant elliptical galaxy NGC 1275, whose SMBH powers bipolar jets into the ICM, which are inflating under-dense bubbles. Those are simultaneously visible as X-ray cavities and radio lobes (labeled inner cavities). As the bubbles rise buoyantly outwards the cluster atmosphere, they become disconnected from the feeding jets (labeled outer or ghost cavities).

([McNamara et al., 2000](#)). This implies that there are periods of time where no jets are launched, e.g. in Ophiuchus ([Werner et al., 2016](#)). The so-called cyclical jet feedback mechanism (JFM) ([Soker, 2016](#)) is based on the fact, that CCs with two or more bipolar pairs of bubbles are seen, like in Perseus ([Fabian et al., 2000](#)) or Hydra A ([Wise et al., 2007](#)). In addition, even clusters inhabiting very powerful AGNs like MS0735.6+7421 show large-scale symmetry in their cavities, which is visible at times after multiple outburst cycles have happened ([McNamara and Nulsen, 2012](#)). Simulations also show ([O'Neill and Jones, 2010; Mendygral et al., 2012](#)) that a cyclical JFM is able to make the lobes more spherical, as observed. Instead, a steady, continuous jet support produces highly elongated fronts ([Vernaleo and Reynolds, 2007](#)).

Nevertheless, some properties of bubbles cannot be determined yet from observations like the temperature or the general content of the filling gas, because of the very low densities inside the bubbles ([Soker, 2016](#)). Magnetic fields are assumed to be sub-dominant within the bubbles and small-scale vortices could dominate their energy content ([Hardcastle and Croston, 2005; Hardcastle and Krause, 2014](#)). The alignment of magnetic fields in radio lobes can be derived from the degree of polarization of synchrotron radiation. For FR-type I jets, which are considered throughout this thesis, the magnetic field lines are found to be typically perpendicular to the jet axis ([Hawley et al., 2015](#)).

### 2.2.2. Bubble stability

While theoretical studies suggest that bubbles should be rapidly disrupted in a CF environment, observations indicate that they live for a long time, meaning that the lobes sustain their morphology with a spherical front over  $\sim 100$  Myr, analysed observationally ([Rafferty et al., 2008](#)) and numerically ([Bourne et al., 2019](#)). However, some development of RTI are seen at the center-front of some bubbles, e.g. in Abell 2052 ([Blanton et al., 2001, 2003](#)) or in the northwest

bubble in Perseus (Fabian et al., 2002; Soker et al., 2002). Advances in numerical simulations have been showing that buoyantly rising bubbles are disrupted through KHI or RTI. Disruption can be delayed if the instability is suppressed by either turbulent diffusion (Scannapieco and Brüggen, 2008), magnetic draping (Ruszkowski et al., 2007; Dursi and Pfrommer, 2008; O’Neill et al., 2009), favorable dynamics (Pizzolato and Soker, 2006), or CRs (Ehlert et al., 2018). This thesis will focus on the suppression of instabilities by viscosity and investigate whether viscosity can preserve coherence of rising bubbles by damping the small-scale perturbations, which was especially studied by Reynolds et al. (2005) and Dong and Stone (2009). Thus, the model setup for the ICs, described in section 3.1, follows the ones used by those two papers.

As long as the lobes remain intact, they will maintain approximate pressure balance with their surroundings while rising buoyantly. As their pressure decreases with time, their enthalpy will also decrease, which releases energy into the ICM, mostly as kinetic energy in the flow around rising bubbles (McNamara and Nulsen, 2007).

### 2.2.3. Cavity power

Since almost every CC with  $t_{\text{cool}} \lesssim 1 \text{ Gyr}$  hosts an active radio source in their BCG (Mittal et al., 2009), sufficient amount of energy could have been also generated via synchrotron radiation. The synchrotron emission, which is visible in the radio, is due to CR-electrons gyrating around magnetic field lines. Comparing cavity power with bolometric radio power reveals that the mean mechanical power is 100-1000 times larger than the synchrotron power (Birzan et al., 2008; O’Sullivan et al., 2011), making the synchrotron radiation highly inefficient for heating the ICM. Hence, the AGN’s energy required depends on its mechanical power and not its radio luminosity. If we assume that the rising cavities are governed by buoyancy, their ages and mean jet power can be estimated (Churazov et al., 2002; Birzan et al., 2004). As the X-ray cavities are inflated, they do  $pV$  work (mechanical energy) against the ICM. At the same time, as the relativistic jets displace the ICM at the location of the cavities, they provide the pressure supporting the latter in form of internal energy  $E_{\text{th}}$ . Hence, the total energy required to create the cavity is equal to its enthalpy, (Gitti et al., 2012)

$$H = E_{\text{th}} + pV = \frac{\gamma}{\gamma - 1} pV = \begin{cases} 2.5 pV, & \text{for } \gamma = 5/3, \\ 4pV, & \text{for } \gamma = 4/3, \end{cases} \quad (2.16)$$

where  $\gamma$  is the ratio of specific heats of the cavity plasma, which depends on whether the pressure support is supplied by relativistic or non-relativistic plasma. Looking at the measured synchrotron emission, one has to assume equipartition between the energy of the particles and the energy of the magnetic field of the bubbles. From this, one can infer the pressure of the bubbles, which is only  $\sim 10\%$  of the pressure of the surrounding ICM (Worrall, 2000; Croston et al., 2008). In order to keep the bubbles stabilized, either a very hot thermal gas (which is not observed) or a non-thermal component has to be present (McNamara and Nulsen, 2012). If the radio emitting lobes were filled with a non-relativistic thermal plasma, the temperature would need to exceed  $\approx 20 \text{ keV}$  in order to be undetectable by its thermal X-ray emission (Blanton et al., 2003; Gitti et al., 2007). Therefore, it is more likely to assume that the bubbles are filled with relativistic plasma, giving  $\gamma = 4/3$  and  $H = 4pV$  per cavity. The cavities may be filled with more complex gas (with a non-thermal component to stabilize the bubble (McNamara and Nulsen, 2012)), but observations selected for large, fully-grown bubbles are roughly consistent with MHD simulations using  $4pV$  per cavity (Mendygral et al., 2011). However, in our simulations we assume that the bubble interior is non-relativistic and we will neglect the effects of CRs in the rest of the thesis.

In order to estimate the AGN heating rate based on the cavity power, we need to obtain the

ratio between work done by the two bubbles and the buoyancy time. The derivations covered hereafter are following the lecture notes from Pfrommer (2020). The cavity power is the product of the volume of the bubble and the surrounding pressure. Normalizing it to quantities in our ICs (see section 3.1) yields

$$pV = 2 \times n_{\text{amb}} k_B T \times \frac{4}{3} \pi r_{\text{bub}}^3 \approx 3 \times 10^{59} \text{ erg} \left( \frac{r_{\text{bub}}}{20 \text{ kpc}} \right) \left( \frac{n_{\text{amb}}}{0.03 \text{ cm}^{-3}} \right) \left( \frac{k_B T}{3.34 \text{ keV}} \right). \quad (2.17)$$

Subscripts amb and bub are abbreviations for the ambient and bubble component of that quantity, respectively. The expression is multiplied by two to account for both of the bipolar aligned bubbles. The buoyancy rise time can be computed by balancing the buoyancy force  $F_{\text{buoy}}$  acting upon the bubble with the drag force  $F_{\text{drag}}$  exerted by the ram pressure on the bubble, yielding the terminal velocity  $v_t$  (McNamara and Nulsen, 2007)

$$\begin{aligned} \|\mathbf{F}_{\text{buoy}}\| &= -g V_{\text{bub}} (\rho_{\text{amb}} - \rho_{\text{bub}}) = -\frac{C_d}{2} \sigma \rho_{\text{amb}} v^2 = \|\mathbf{F}_{\text{drag}}\| \\ v_t &= \sqrt{\frac{2gV_{\text{bub}}}{\sigma C_d} \frac{\rho_{\text{amb}} - \rho_{\text{bub}}}{\rho_{\text{amb}}}} \approx \sqrt{\frac{2gV_{\text{bub}}}{\sigma C_d}}, \end{aligned} \quad (2.18)$$

where  $\sigma$  is the cross-section of the bubble,  $g$  is the gravitational acceleration and  $C_d$  is the drag coefficient, which depends on the bubble geometry and the Reynolds number (see section 2.3.4). For a Mach number of  $\mathcal{M} \approx 0.7$  the drag coefficient is  $C_d \approx 0.6$  (Churazov et al., 2001). In the last step we assumed  $\rho_{\text{bub}} \ll \rho_{\text{amb}}$ . As a last step it is also useful to introduce an estimate for the sound-crossing time  $t_{\text{sc}}$  normalised to quantities in our ICs (over the gravitational radius  $R_G$ ), which is given by

$$t_{\text{sc}} \stackrel{(2.4)}{=} \frac{R_G}{c_s} \approx 3 \times 10^8 \text{ yr} \left( \frac{R_G}{240 \text{ kpc}} \right) \left( \frac{c_s}{800 \text{ km s}^{-1}} \right)^{-1}.$$

Together with the rise velocity from equation (2.18) we can now deduce the buoyancy time  $t_{\text{buoy}}$  for a bubble at distance  $R$  from the cavity center to the SMBH,

$$t_{\text{buoy}} = \frac{R}{v_t} \approx 0.6 \times t_{\text{sc}} \left( \frac{R}{2r_{\text{bub}}} \right)^{1/2} \approx 4 \times 10^{15} \text{ s} \approx 1.3 \times 10^8 \text{ yr}, \quad (2.19)$$

where the first approximation is derived in Birzan et al. (2004). Our estimate is in agreement with observations (see section 2.2.1). The buoyancy time gives a reasonable estimate for the later stage of a cavity system, long after it was injected by its AGN (McNamara and Nulsen, 2007). We can finally combine equations (2.19) and (2.17) to obtain the AGN heating rate,

$$L_{\text{AGN}} \approx \frac{2.5 pV}{t_{\text{buoy}}} \approx 7.5 \times \frac{10^{59} \text{ erg}}{4 \times 10^{15} \text{ s}} \approx 2 \times 10^{44} \text{ erg s}^{-1} \approx 0.5 \times L_X. \quad (2.20)$$

Hence, the AGN heating rate based on cavity power is comparable to the X-ray cooling luminosity, obtained from equation (2.15), which is supported by observational analysis of the cooling region in CCs (Rafferty et al., 2006; Gitti et al., 2012). This suggests that heating via AGN feedback is the primary mechanism providing roughly enough energy (in synergy with additional heating sources) to substantially prevent cooling flows in cool-core clusters (McNamara and Nulsen, 2012). How much energy is contributed by other proposed heating channels is an ongoing field of studies (see section 2.2.5).

### 2.2.4. Heating by AGN feedback

As described in section 2.2.3, the overall energetics between jet-induced power and cooling luminosity seem to be fitting. Neither cooling nor heating is dominating. Even the most powerful AGNs with the shortest cooling times in CCs (e.g., MS0735.6+7421 (McNamara et al., 2005)) show stable and long-lived CFs. Additionally, as pointed out in section 2.2.1, AGNs trigger outbursts on time-scales shorter than the cooling time-scales in their center. In fact,  $t_{\text{buoy}} \lesssim t_{\text{cool}}$ , meaning that generally cavities are younger than the time needed for the ambient gas to cool. This implies that jets are launched frequently enough to prevent runaway cooling (McNamara and Nulsen, 2012). Steep abundance gradients show that there is no large-scale mixing taking place (Fabian, 2012). This gentle, quasi-continuous (on time-scales  $\lesssim 10^8$  yr, (Rafferty et al., 2008)) heating process is shown as a flattening of the central entropy profiles (Voit and Donahue, 2005).

The general heating mechanism works as follows. As a buoyant cavity rises, it displaces gas, which must fall inward to fill the low-density wake. There, kinetic energy is generated from gravitational potential energy, which is then dissipated locally (McNamara and Nulsen, 2007). The energy created this way by the cavity is equal to the concomitant loss of enthalpy thermalized in its wake (Churazov et al., 2002). However, it is still under debate, how the thermal energy is supplied, distributed and dissipated on the right spatial scales to balance radiative cooling throughout the core of the cluster. The exact coupling mechanism has not been identified yet. (McNamara and Nulsen, 2012; Fabian, 2012; Soker, 2016) Different theories are briefly mentioned in section 2.2.5.

X-ray observations by *Hitomi* of the Perseus cluster core reveal low velocity dispersions (Hitomi Collaboration et al., 2018). Hillel and Soker (2017) conclude, that heating by small-scale mixing of hot bubble plasma with the ICM is very likely. The mixing is taking place in the wake where vortices have formed. These vortices also excite sound waves and turbulence, but they only make up  $\lesssim 20\%$  to the heating process. Shocks contribute even less Hillel and Soker (2017). The mixing is depositing CRs and magnetic energy as well.

Looking at the ICM as a whole, no single heating process seems to be dominant over all radii (McNamara and Nulsen, 2007). Many of them are probably relevant. At the innermost part, weak shocks are likely to be most significant. At radii where the lobes are formed, cavity heating takes over and on larger scales, sound damping may become dominant. At the outermost scales, thermal conduction is the most efficient. All in all, heating by AGN feedback seems to be dominating from the inside, while conductive heating is working from the outside of a CC (McNamara and Nulsen, 2007).

### 2.2.5. Other Heating Mechanisms

We described how the AGN-inflated cavities theoretically inhibit roughly enough energy to balance radiative cooling via bremsstrahlung while preventing the cooling catastrophe. As already mentioned, there is no consensus how this AGN energy is actually thermalized and which processes are key for transfer the energy from the jet-inflated bubbles to the ambient ICM. Many different heating mechanisms have been proposed over the years and discussing all of them will be far beyond the scope of this thesis. Therefore, we only list recent studies of the most common discussed heating models, which include AGN-initiated weak shocks (Li et al., 2016; Guo et al., 2017), dissipation of sound waves (Fabian et al., 2017; Bambic and Reynolds, 2019), dissipation of internal waves (Zhang et al., 2018), dissipation of turbulence (Zhuravleva et al., 2014), mixing of hot bubble gas with the ICM (Hillel and Soker, 2017), gas sloshing (Ueda et al., 2020), CRs (Jacob and Pfrommer, 2017b; Ehlert et al., 2018) and thermal conduction (Yang and Reynolds,

2016b).

In this work, we will focus on viscous heating in section 4.1.3.

## 2.3. Plasma Physics

### 2.3.1. Plasma Parameters

We have treated the ICM as a completely ionized, ideal gas in the previous sections, but it can also be well described as a plasma *fluid* if the particle mean free path,  $\lambda_{\text{mfp}}$ , is much shorter than the characteristic system size,  $L$  (Pfrommer, 2020). To check whether this can be taken for granted, we need to introduce some plasma parameters. Consider a non-relativistic hydrogenic plasma with equal ion and electron number densities,  $n = n_i = n_e$ , and temperatures,  $T = T_i = T_e$ . The mean mass per particle is then  $m_p/2$  and the (iso-)thermal speed of the ions is  $v_{\text{th}} = (p/\rho)^{1/2} = (2k_B T/m_p)^{1/2}$  (see equation (2.4)). Together with the ion-ion collision frequency,  $\nu_{ii} = 0.06 \times \ln \lambda \times n_i T^{-3/2} \text{ s}^{-1}$  (see equation (2.29)), the value of the mean free path in a cluster atmosphere can be estimated as (see ZuHone and Roediger (2016))

$$\lambda_{\text{mfp}} = \frac{v_{\text{th}}}{\nu_{ii}} \approx 0.5 \text{ kpc} \left( \frac{n}{0.03 \text{ cm}^{-3}} \right)^{-1} \left( \frac{k_B T}{3.34 \text{ keV}} \right)^2, \quad (2.21)$$

where  $\ln \lambda \sim 30$  is the Coulomb logarithm. The characteristic system size can be estimated via the thermal pressure scale height  $H$  (Kunz et al., 2012) by considering  $g = \rho^{-1} dp/dr$  as the gravitational acceleration (see equation (2.6)).

$$H = \frac{v_{\text{th}}^2}{g} \approx 130 \text{ kpc} \left( \frac{n}{0.03 \text{ cm}^{-3}} \right) \left( \frac{k_B T}{3.34 \text{ keV}} \right) \left( \frac{g}{10^{-8} \text{ cm s}^{-2}} \right)^{-1}. \quad (2.22)$$

Hence,  $\lambda_{\text{mfp}} \ll H$  and the fluid description of the ICM is applicable and the plasma is said to be weakly collisional. This can be expressed in terms of the Knudsen number,  $\text{Kn} = \lambda_{\text{mfp}}/H$ , which is a dimensionless measure for collisionality. Since  $\text{Kn} \sim 0.004$ , the intracluster plasma is not purely collisional, but rather weakly collisional. Plasmas with  $\text{Kn} \gtrsim 1$  would be effectively collisionless. The ion-ion collision frequency  $\nu_{ii}$  can also be related to the ion gyrofrequency  $\Omega_i = q_i B / m_p c$  of a particle gyrating around a magnetic field line of constant strength  $B$  due to the Lorenz force.  $\Omega_i$  is also called the Larmor frequency and the corresponding Larmor radius (or ion gyroradius)  $r_i$  is defined by

$$r_i = \frac{v_{\text{th}}}{\Omega_i} \approx 2 n p c \left( \frac{n}{0.03 \text{ cm}^{-3}} \right) \left( \frac{k_B T}{3.34 \text{ keV}} \right) \left( \frac{B}{1 \mu\text{G}} \right)^{-1}. \quad (2.23)$$

The ratio of the Larmor radius to the characteristic length scale of the system is called the plasma magnetization parameter  $\delta_i$  (Hazeltine and Waelbroeck, 2004). Thus as  $\delta_i = r_i/\lambda_{\text{mfp}} \approx 10^{-14} \ll 1$ , the ICM is magnetized, meaning that a particle gyrates around a magnetic field line so many times before it collides with another particle, that we can say it is tied to the field line. In other words, the collision frequency is much smaller than the gyrofrequency. Putting all relations together, we get that  $r_i \ll \lambda_{\text{mfp}} < H$ .

Furthermore, turbulence can excite three MHD waves, of which two are similar to sound waves (the fast and slow compressive modes) and one is solenoidal (the Alfvén mode). For the latter the Alfvén velocity for ions is given by

$$v_A = \frac{B}{\sqrt{4\pi\rho}} \approx 13 \frac{\text{km}}{\text{s}} \left( \frac{n}{0.03 \text{ cm}^{-3}} \right)^{-1/2} \left( \frac{B}{1 \mu\text{G}} \right). \quad (2.24)$$

Studies find that turbulent gas motions in CCs have velocity dispersions of several hundred km/s at the outer scale of several tens of kpc, which is shown both observationally with *Hitomi* in

Perseus (Hitomi Collaboration et al., 2018) and numerically with simulations of cluster formation (Miniati, 2014). This means that ICM turbulence is super-Alfvénic on the largest scales initially. Therefore, magnetic fields are probably not very important dynamically on such scales and the plasma is well shaped by fluid motions (Donnert et al., 2018). The ratio of thermal gas pressure  $p_{\text{th}} = nk_B T$  to magnetic pressure  $p_B = B^2/8\pi$  is described by the so-called plasma- $\beta$ , which is a dimensionless parameter for the effective strength of the magnetic field.

$$\beta = \frac{2k_B T}{m_p v_A} = \frac{8\pi n k_B T}{B^2} \approx 4000 \left( \frac{n}{0.03 \text{ cm}^{-3}} \right) \left( \frac{k_B T}{3.34 \text{ keV}} \right) \left( \frac{B}{1 \mu\text{G}} \right)^{-2}. \quad (2.25)$$

Since  $\beta$  is typically quite high (Carilli and Taylor, 2002) it is interesting to investigate whether weak magnetic fields are dynamically important at all in cluster atmospheres. One goal of this thesis is to study how such a weakly magnetized medium affects the evolution of buoyantly rising bubbles.

### 2.3.2. ICM as a weakly collisional plasma

Therefore, the ICM can be treated as a weak collisional plasma with a weak magnetic field with  $\|\mathbf{B}\| \sim 1 \mu\text{G}$ . In centers of CCs magnetic field strength of tens of microgauss have been inferred, which scale with thermal density, while considering that the plasma- $\beta$  is constant (isothermal) (Clarke et al., 2001; Bonafede et al., 2010). Both the Coma and the Perseus cluster host a turbulent magnetic field consistent with a Kolmogorov power spectrum (Schuecker et al., 2004; Subramanian et al., 2006). Evidence for magnetic fields comes from Faraday rotation measurements and synchrotron emission of radio sources in galaxy clusters (Ferrari et al., 2008; Govoni et al., 2010).

In addition, if the ICM would be governed by Coulomb collisions, transport properties would be isotropized. But since the plasma is only weakly collisional, the particles are coupled to the magnetic field lines, making transport of heat and momentum anisotropic. In turn, the magnetic field lines are frozen into the plasma fluid and advected with the bulk motions of the ambient medium (Kulsrud and Ostriker, 2006). In other words, motions of the intracluster gas causes changes in the magnetic field strength as the field is dragged along with the gas flow. This aspect is related to the magnetic Prandtl number  $\text{Pr}_m = \nu/\eta$ , which is the ratio of momentum to magnetic diffusivity. For galaxy clusters we get  $\text{Pr}_m \approx 10^{29} \gg 1$ , hence the viscous-scale motions dominate (Schekochihin and Cowley, 2007). Such conditions induce a small-scale dynamo, which amplifies the magnetic fluctuations by random stretching of the field lines on time-scales of  $10^8 \text{ yr}$  (Schekochihin et al., 2005).

All this together fundamentally changes the stability properties of the ICM, which differ from those expected from the Schwarzschild criterion. This criterion states that an atmosphere is stable to convection if the entropy,  $S$ , increases with height as  $dS/dr > 0$  (Carroll and Ostlie, 2014). As pointed out in section 2.1.5, a positive entropy gradient is indeed observed for CCs (Piffaretti et al., 2006). Although the ICM is stable against convection according to the Schwarzschild criterion, it is not applicable because the ICM is a weakly collisional and weakly magnetized plasma. So the aforementioned anisotropic transport needs to be considered, which means that e.g. the gas pressure perpendicular and parallel to the local magnetic field become unequal, resulting in anisotropic viscous stresses. Particle motions perpendicular to the magnetic field are suppressed and motions parallel to the field are either unconstrained or limited by  $\lambda_{\text{mfp}} \ll r_i$ . Collisions between ions do not occur frequently enough to counteract the pressure anisotropy. These effects make the ICM subject to fast growing instabilities on microscopic scales (between  $r_i$  and  $\lambda_{\text{mfp}}$ ) where their description by Braginskii-MHD becomes invalid (see section 2.3.6).

### 2.3.3. Turbulence

Turbulence according to Kolmogorov (Kolmogorov, 1941) describes how the energy of a nonlinear process is cascaded from large scales of vortical fluid motion to small scales of length  $l$  at a rate  $kv$ , where  $k = 2\pi/l$  is the wave vector,  $v$  is the velocity dispersion (the root-mean-square of the power spectrum at scale  $k$ ) and  $l$  is the eddy size. For subsonic turbulence ( $v < v_{\text{th}}$ ) the velocity fluctuations are adiabatic, which is implied by assuming an incompressible flow,  $\nabla \cdot \mathbf{v} = 0$ . At the macroscopic injection scale,  $L$ , energy is fed into the turbulent cascade by inducing fluid motions manifesting as eddies of size of the outer scale. This is also called the driving scale of the turbulent system, where in the case of galaxy clusters the driver might be a major merger or an AGN jet. The largest eddies break up into smaller ones due to the convective term,  $\mathbf{v} \cdot \nabla \mathbf{v}$ , in the fluid equations. Energy is being transferred at each smaller length scale until the local kinetic energy gets dissipated by viscosity at the microscopic inner scale,  $l_{\text{visc}}$ . Here, at scales of order of  $\lambda_{\text{mfp}}$ , viscous shear stresses dissipate the vortical motions into thermal energy and the Lorentz force dissipates the local kinetic energy into magnetic energy in case of a dynamo. Note that the dissipation scale is locally isotropic while the injection scale is highly anisotropic. The intermediate range of scales  $l$ , where  $L > l > l_{\text{visc}}$ , is called the inertial range. At each scale, the cascading time-scale is the eddy turnover time,  $t_l = l/v_l$ , where  $v_l$  is the typical rotational velocity across the eddy. The cascading itself is not depending on the driving scale (Schekochihin and Cowley, 2007). In the inertial range, energy cascading scales as  $\epsilon_{\text{kin}} \propto v_l^2/t_l \propto v_L(l/L)^{2/3}$  and the turbulent velocity scales as  $v_l \propto l^{1/3}$ . This implies that the largest eddies have the highest velocities and kinetic energies, while the smallest eddies have the highest vorticity. In other words, the turbulent system is driven by energy at the outer scale, but dominated by viscous forces at the dissipative inner scale. The hierarchy of eddies can be described by the energy power spectrum  $E(k)$  (Schekochihin and Cowley, 2007),

$$v_l^2 \sim \int_k^\infty E(k') dk' \sim \epsilon^{2/3} k^{-2/3} \Rightarrow E(k) \sim \epsilon^{2/3} k^{-5/3}. \quad (2.26)$$

The characteristic time-scale for turbulence of a typical galaxy cluster to be established during a major merger is  $t_L = L/v_L \sim 300 \text{ kpc}/(1000 \text{ km s}^{-1}) \approx 300 \text{ Myr}$  (Brunetti and Lazarian, 2007), where  $v_L$  is the velocity dispersion of the largest eddy at the outer scale  $L$ . In case that AGN-inflated bubbles are driving turbulence in a relaxed ICM, the characteristic time-scale can be estimated as  $t_L \sim 20 \text{ kpc}/(400 \text{ km s}^{-1}) \approx 50 \text{ Myr}$  (see section 3.1). Observationally, these scales are in agreement with turbulence measures using pressure maps, i.e. in the Coma cluster (Schuecker et al., 2004). Additionally, the viscous scale of an AGN-driven cluster can be approximated as  $l_{\text{visc}} \sim L \text{Re}^{-3/4} \sim 1 \text{ kpc}$  (Schekochihin et al., 2005), where  $\text{Re} = 50$  is the Reynolds number based on typical values of the ICM (see section 2.3.4). Comparing  $l_{\text{visc}}$  with  $\lambda_{\text{mfp}}$  from equation (2.21) shows that both act on length scales of roughly the same order of magnitude.

Turbulent fluid motions in a cluster atmosphere can be induced by stresses of tangled magnetic field lines permeating the cluster. Concomitantly, the magnetic field power spectrum is also consistent with a Kolmogorov power spectrum as observations (Schuecker et al., 2004) and simulations (Gaspari and Churazov, 2013; ZuHone et al., 2016) find for the Coma cluster. Also the Perseus CC (Subramanian et al., 2006) and Hydra A (Kuchar and Enßlin, 2011) seem to host a turbulent magnetic field. Bonafede et al. (2010) and Kuchar and Enßlin (2011) fit their models to Faraday rotation measurements to constrain the magnetic field strength and to find the magnetic power spectrum. They find a magnetic field dependence on the electron number

density as

$$\langle B^2(r) \rangle \propto n_e^{2\alpha}(r) \quad (2.27)$$

with  $\alpha = 0.4 - 0.7$  (Bonafede et al., 2010). These findings are consistent with a constant plasma beta throughout the cluster gas, since  $\beta = 8\pi nkT/B^2$ .

### 2.3.4. Reynolds Number

As introduced in the previous section, a turbulent fluid cascades large scale motions to progressively smaller scales until viscous forces become important to dissipate the kinetic energy. At larger scales the fluid motion is undamped. To indicate at what scale the viscous dissipation takes over, the Reynolds number,  $\text{Re}$ , is introduced. The Reynolds number is a dimensionless quantity to show whether a fluid is governed by laminar flow or turbulence. It is defined as the ratio between inertial and viscous forces in a fluid. Hence, for  $\text{Re} \gg 1$ , viscous forces are not important at all at the inertial scales and vortical motions will be produced. Considering the kinematic viscosity  $\nu = \mu/\rho = \lambda_{\text{mfp}}v_{\text{th}}$ , which has units of  $\text{cm}^2 \text{s}^{-1}$ , we can also define the Reynolds number as the ratio of dissipative to advective time-scales (see Pfrommer (2020)),

$$\text{Re} = \frac{t_{\text{diss}}}{t_{\text{adv}}} = \frac{Lv_L}{\nu} = \frac{L}{\lambda_{\text{mfp}}} \frac{v_L}{v_{\text{th}}}, \quad (2.28)$$

where  $t_{\text{diss}} = L^2/\nu$  and  $t_{\text{adv}} = L/v_L$ . Here,  $L$  and  $v_L$  are characteristic length and velocity scales of system size. Therefore,  $\text{Re}$  can be expressed as the product of the ratios of macroscopic to microscopic length and velocity scales. Again, for  $\text{Re} \gg 1$ , advection is dominating and dissipation cannot stabilize the growth of the turbulent modes.

As pointed out in section 2.3.2, due to the pressure anisotropy in the ICM, heat and momentum are transported along the magnetic field lines with unit vector  $\mathbf{b} = \mathbf{B}/\|\mathbf{B}\|$ . So, the kinematic viscosity (also called momentum diffusivity) parallel to  $\mathbf{b}$  is  $\nu_{\parallel} = \mu/\rho = \mu/n_i m_p$ , where  $\mu$  is the dynamic viscosity,  $\rho$  is the density of the fluid,  $n_i$  is the number density of the ions and  $m_p$  is the mass of one particle. An upper limit for the kinematic viscosity has been found from X-ray observations for the Coma cluster of  $\nu_{\parallel} \lesssim 3 \times 10^{29} \text{ cm}^2 \text{s}^{-1}$  on scales of 90 kpc (Schuecker et al., 2004). In numerical simulations, a ceiling has been applied, i.e. by modelling the Perseus cluster with  $\nu_{\parallel} \lesssim 10^{30} \text{ cm}^2 \text{s}^{-1}$  (Kingsland et al., 2019).

Further,  $\mu = 0.96 \times p_i/\nu_{ii} = 0.96 \times n_i k_B T / \nu_{ii}$  (Kunz et al., 2012), where  $p_i$  is the ion thermal pressure,  $\nu_{ii}$  is the ion-ion collision frequency,  $k_B$  is the Boltzmann constant and  $T$  is the temperature of the fluid. Considering the value of  $\nu_{ii}$  for fully ionized plasmas (Richardson, 2019),

$$\nu_{ii} = \frac{4\sqrt{\pi}e^4 n_i \ln \Lambda}{3\sqrt{m_p} k_B^{\frac{3}{2}} T^{\frac{3}{2}}} = 6.0 \times 10^{-2} \frac{n_i \ln \Lambda}{T^{\frac{3}{2}}} \text{ s}^{-1}, \quad (2.29)$$

to be Spitzer if  $k_B = 1.381 \times 10^{-16} \text{ erg/K}$  (Spitzer, 1962). This yields for the dynamic viscosity,

$$\mu_{\text{sp}} = 2.2 \times 10^{-15} \frac{T^{\frac{5}{2}}}{\ln \Lambda} \text{ g cm}^{-1} \text{ s}^{-1}, \quad (2.30)$$

where  $T$  is measured in Kelvin. We can now write for the Reynolds number

$$\text{Re} = \frac{Lv_L}{\nu_{\parallel}} = \frac{Lv_L n_i m_p}{\mu_{\text{sp}}} = 2.3 \times 10^{-8} \times \left( \frac{v_L}{v_{L,0}} \right) \left( \frac{L}{L_0} \right) \left( \frac{n}{n_0} \right) \left( \frac{T}{T_0} \right)^{-\frac{5}{2}} \times v_{L,0} L_0 n_0 T_0^{-\frac{5}{2}}, \quad (2.31)$$

where we used  $\ln \lambda = 30$  in the prefactor (see e.g. Dong and Stone (2009) or Kingsland et al.

(2019)). We can use this notation to compute the Reynolds number from the ratios of four easily accessible variables. Typical values for the ICM in CCs yield Reynolds numbers of order  $\lesssim 10^2$  (Schekochihin and Cowley, 2007; Brunetti and Lazarian, 2007) if we assume Spitzer viscosity.

The Reynolds number can be estimated for the ICM of the Perseus cluster core region if  $v_L$  and  $L$  are inferred from Hitomi Collaboration et al. (2016) and  $n$  and  $T$  are inferred from Fabian et al. (2017):

$$\text{Re} \approx 50 \left( \frac{v_L}{164 \text{ km/s}} \right) \left( \frac{L}{10 \text{ kpc}} \right) \left( \frac{n}{0.04 \text{ cm}^{-3}} \right) \left( \frac{T}{3.87 \times 10^7 \text{ K}} \right)^{-5/2} \quad (2.32)$$

### 2.3.5. Braginskii-MHD

Ideal magnetohydrodynamics (MHD) is a continuum theory that combines the equations of fluid dynamics with Maxwell's equations to describe the behavior of a magnetized conducting medium. It is only applicable as a fluid approximation and does not describe the individual motions of particles directly, which would be subject to kinetic theory. Instead, the distribution functions,  $f(\vec{x}, \vec{v}, t)$ , are replaced with plasma moments such as density, mean velocity and mean energy. These moments are taken from the Vlasov equation extended by a collisional term. We refer to Baumjohann and Treumann (1997) for a full derivation.

As pointed out in section 2.3.2, the ICM is highly conductive ( $\text{Pm} \gg 1$ ), so that its resistivity is negligibly small. Thus according to the induction equation, the magnetic field lines are frozen into the plasma fluid, known as Alfvén's theorem (Alfvén, 1942). In addition, as described in section 2.3.1, the ICM must be modelled as a weakly collisional, magnetized plasma, where  $\lambda_{\text{mfp}} \gg r_i$ . Therefore, on macroscopic scales (greater than  $\lambda_{\text{mfp}}$ ), the transport of momentum and heat becomes highly anisotropic along the direction of the local magnetic field lines, making the ideal MHD approximation inadequate. Accounting for anisotropic viscosity and heat conduction in form of diffusion terms leads to an extended MHD model, the so-called Braginskii-MHD (Braginskii, 1965). At frequencies below the Larmor frequency  $\Omega_i$  and at scales above the ion gyroradius  $r_i$ , the fundamental equations of motion (mass continuity, momentum, induction, energy) can be given in conservative form and in Gaussian units as (see e.g. Kunz et al. (2012); ZuHone and Roediger (2016))

$$\frac{\partial \rho}{\partial t} + \nabla \cdot (\rho \mathbf{v}) = 0, \quad (2.33)$$

$$\frac{\partial(\rho \mathbf{v})}{\partial t} + \nabla \cdot (\rho \mathbf{v} \mathbf{v} + \mathcal{P}) = \rho \mathbf{g}, \quad (2.34)$$

$$\frac{\partial \mathbf{B}}{\partial t} = \nabla \times (\mathbf{v} \times \mathbf{B}) = -\nabla \cdot (v \mathbf{B} - \mathbf{B} v), \quad (2.35)$$

$$\frac{\partial(\rho \epsilon)}{\partial t} + \nabla \cdot [(\rho \epsilon \mathbf{I} + \mathcal{P}) \cdot \mathbf{v} + \mathbf{Q}] = \rho \mathbf{g} \cdot \mathbf{v}, \quad (2.36)$$

where  $\epsilon$  is the energy per unit mass, so that  $\rho \epsilon$  is the energy per unit volume with  $\gamma = 5/3$  and  $\rho \epsilon \mathbf{v}$  is the internal energy flux. The total energy density (kinetic, internal, magnetic) is given by

$$\rho \epsilon = \frac{1}{2} \rho v^2 + \frac{p}{\gamma - 1} + \frac{B^2}{8\pi}. \quad (2.37)$$

The pressure tensor is given by

$$\begin{aligned}\mathcal{P} &= \left( p_{\perp} + \frac{B^2}{8\pi} \right) \mathbf{I} - \left( p_{\perp} - p_{\parallel} + \frac{B^2}{4\pi} \right) \mathbf{b}\mathbf{b} \\ &= p\mathbf{I} + \mathbf{\Pi} + \frac{B^2}{8\pi}\mathbf{I} - \frac{\mathbf{B}\mathbf{B}}{4\pi},\end{aligned}\quad (2.38)$$

with total thermal pressure:

$$p = \frac{2}{3}p_{\perp} + \frac{1}{3}p_{\parallel}, \quad (2.39)$$

where  $p_{\perp}$  ( $p_{\parallel}$ ) is the pressure term perpendicular (parallel) to the local magnetic field with  $\mathbf{b} = \mathbf{B}/B$  as the unit vector and  $\mathbf{b}\mathbf{b}$  as a dyadic product. The terms  $B^2\mathbf{I}/8\pi$  and  $\mathbf{B}\mathbf{B}/4\pi$  can be recognized as magnetic pressure and magnetic tension, respectively. The additional terms in equations (2.34) and (2.36) extending ideal MHD are the anisotropic heat flux  $\mathbf{Q}$  (which we neglect) and the anisotropic viscosity tensor

$$\mathbf{\Pi} = -\Delta p \left( \mathbf{b}\mathbf{b} - \frac{1}{3}\mathbf{I} \right), \quad (2.40)$$

where the pressure anisotropy is defined as  $\Delta p = p_{\perp} - p_{\parallel}$ . It arises from the conservation of the first and second adiabatic invariants for each particle (Chew et al., 1956). Viscosity and heat break these conservation laws. The so-called Chew, Goldberger & Law (CGL) equations can be derived from the Vlasov-Landau equation by taking the moments  $mv_{\perp}^2/2$  and  $mv_{\parallel}^2$  (see Schekochihin et al. (2010) and references therein). If viscosity and heat are neglected, then the CGL equations reduce to

$$p_{\perp} \frac{d}{dt} \left( \ln \frac{p_{\perp}}{\rho B} \right) = 0, \quad p_{\parallel} \frac{d}{dt} \left( \ln \frac{p_{\parallel} B^2}{\rho^3} \right) = 0, \quad (2.41)$$

where  $d/dt = \partial/\partial t + \mathbf{v} \cdot \nabla$  is the Lagrangian time derivative. We refer to Berlok (2014) for a full derivation. The first (second) adiabatic invariant in equation (2.41) arises from the conservation of angular (longitudinal) momentum. The non-reduced CGL equations together with collisionality, including viscosity and heat conduction, can be combined to get an expression for the evolution of the Braginskii pressure anisotropy:

$$\Delta p = p_{\perp} - p_{\parallel} = 0.96 \frac{p}{\nu_{ii}} \frac{d}{dt} \ln \frac{B^3}{\rho^2} \quad (2.42)$$

Hence, in a weakly collisional plasma like the ICM the production of pressure anisotropy is being relaxed by collisions, whereas would be quickly isotropized in a collisional plasma (having a Maxwellian distribution) (Schekochihin et al., 2005). As the first adiabatic invariant  $\mu = mv_{\perp}^2/2B$  is only weakly broken by collisions (since  $\lambda_{\text{mfp}} \gg r_i$ ), any change in  $B$  leads to a proportional change in  $p_{\perp}$  such that  $p_{\perp}/B = \text{const}$  (Schekochihin and Cowley, 2007). We can rewrite expression (2.42) by using the continuity equation (2.33) and the induction equation (2.35) to replace the time derivatives of  $\rho$  and  $B$  with velocity gradients. We may also use the identity relating the evolution of magnetic field strength with the rate of strain, assuming that motions in the inertial range are subsonic (see section 2.3.3),

$$\frac{1}{B} \frac{dB}{dt} = \mathbf{b}\mathbf{b} : \nabla \mathbf{v}, \quad (2.43)$$

where  $:$  is defined as the trace of a matrix product, such that  $\mathbf{b}\mathbf{b} : \nabla \mathbf{v} = \Sigma_i \Sigma_j b_i b_j \partial_i v_j$ . The

anisotropic pressure from equation (2.42) now reads

$$\Delta p = \frac{p}{\nu_{ii}} (3\mathbf{bb} - \mathbf{I}) : \nabla \mathbf{v} = \rho \nu_{\parallel} (3\mathbf{bb} : \nabla \mathbf{v} - \nabla \cdot \mathbf{v}), \quad (2.44)$$

where  $\nu_{ii}$  is the ion-ion Coulomb collision frequency. The prefactor  $\mu_{sp} = p/\nu_{ii} = \rho \nu_{\parallel}$  is the dynamic viscosity coefficient, or simply called Spitzer viscosity in terms of ions (see section 2.3.4).  $\nu_{\parallel}$  is the kinematic viscosity parallel to the local magnetic field line. This shows that the pressure anisotropy is effectively working out as an anisotropic viscous flux and the viscosity tensor from equation (2.40) becomes (Braginskii, 1965)

$$\boldsymbol{\Pi} = -3\mu_{sp} \left( \mathbf{bb} - \frac{1}{3}\mathbf{I} \right) \left( \mathbf{bb} - \frac{1}{3}\mathbf{I} \right), \quad (2.45)$$

which is implemented in *AREPO* by Berlok et al. (2019) (see section 2.4.1). While modelling a weakly collisional, magnetized plasma like the ICM, it is inevitable using the Braginskii extension of ideal MHD, if one is interested in studying the effects of thermal conduction and/or viscosity. However, e.g. the viscous stress tensor does not necessarily have to take an anisotropic form as in equation (2.45). In the presented thesis, we are also interested in how Braginskii viscosity affects the transport processes of the plasma and thus the morphology of the rising bubbles if the viscosity tensor is in fact isotropic and not depending on an pressure anisotropy. In this case the isotropic viscous stress tensor is simply given by (Kingsland et al., 2019) as

$$\boldsymbol{\Pi}_{iso} = -f_{\nu} \mu_{sp} \nabla \mathbf{v}. \quad (2.46)$$

This form is justified if the weak magnetic field is turbulent throughout the volume of a simulated cluster and isotropically tangled (ZuHone and Roediger, 2016). Then  $f_{\nu}$  becomes a suppression factor accounting for reduced viscosity (below the Spitzer value) due to averaging over the random direction of the magnetic field. Not all of our simulations have an initially turbulent magnetic field setup, especially not our fiducial run (see section 3.1). Therefore, we use a more elaborated version where the isotropic viscosity tensor is derived from the Navier-Stokes equations for a viscous flow (Muñoz et al., 2013),

$$\boldsymbol{\Pi}_{iso} = -\eta \left( \nabla \mathbf{v} + (\nabla \mathbf{v})^T - \frac{2}{3}\mathbf{I}(\nabla \cdot \mathbf{v}) \right) - \zeta \mathbf{I}(\nabla \cdot \mathbf{v}), \quad (2.47)$$

where  $\eta = \rho \nu_0 = \mu_{sp}$  is the shear viscosity and  $\zeta$  is the bulk viscosity. The former is referring to constant-volume shear deformations and the latter is corresponding to isotropic expansions/contractions. Note, that the bulk viscosity vanishes for an incompressible fluid flow ( $\nabla \cdot \mathbf{v} = 0$ ) or for an ideal monoatomic gas, which has no internal degrees of freedom if interpreted as hard spheres interacting only through elastic collisions. Hence, the isotropic Navier-Stokes viscosity implemented in *AREPO* by equation (2.47) assumes that  $\zeta = 0$ .

### 2.3.6. Micro-scale Instabilities

We can infer from equation (2.42) that an increasing magnetic field strength will yield a positive pressure anisotropy and regions with a decreasing field strength will have a negative anisotropic pressure, if the density is constant. Additionally, equation (2.44) shows that the pressure anisotropy controls the rate of viscous dissipation down to the dissipation scale (order of  $\lambda_{mfp}$ ) and thus affects the fluid dynamics at larger scales. Therefore, the Braginskii viscosity only dissipates such velocity gradients that change the strength of the magnetic field. (Schekochihin

and Cowley, 2007) The remaining motions not affecting  $B$  can in principle exist below the dissipation scale with their fastest growing modes down to the Larmor scale ( $r_i \ll \lambda_{\text{mfp}}$ ), where they act as micro-scale instabilities in a weakly magnetized, high- $\beta$  plasma. These rapidly growing instabilities are not yet resolved in simulations modelling galaxy clusters since it would require numerical resolutions ranging from several nano- to kilo-parsec scales and resolving  $\sim 10^{12}$  orders of magnitude is numerically not achievable. Nevertheless, theoretical studies (Schekochihin et al., 2008; Rosin et al., 2011) and particle-in-cell simulations (Kunz et al., 2014; St-Onge et al., 2020) show that the micro-scale instabilities, namely the firehose and the mirror instability, act such that they regulate the pressure anisotropy back to values within its stability boundaries. This is also supported by direct solar wind observations (Chen et al., 2016). So, whenever  $\Delta p$  exceeds certain thresholds (see e.g. Kunz et al. (2012)),

$$-\frac{B^2}{4\pi} \lesssim p_{\perp} - p_{\parallel} \lesssim \frac{B^2}{8\pi}, \quad (2.48)$$

the micro-scale firehose (left-hand side) and mirror (right-hand side) instability are triggered and drive  $\Delta p$  to marginal stability, where they saturate. In other words, the pressure anisotropy (and thus parallel viscosity) becomes unphysically large in weakly collisional, magnetized plasma fluid simulations, if no micro-physical limits are implemented, which would account for isotropizing the plasma to marginally stable levels. We describe both micro-instabilities schematically in figure 2.3. It shows that if the magnetic field strength gets enhanced via stretched or compressed field lines, the perpendicular pressure component becomes dominant, which excites the mirror instability. On the other hand, if  $B$  decreases locally due to turbulent velocities, the parallel pressure dominates and can trigger the firehose instability. We can rearrange the inequality (2.48) in a way, that we get an expression, where the pressure anisotropy is pinned at marginal stability (Kunz et al., 2011). Dividing by the total thermal pressure while considering the plasma beta  $\beta = 8\pi p/B^2$  yields

$$-\frac{2}{\beta} \lesssim \frac{\Delta p}{p} \lesssim \frac{1}{\beta} \Rightarrow \left( \frac{\Delta p_{\text{lim}}}{p} \right) = \left( \frac{\xi}{\beta} \right), \quad (2.49)$$

where  $\xi = -2$  for the firehose instability or  $\xi = 1$  for the mirror instability.

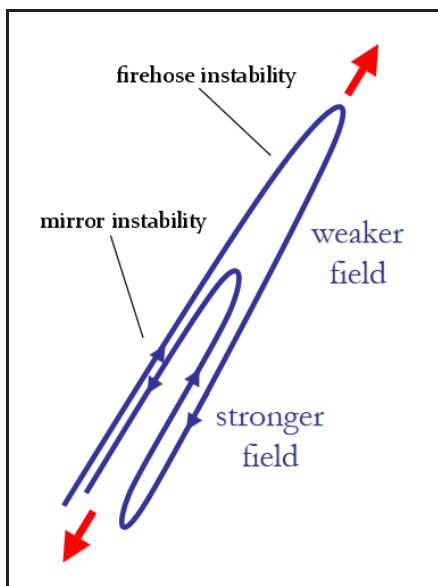


Figure 2.3.: Sketch how firehose and mirror instabilities emerge by bending the magnetic field lines. (adopted from Schekochihin and Cowley (2007)).

The limits from inequality (2.48) are also necessary to avoid unphysical results since the fluid description of the ICM by Braginskii-MHD becomes invalid at scales  $< \lambda_{\text{mfp}}$  ([Schekochihin et al., 2005](#)). [Kunz et al. \(2012\)](#) show that indeed the firehose fluctuations (which are resolved in their simulations to some extent) grow fast enough to compensate the negative excess in pressure anisotropy to retain marginal stability and self-consistently provide a lower bound to  $\Delta p$ . But the mirror instability excited by Braginskii-MHD grows substantially slower than the kinetic mirror fluctuations, meaning that positive pressure anisotropies are not efficiently regulated. Either way, [Kunz et al. \(2012\)](#) find that in general both micro-scale instabilities do not grow as fast using Braginskii-MHD as they would otherwise grow using kinetic theory since the fastest modes can not be resolved. For example, in Braginskii-MHD the firehose instability has a maximum growth rate occurring at  $k_{\parallel}H$ , whereas in kinetic theory the firehose instability actually has a maximum growth rate occurring at  $k_{\parallel}r_i$ , where  $H$  is the thermal pressure scale height and  $r_i$  is the Larmor radius (see section 2.3.1). Therefore, the effects of Braginskii conductivity and viscosity are probably overestimated by a factor  $H/r_i \sim 10^{10}\text{-}10^{11}$  ([Schekochihin et al., 2008](#)) in a weakly collisional, magnetized plasma.

## 2.4. AREPO

The cosmological MHD code *AREPO* (Springel, 2010) has been designed in order to combine the advantages of both Lagrangian smoothed-particle hydrodynamics (SPH) methods and finite volume Eulerian fixed Cartesian mesh codes. *AREPO* is based on a moving unstructured Voronoi mesh, which allows for a quasi-Lagrangian description while retaining better numerical convergence of Eulerian codes (Pakmor et al., 2016). In fact, *AREPO* uses a second-order accurate Runge-Kutta method to estimate the fluxes at each time step. The Voronoi mesh is generated from a set of points such that for each generator point there is a corresponding cell of volume containing cell points which are closest to that generator point. This spatial discretization is called Voronoi tessellation and uniquely constructs a mesh, which moves with the fluid flow and is updated over time accordingly. *AREPO* solves the hyperbolic conservation laws on the moving Voronoi mesh using a finite volume approach. In case of ideal MHD, the set of Euler equations can be written in compact form by introducing a state vector of conserved quantities  $\mathbf{U}$  and the flux function  $\mathbf{F}(\mathbf{U})$  for the fluid as (Pakmor et al., 2011)

$$\frac{\partial \mathbf{U}}{\partial t} + \nabla \cdot \mathbf{F} = 0, \quad (2.50)$$

where  $\mathbf{U}$  and  $\mathbf{F}(\mathbf{U})$  are given by

$$\mathbf{U} = \begin{pmatrix} \rho \\ \rho\mathbf{v} \\ \rho\epsilon \\ \mathbf{B} \end{pmatrix}, \quad \mathbf{F}(\mathbf{U}) = \begin{pmatrix} \rho\mathbf{v} \\ \rho\mathbf{v}\mathbf{v} + \mathcal{P} - \mathbf{B}\mathbf{B}/4\pi \\ \mathbf{B}\mathbf{v} - \mathbf{v}\mathbf{B} \\ \rho\epsilon\mathbf{v} + \mathcal{P}\mathbf{v} - \mathbf{B}(\mathbf{v} \cdot \mathbf{B})/4\pi \end{pmatrix}, \quad (2.51)$$

where  $\mathcal{P} = p\mathbf{I} + B^2\mathbf{I}/8\pi$  is the pressure tensor,  $p$  is the total thermal pressure and  $\rho\epsilon = \frac{1}{2}\rho v^2 + p/(\gamma-1) + B^2/8\pi$  is the total energy density in Gaussian units. Note the notation and correlation with continuity, momentum, induction and energy equations (2.33)-(2.36) of extended Braginskii-MHD. The fluid state is computed by taking the cell averages of the conserved quantities  $\mathbf{U}$  for each cell by integrating the fluid over the finite volume  $V_i$  of a cell  $i$ ,

$$\mathbf{Q}_i = \int_{V_i} \mathbf{U} dV. \quad (2.52)$$

yielding the total mass, momentum, energy and magnetic field strength contained in each cell. The introduced fluxes  $\mathbf{F}$  are only valid for a static grid, but since *AREPO* uses a moving mesh, the flux over a static interface has been added by an additional advection term  $\mathbf{U}\mathbf{w}^T$  owing for the movement of the interface with velocity  $\mathbf{w}$  (Pakmor et al., 2011). The geometry is illustrated in figure 2.4. By using Gauss' theorem we can get the rate of change in time of  $\mathbf{Q}_i$  as

$$\frac{d\mathbf{Q}_i}{dt} = - \int_{\partial V_i} [\mathbf{F}(\mathbf{U}) - \mathbf{U}\mathbf{w}^T] d\mathbf{e}_n = - \sum_j A_{ij} \mathbf{F}_{ij}, \quad (2.53)$$

where  $\mathbf{e}_n$  is a normal vector of an interface between two Voronoi cells and  $\mathbf{w}$  is the normal velocity of this interface.  $\mathbf{e}_n$  and  $\mathbf{w}$  describe the motion of the face, which is fully specified by the velocities of the mesh-generating points of the two cells next to the interface (Springel, 2010). Note, that in Eulerian codes  $\mathbf{w} = 0$  where the mesh becomes static. All the fluxes over an interface are computed in the rest frame of the moving interface, which means that the interface velocity is subtracted from the equations of motion. Only the relative velocity between the two Voronoi cells enters the flux estimation and not the dynamical flow of the moving mesh. This has the advantage that the flux solutions become Galilean-invariant, whereas in Eulerian methods using

fixed Cartesian meshes the numerical truncation error grows with the fluid velocity (Springel, 2010). The Riemann problem is solved by using the approximative *HLLD* solver in case of ideal MHD (Pakmor et al., 2011).

The right-hand side of equation (2.53) resembles the Euler equations in finite-volume form and is derived by calculating the averaged flux across the interface between cells  $i$  and  $j$  as

$$\mathbf{F}_{ij} = \frac{1}{A_{ij}} \int_{A_{ij}} [\mathbf{F}(\mathbf{U}) - \mathbf{U}\mathbf{w}^T] d\mathbf{A}_{ij}, \quad (2.54)$$

where  $\mathbf{A}_{ij}$  is the oriented area of the face between cells  $i$  and  $j$ . The fluid state is then evolved in time by discretization of equation (2.53) in time to finally yield (Springel, 2010)

$$\mathbf{Q}_i^{(n+1)} = \mathbf{Q}_i^{(n)} - \Delta t \sum_j A_{ij} \hat{\mathbf{F}}_{ij}^{(n+1/2)}, \quad (2.55)$$

where  $\hat{\mathbf{F}}_{ij}$  is a time-averaged approximation of the true flux  $\mathbf{F}_{ij}$ . The superscript  $(n)$  is denoting the state of the system at time step  $n$ .

Furthermore, the evolving magnetic field has to fulfill the constraint  $\nabla \cdot \mathbf{B} = 0$  to stay divergence-free. However, as the moving mesh is spatially discretized, numerical errors can significantly amplify the magnetic field and lead to unphysical results (Pakmor and Springel, 2013). Hence, *AREPO* adopts the divergence-cleaning method by Powell (Powell et al., 1999), where a passive advection term of the flow of the magnetic field is added to the Euler equations. This method has been implemented into the code by Pakmor and Springel (2013), where the divergence of the magnetic field in a cell  $i$  is then calculated as

$$\nabla \cdot \mathbf{B}_i = \frac{1}{V_i} \sum_{\text{faces}} \mathbf{B}_{\text{face}} \cdot \mathbf{e}_n A_{\text{face}}, \quad (2.56)$$

where  $\mathbf{B}_{\text{face}}$  is the magnetic field strength on the interface and  $V_i$  is the volume of the cell.

There are numerous other features implemented into *AREPO* to account for the novelty of having a moving mesh and we refer to Springel (2010) and Weinberger et al. (2020) for further details. In thesis we describe only those special treatments that we actually have included in our simulations in section 3.1, including i.e. the mesh regularization, de-/refinement criteria and boundary conditions.

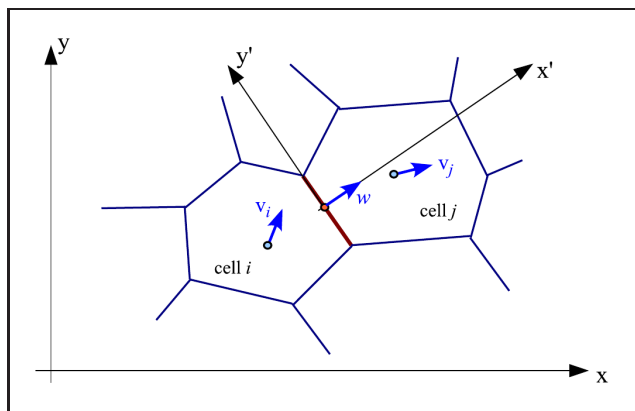


Figure 2.4.: Sketch showing the geometry of the flux calculation. An unsplit scheme is used where the flux across each face is estimated based on a one-dimensional Riemann problem. The fluid state is expressed in a frame which moves with the normal velocity  $w$  of the face, and is aligned with it. Taken from (Springel, 2010).

### 2.4.1. Braginskii Module

Braginskii viscosity is numerically implemented into the moving-mesh code *AREPO* by [Berlok et al. \(2019\)](#) as a subsequent module to already existing extensions to non-ideal MHD physics like isotropic viscosity ([Muñoz et al., 2013](#)) and anisotropic heat conduction ([Kannan et al., 2016](#)). Operator splitting is used to solve the equations of motion (2.33)-(2.36), which means that *AREPO* internally alternates between a MHD time step  $\Delta t_{\text{MHD}}$  and a Braginskii viscosity time step  $\Delta t_{\text{Brag}}$ . Since the viscosity tensor  $\boldsymbol{\Pi}$  only enters the momentum and the energy equation (see section 2.3.5), only such viscous terms need to be solved by the algorithm, which reduce to

$$\rho \frac{\partial \mathbf{v}}{\partial t} = -\nabla \cdot \boldsymbol{\Pi}, \quad (2.57)$$

$$\rho \frac{\partial \epsilon}{\partial t} = -\nabla \cdot (\boldsymbol{\Pi} \cdot \mathbf{v}), \quad (2.58)$$

while the density and the magnetic field are kept constant during the Braginskii time step. In order to solve equations (2.57) and (2.58) in *AREPO*, [Berlok et al. \(2019\)](#) define a local coordinate system with basis vectors  $\mathbf{e}_n$ ,  $\mathbf{e}_m$  and  $\mathbf{e}_p$  at each interface between two Voronoi cells for the non-trivial spatial discretization on a moving mesh. Additionally, both equations can be rewritten by taking the volume average over a cell of volume  $V$ , such that

$$\frac{1}{V} \int_V \frac{\partial(\rho \mathbf{v})}{\partial t} dV = -\frac{1}{V} \int_V \nabla \cdot \boldsymbol{\Pi} dV = -\frac{1}{V} \int_{\partial V} \boldsymbol{\Pi} \cdot \mathbf{e}_n dA, \quad (2.59)$$

$$\frac{1}{V} \int_V \frac{\partial(\rho \epsilon)}{\partial t} dV = -\frac{1}{V} \int_V \nabla \cdot (\boldsymbol{\Pi} \cdot \mathbf{v}) dV = -\frac{1}{V} \int_{\partial V} (\boldsymbol{\Pi} \cdot \mathbf{v}) \cdot \mathbf{e}_n dA, \quad (2.60)$$

where the surface integrals on the right-hand side are derived by applying the divergence theorem with  $\partial V$  as the surface of the volume and  $dA$  as an infinitesimal area.  $\mathbf{e}_n$  is the unit vector of the local coordinate system and is orientated to be the normal to the interface between the two Voronoi cells. The right-hand side of both equations (2.59) and (2.60) is then approximated as a discrete sum of fluxes through the faces of the Voronoi cell ([Berlok et al., 2019](#)). Thereby, a quantity  $\phi$  or its derivative is estimated at each interface of a Voronoi cell by taking a weighted harmonic mean of its values at all the corners of this cell,

$$\frac{\partial \phi_{\text{face}}}{\partial x} = \left( \sum_i \frac{w_i}{\partial \phi_i / \partial x} \right)^{-1}, \quad (2.61)$$

where  $w_i$  is the weight of the corner  $i$ . In turn, the gradients  $\partial \phi_i / \partial x$  at each corner are estimated with the corresponding values for neighbouring cells by taking i.e. a least-squares fit of the values of the four adjacent cell centers ([Pakmor et al., 2016](#)).

The anisotropic fluxes for all Voronoi cells are calculated at each Braginskii time step  $\Delta t_{\text{Brag}}$ , which is constrained for an explicit update of viscosity as ([Berlok et al., 2019](#))

$$\Delta t_{\text{Brag}} \leq C \frac{(\Delta x)^2}{2d\nu_{\parallel}}, \quad (2.62)$$

where  $\Delta x = V^{1/3}$  is the minimum size of the cells,  $d = 3$  is the number of spatial dimensions being solved,  $\nu_{\parallel} = \mu/\rho$  is the viscosity coefficient and  $C = 0.3$  is the Courant number, which is defined as the ratio of the applied time step to the allowed time step ([Courant et al., 1928](#)). We can compare the Braginskii time step with the MHD time step constraint given by ([Springel](#),

2010)

$$\Delta t_{\text{MHD}} \leq C \frac{\Delta x}{v_{\max}}, \quad (2.63)$$

where  $v_{\max}$  is the maximum signal speed, which is the sum of the adiabatic sound speed and the Alfvén speed, ergo effectively the flow velocity. Since  $\Delta t_{\text{MHD}} \propto \Delta x$  and  $\Delta t_{\text{Brag}} \propto (\Delta x)^2$ , we can infer that the MHD time step constraint will generally satisfy  $\Delta t_{\text{MHD}} \gg \Delta t_{\text{Brag}}$ . The different scalings become especially crucial for highly resolved simulations, where the explicit Braginskii time step becomes very small. This makes the numerical computations very expensive, because the operator splitting requires that  $\Delta t_{\text{MHD}} = \Delta t_{\text{Brag}}$  in order to advance in time. Therefore, [Berlok et al. \(2019\)](#) implemented a second-order accurate super-time-stepping (STS) method for Braginskii viscosity. STS accelerates the Braginskii viscosity update such that the computational cost scales down to  $\Delta t_{\text{STS}} \propto (\Delta x)^{3/2}$ . However, we have decided for another approach instead by using sub-cycled time steps, which means that the Braginskii viscosity is updated  $n$  times per global MHD time step:  $\Delta t_{\text{MHD}} = n \times \Delta t_{\text{Brag}}$ . Using sub-cycling has the advantage that it works with local time stepping and is thus faster than than STS in our cluster simulations. We have chosen the number of sub-cycles to be  $n = 10$ , which is the same as in [Kunz et al. \(2012\)](#). By restricting sub-cycling properly, we avoid that changes in the system between two consecutive global MHD time steps become too large, because Braginskii viscosity has been updated too many times, which would cause unphysical behaviour following through the remaining time steps.



# Chapter 3.

## Methods

In this work we intentionally focus on the Braginskii-MHD effects in an isothermal cluster atmosphere. The significance of pressure anisotropy can be better understood if testing certain parameters in our simulations is based on a controllable setup. Our first set of simulations, introducing a uniform horizontal magnetic field, aims to reproduce the findings of [Dong and Stone \(2009\)](#), this time applying adaptive mesh refinement (AMR) on a moving Voronoi mesh. The second set of simulations is based on the same simplisitc setup as the first, now enhanced by introducing a turbulent magnetic field. Having different levels of complexity allows us to better assess the qualitative impact of anisotropic viscosity at each step while advancing to more and more realistic cluster properties.

### 3.1. Model Setup

In order to numerically study the evolution and stability of buoyantly rising bubbles in the ICM, we model an idealized, isothermal, relaxed galaxy cluster core. To investigate the effects of Braginskii viscosity, some limitations need to be established as a compromise between a realistic environment and a manageable setup where the underlying physics are more comprehensible. This allows us to isolate the results of Braginskii-MHD in our simulations. Thereby, we follow the cluster setup by [Reynolds et al. \(2005\)](#) and [Dong and Stone \(2009\)](#). The ICM atmosphere is given a density profile described by a beta-profile using  $\beta = 1/2$  as its index,

$$\rho(r) = \rho_0 \left[ 1 + \left( \frac{r}{r_0} \right)^2 \right]^{-\frac{3}{2}\beta}. \quad (3.1)$$

Assuming that the ICM stays in hydrostatic equilibrium, the gravitational potential of the dark matter is fixed by  $\nabla p = -\rho \nabla \Phi$ . Further assuming spherical symmetry and using  $p = c_s^2 \rho$  (see section 2.1.3), we can rewrite equation (2.6) by plugging in the derivative of equation (3.1) to yield

$$\begin{aligned} c_s^2 \frac{1}{\rho} \frac{3\rho_0}{2r_0^2 r} \left[ 1 + \left( \frac{r}{r_0} \right)^2 \right]^{-\frac{7}{4}} &= \frac{d\Phi}{dr} = -g, \\ \frac{3}{2} c_s^2 \int_0^r \frac{r'}{(r'^2 + r_0^2)} dr' &= \int_0^r d\Phi. \end{aligned}$$

Finally, by performing the integral we get an expression for the gravitational potential for our cluster model ([Reynolds et al., 2005](#))

$$\Phi(r) = \frac{3}{4} c_s^2 \log(r'^2 + r_0^2) \Big|_0^r = \frac{3}{4} c_s^2 \log \left[ 1 + \left( \frac{r}{r_0} \right)^2 \right]. \quad (3.2)$$

The gravitational forces (dominated by dark matter) acting on each grid cell in our ICs are fixed by using this analytical potential throughout the simulations presented in table 3.3.

We choose units of mass, length and velocity such that  $\rho_0 = 1$ ,  $r_0 = 1$  and  $v_0 = 1$  in the code. Our simulations have been run in a cubic box that spans a spatial domain of  $6r_0$  in

each dimension. The origin of the gravitational potential coincides with the center of the box at  $r/r_0 = \sqrt{x^2 + y^2 + z^2} = 0$ . We consider an ideal gas with adiabatic equation of state with  $\gamma = 5/3$ . The initially static cluster atmosphere gets carved out by two underdense spherical regions, symmetrically aligned along the vertical  $y$ -axis. Such a bubble is displaced from the center of the dark matter potential by a distance  $R = 0.3 r_0$  with radius  $r_{\text{bub}} = 0.25 r_0$  and density  $\rho_{\text{bub}} = 0.01 \rho_0$ . Hence, our ratio  $R/r_{\text{bub}} = 1.2$  is in good agreement with statistical data from observations ([Rafferty et al., 2006](#)). The bubble profile smoothly changes from the reduced values inside the bubbles to the quiescent ambient gas for all number of cells  $N$  via an analytical profile given by

$$\rho_i = \rho_{\text{bub}} + \frac{1}{2} \left( 1 + \tanh \left( \frac{r_i - r_{\text{bub}}}{a} \right) \right) (\rho_i - \rho_{\text{bub}}) \quad \forall i \in [0, N], \quad (3.3)$$

where  $r_i = \|\mathbf{r}_i - \mathbf{r}_{\text{bub}}\|$  is the distance of the  $i$ -th grid cell to the closest bubble center,  $r_{\text{bub}} = \|\mathbf{r}_{\text{bub}}\|$  is the bubble radius,  $a$  is a smoothing parameter and  $\rho_i$  is the density of the  $i$ -th cell. Local pressure equilibrium is maintained by setting the initial pressure of the bubbles to the initial pressure of the ICM at that radius, meaning that the bubbles become hotter than their surroundings by a factor of  $T_{\text{bub}} = 100 T_{\text{amb}}$ . This results in an ICM with constant internal energy. The radially averaged profiles for density, thermal pressure and temperature are plotted in figure 3.1.

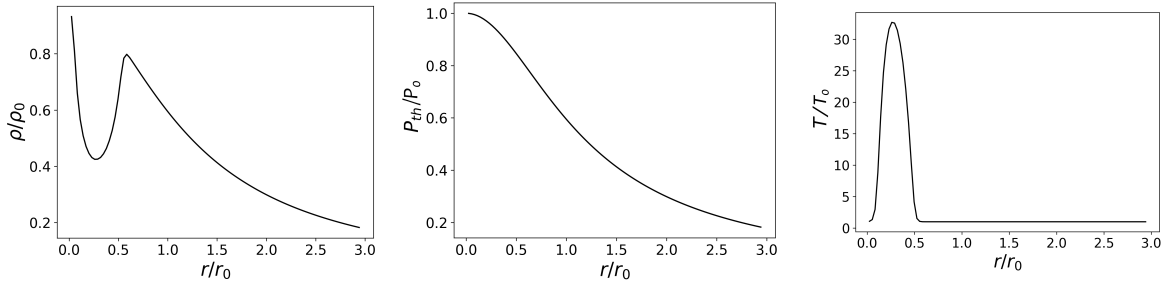


Figure 3.1.: Radial profiles of our ICs for a uniform magnetic field at  $t/t_0 = 0$ . Plotted from left to right are the volume-weighted density  $\rho$ , the volume-weighted thermal pressure  $P_{\text{th}}$  and the mass-weighted temperature  $T$ . The artificially carved out low-density, hot bubbles are set in pressure equilibrium and can be clearly seen centered at  $r = \pm 0.3 r_0$ .

The evolution of the bubbles is computed by solving the equations of three-dimensional Braginskii-MHD (see section 2.3.5) using the moving-mesh code *AREPO* ([Springel, 2010](#)), see section 2.4 for implementation details.

We are going to relate our code units to quantities of real clusters in order to be able to assess our findings with physical meaning and to make the following in analysis more quantitative. Therefore, we adopt fiducial values for length, mass and time following [Dong and Stone \(2009\)](#). We fix the unit of length to  $r_0 = 80 \text{ kpc}$  being equivalent to the core radius, the unit of density to a proton number density of  $\rho_0 = 0.03 m_p \text{ cm}^{-3}$  and the unit of velocity to  $v_0 = 800 \text{ km s}^{-1}$  being equivalent to the isothermal sound speed. Having fixed these units already implies setting the units of mass and time. Additionally, physical units allow us to derive general characteristics of our cluster model like the virial mass  $M_{200}$ , virial radius  $r_{200}$ , the sound crossing time  $t_{\text{sc}}$  or the thermal pressure scale height  $H$ . Those are presented in table 3.1. A core radius of 80 kpc was chosen as a compromise between staying close to the setup by [Dong and Stone \(2009\)](#) while initializing the bubble radius to 20 kpc to be comparable with the jet-inflated bubbles simulated by [Ehlert et al. \(2018\)](#). Other studies with numerical simulations of buoyantly rising bubbles based on an isothermal (double) beta profile use core radii with i.e. 200 kpc ([Brüggen and Kaiser,](#)

2001), 50 kpc (O'Neill and Jones, 2010) or 100 kpc (Gilkis and Soker, 2012).

The total mass of a cluster within the virial radius can be calculated using the expression for  $M(r)$  derived from hydrostatic equilibrium in equation (2.7). There, the gradient in temperature vanishes assuming an isothermal cluster profile. Since the gas density is well described by a  $\beta$ -model, we can simply derive  $d \ln \rho_g(r)/dr = -3\beta r/(r^2 + r_0^2)$  and plug in  $r = r_{200}$  to get the total mass enclosed within the viral radius:

$$M(r_{200}) = \frac{3\beta k_B T r_{200}}{G \mu m_p} \frac{(r_{200}/r_0)^2}{1 + (r_{200}/r_0)^2} \quad (3.4)$$

In section 2.1.4 the virial radius  $r_{200}$  has been defined as the radius, within the mean gas density equals 200 times the critical density of the universe, ergo  $M(r_{200})/V(r_{200}) = 200 \times \rho_c$ , where  $\rho_c$  is given by  $\rho_c = 3H_0^2/8\pi G \approx 1.88 \times 10^{-29} h^2 \text{ g cm}^{-3}$ . Here,  $H_0$  is the Hubble time and  $h$  is the Hubble parameter. With this relation we can calculate  $r_{200}$  as

$$r_{200} = \sqrt{200 \rho_c \frac{3\beta k_B T}{G \mu m_p} \frac{3}{4\pi} - r_0^2}. \quad (3.5)$$

The only term remaining unknown in equations (3.4) and (3.5) is the temperature, which can be expressed as  $k_B T = v_0^2 \mu m_p = 3.34 \text{ keV}$ . The resulting quantities describing a pseudo-realistic galaxy cluster are shown in table 3.1. They are in agreement with the properties which have been discussed throughout chapter 2. The simulations presented in this thesis span a cubic box with size  $(480 \text{ kpc})^3$  and the target mass of the cells of the ambient gas is about  $6 \times 10^5 \text{ M}_\odot$ . For our fiducial run the numerical resolution of the cells inside the bubble region is about 0.5 kpc, which is about equal to the mean free path of the ions  $\lambda_{\text{mfp}}$  we estimated in equation (2.21). The latter in turn is comparable to the viscous dissipation scale  $l_{\text{visc}} \sim 1 \text{ kpc}$  for a Reynolds number of  $\text{Re} = 50$  (see section 2.3.3). Thus, we have established the following relation,

$$V_{\text{target},0}^{1/3} \sim \lambda_{\text{mfp}} \sim l_{\text{visc}}. \quad (3.6)$$

$r_0$	80 kpc
$\rho_0$	$0.03 m_p = 5 \times 10^{-26} \text{ g cm}^{-3}$
$v_0$	$800 \text{ km s}^{-1}$
$t_0$	98 Myr
domain space	$(480 \text{ kpc})^3 = (6 r_0)^3$
resolution	number of cells
highest res	$7 \times 10^7$
fiducial res	$2 \times 10^7$
lower res	$7 \times 10^6$
$V_{\text{target},0}^{1/3}$	$0.48 \text{ kpc} = 6 \times 10^{-3} r_0$
$m_{\text{target},0}$	$5.9 \times 10^5 \text{ M}_\odot$
$k_B T_0$	$3.34 \text{ keV} = 3.88 \times 10^7 \text{ K}$
$r_{200}$	1.5 Mpc
$M(< r_{200})$	$3.3 \times 10^{14} \text{ M}_\odot$
$H$	107 kpc
$g(r_0)$	$2 \times 10^{-8} \text{ cm s}^{-2}$

$t_{\text{sc}}(r_{200})$	1.8 Gyr	
$t_{\text{sc}}(3 r_0)$	0.3 Gyr	
$t_{\text{buoy}}$	130 Myr	
$t_{\text{cool}}$	1.8 Gyr	
$\nu_0$	$\nu_{\parallel}$	$\text{Re}$
0.01	$1.98 \times 10^{29} \text{ cm}^2 \text{ s}^{-1}$	50
0.001	$1.98 \times 10^{28} \text{ cm}^2 \text{ s}^{-1}$	500
Spitzer	$4.6 \times 10^{28} \text{ cm}^2 \text{ s}^{-1}$	420
$\beta$	$\ \mathbf{B}\ $	$k_{\text{inj}}$
$10^6$	$0.1 \mu\text{G}$	-
100	$9.0 \mu\text{G}$	$37.5^{-1} \text{ kpc}^{-1}$

Table 3.2.: Fixing physical parameters that characterize the ICM, continued.

Table 3.1.: Fixing physical parameters that characterize the ICM.

We study two different initial magnetic field configurations, firstly a uniform horizontal field  $\mathbf{B} = (B_0, 0, 0)$  and secondly a turbulent field with constant plasma beta. For each field geometry

we study two different magnetic field strengths, one with a weak field given by  $\beta = 10^6$  and one with a strong field given by  $\beta = 100$ . Calling the latter setup *strong* might be a bit misleading since the magnetic pressure is still 100 times weaker than the thermal pressure, but it is convenient to do so in order to clearly distinguish both. The plasma beta can be converted into physical field strength  $\|\mathbf{B}\|$  in terms of Gauss using equation (2.25), which are presented in table 3.2. Field strengths ranging between  $0.1 - 9 \mu\text{G}$  are representing reasonable cluster properties (Carilli and Taylor, 2002). For the turbulent magnetic field an injection scale is introduced,  $k_{\text{inj}}$ , such that the coherence length is of order the bubble size, such that  $2\pi/k_{\text{inj}} \sim L$ . This is quite important since whether the magnetic fields is able to stabilize a buoyantly rising bubble depends on the coherence length of the field (Ruszkowski et al., 2007). They find that if the coherence length is smaller than the bubble radius, no useful draping layer can form at the bubble front and the bubble is getting dissolved by KHIs and RTIs.

Furthermore, we study two different values for the anisotropic diffusion coefficient of Braginskii viscosity, which are also shown in table 3.2. Following Dong and Stone (2009), the dynamic viscosity is fixed as a diffusion constant  $\mu = \nu_0$  (see section 2.3.4) to give a Reynolds number  $\text{Re} = v_0 r_0 \rho_0 / 2\nu_0 = 50$ , where in code units  $v_0 = r_0 = \rho_0 = 1$  such that  $\nu_0 = 0.01$ . Here, the characteristic velocity is  $v_0/2$ . Using the same value for  $\nu_0$  allows for direct comparison later on. The physical units of this diffusion constant are then simply achieved by an unit conversion as  $\nu_{\parallel} = \nu_0 (r_0^2/t_0)$ . For our fiducial simulations we take  $\nu_0 = 0.01$ , which yields  $\nu_{\parallel} \approx 2 \times 10^{29} \text{ cm}^2 \text{ s}^{-1}$ . It is insightful to compare the Reynolds number of our isothermal setup to the Reynolds number of a CC having the Spitzer value of viscosity. The temperature dependent Spitzer value can be derived from equation (2.30),

$$\nu_{\parallel} = \frac{2.2 \times 10^{-15}}{\ln \Lambda} \left( \frac{T}{T_0} \right)^{5/2} \frac{\rho_0}{\rho} \text{ cm}^2 \text{ s}^{-1},$$

where we substitute

$$\left( \frac{T}{T_0} \right) = \frac{m_p}{2} \frac{(p/p_0)}{(\rho/\rho_0)},$$

which yields  $\nu_{\parallel} \approx 1.4 - 7.8 \times 10^{28} \text{ cm}^2 \text{ s}^{-1}$  at the very cluster center ( $r/r_0 = 0$ ) and at the outer radii ( $r/r_0 = 3$ ), respectively. From this we can estimate the Spitzer Reynolds number with quantities in accordance with our presented setup at the cluster core:

$$\text{Re}_{\text{sp}} \left( \frac{r}{r_0} = 0 \right) \approx 720 \left( \frac{v_L = v_0/2}{400 \text{ km/s}} \right) \left( \frac{L = r_0}{80 \text{ kpc}} \right) \left( \frac{n_0}{0.03 \text{ cm}^{-3}} \right) \left( \frac{T_0}{3.88 \times 10^7 \text{ K}} \right)^{-5/2} \quad (3.7)$$

Looking at radii further out with lower density, the cluster atmosphere becomes less turbulent and the Reynolds number decreases accordingly down to  $\text{Re}_{\text{sp}}(r/r_0 = 3) \approx 130$ , which implies a naive mean Reynolds number of  $\text{Re}_{\text{sp}} \approx 420$ . Our estimated range of Reynolds numbers inferred from Spitzer viscosity is not in good agreement with estimates of Reynolds et al. (2005); Dong and Stone (2009) modelling the hot bubble gas for the Perseus cluster core region,

$$\text{Re} \approx 62 \left( \frac{v_L}{390 \text{ km/s}} \right) \left( \frac{L}{20 \text{ kpc}} \right) \left( \frac{n}{0.03 \text{ cm}^{-3}} \right) \left( \frac{T}{5.81 \times 10^7 \text{ K}} \right)^{-5/2}, \quad (3.8)$$

neither with estimates of Rosin et al. (2011) modelling the plasma in the core of Hydra A,

$$\text{Re} \approx 60 \left( \frac{v_L}{250 \text{ km/s}} \right) \left( \frac{L}{6.5 \text{ kpc}} \right) \left( \frac{v_{\text{th}}}{700 \text{ km/s}} \right)^{-1} \left( \frac{\lambda_{\text{mfp}}}{0.04 \text{ kpc}} \right)^{-1}, \quad (3.9)$$

nor with the estimate we derived based on recent observational data from *Hitomi* in equation (2.32). However, the Reynolds number varies considerably i.e. with the chosen length scale and therefore with the set of fixed units. So for instance, if we would just double the initial temperature, we would get a new mean Spitzer Reynolds number of  $Re_{\text{sp}} \approx 75$  according to equation (3.7), which is already in good agreement with the above estimates of other studies.

We study the results of a set of simulations listed in table 3.3. The fiducial run is highlighted in boldface, which runs a model using a uniform horizontal magnetic field throughout the domain, initially with a very weak magnetic field strength of  $\beta = 10^6$  and in turn a reasonable strong (compared to the Spitzer value) anisotropic viscosity coefficient of  $\nu_0 = 10^{-2}$ , which results in an ICM about 8 times as viscous as the mean Spitzer value. We have also run a similar simulation with the same magnetic field configuration, but with a ten times smaller viscosity coefficient,  $\nu_0 = 10^{-3}$ , yielding an ICM which is about  $\sim 80\%$  as viscous as the mean Spitzer value.

Label	B-field	$\beta$	$\nu_0$	Re
hydro	...	...	...	...
xB6mhd	Horizontal	1e6	...	...
xB2mhd	Horizontal	100	...	...
tB2mhd	Turbulent	100	...	...
<b>xB6N2</b>	<b>Horizontal</b>	<b>1e6</b>	<b>1e-2</b>	<b>50</b>
xB6N3	Horizontal	1e6	1e-3	500
xB6N2lim	Horizontal	1e6	1e-2 lim	50
xB6N2iso	Horizontal	1e6	Iso 1e-2	50
xB6N3iso	Horizontal	1e6	Iso 1e-3	500
xB2N2	Horizontal	100	1e-2	50
xB2N2lim	Horizontal	100	1e-2 lim	50
xB2N2iso	Horizontal	100	Iso 1e-2	50
tB2N2	Turbulent	100	1e-2	50
tB2N3	Turbulent	100	1e-3	500
tB2N2lim	Turbulent	100	1e-2 lim	50
tB2N2iso	Turbulent	100	Iso 1e-2	50

Table 3.3.: Parameter study of the simulations presented in this thesis. The first letter of each label indicates the magnetic field geometry: uniformly, horizontally aligned (x) or turbulent (t). The second letter refers to the magnetic field strength: weak,  $\beta = 10^6$  (B6) or strong,  $\beta = 10^2$  (B2). The third letter refers to the viscosity coefficient: strong,  $\nu_0 = 10^{-2}$  (N2) or weak,  $\nu_0 = 10^{-3}$  (N3). The last syllable indicates whether the Braginskii viscosity is limited (lim) or isotropic (iso).

### 3.1.1. Magnetic Field Configuration

The first magnetic field configuration simply contains a field horizontally aligned ( $x$ -direction) throughout the domain (within both the bubbles and the atmosphere), which sets field lines initially perpendicular to the ( $y$ )-direction of the rising bubbles. It is expected that this setup shows a more coherent bubble morphology over time if anisotropic viscosity is included. This is expected because Braginskii viscosity suppresses RTI and KHI along the field lines, thus having Braginskii-MHD should show less instability at the bubble surface in the  $x$ - $y$  plane, parallel to the field. For the strong field simulations the magnetic field strength scales with density as  $B(r) = B(0)(\rho(r)/\rho(0))^{1/2}$  as studies suggest (see section 2.3.3). This means that the ratio of gas to magnetic pressures,  $\beta = 8\pi P_{\text{th}}/B^2$ , is kept constant with height away from the cluster center. Hence, the ambient magnetic field strength generally decreases outwards in the ICM.

The second magnetic field configuration aims for a more realistic approach in modelling the ICM. Here, we generate a Gaussian-distributed, turbulent magnetic field in accordance with the procedure used in Ehlert et al. (2018). We will only describe its most important aspects in this thesis. For further details, we refer to the Appendices of Ehlert et al. (2018) and Ruszkowski

et al. (2007). The initial magnetic field  $\mathbf{B}$  is Fourier transformed based on a Cartesian mesh, while meeting some fundamental constraints.  $\mathbf{B}$  must be divergence-free, such that  $\nabla \cdot \mathbf{B} = 0$ . Each of the three field components  $B_i$  independently follows a one-dimensional power spectrum  $P_{B_i}(k)$  of the form

$$P_{B_i}(k) \propto \begin{cases} k^2, & k < k_{\text{inj}} \\ k^{-5/3}, & k_{\text{inj}} \leq k \end{cases} \quad (3.10)$$

where the power spectrum is defined by  $P_{B_i}(k) \propto k^2 \|\tilde{B}_i(k)\|^2$  with the Fourier transform of each field component  $\tilde{B}_i(k)$ . So,  $\mathbf{B}$  follows a random white noise power spectrum on the largest scales for wave numbers smaller than the injection scale and a Kolmogorov spectrum in the inertial range for  $k \geq k_{\text{inj}}$ . The average field strength is zero ( $\langle \mathbf{B} \rangle = 0$ ). In order to maintain a constant magnetic-to-thermal pressure ratio,  $\mathbf{B}^2$  is scaled at each radius accordingly. The result is plotted in the left panel of figure 3.2. The power spectrum governs the entire computational domain, meaning that also the bubbles contains tangled magnetic field lines instead of a more realistic toroidal configuration. However, the bubble region is magnetically isolated, which can be seen in the right panel of figure 3.2. After creating the turbulent magnetic field, the Cartesian field components are then interpolated onto the adaptive Voronoi mesh of our initial conditions. Therefore, all cell sizes of the Cartesian mesh need to be smaller than the smallest cell size of our IC at any point. Since the spatial domain is quite large, it is not computationally feasible to maintain the highest resolution of the smallest cell for the entire simulation box. Hence, it becomes necessary to combine multiple (in our case two) nested meshes with adaptive mesh resolution in order to be able to perform the individual Fourier transformations.

To ensure pressure equilibrium, the temperature is rescaled adopting temperature fluctuations of the form  $n k_B \delta T = -\delta \mathbf{B}^2 / 8\pi$ . The new IC is then relaxed using Lloyd's algorithm (see section 3.2.1). In fact, relaxing the IC damps some remaining magnetic divergences, but at the same time leads to a reduction of the amplitude of the magnetic field. Although we set the initial velocities to zero, a small random velocity field will be generated soon after the simulation starts due to the Lorentz force of the tangled magnetic field (Yang and Reynolds, 2016b). These induced turbulent gas motions should gradually dissipate over time, thereby decaying magnetic power. Hence, the temperature and  $\mathbf{B}^2$  of our IC are rescaled again to the desired magnetic-to-thermal pressure ratio  $\beta^{-1}$ . We show the final radial profiles of the turbulent configuration in figure 3.3. The small bump at  $r/r_0 = 1.8$  occurs because there is the transition area from the first mesh to the second coarser nested mesh.

## 3.2. Initial Conditions

### 3.2.1. Mesh Relaxation

We relax the meshes of our ICs by using Lloyd's method (Lloyd, 1982) implemented in *AREPO*. The algorithm iteratively constructs a centroidal Voronoi tessellation starting from our Cartesian-like tessellation. This is achieved by moving the mesh-generating points to the center-of-masses of their cells until both coincide after reconstructing the Voronoi tessellation. After some iterations the initial cubic cells are relaxed towards a honeycomb-like configuration, while remaining the same mass density profile, which is shown in figure 3.4. This mesh regularization has been applied as it creates a non-degenerate tessellation, which is computationally more efficient in *AREPO* and it smoothes some of the remaining magnetic divergences. Having cells where the center-of-mass stays close to the mesh-generating point minimizes numerical errors and limits the rate at which mesh faces turn their orientation during mesh motion (Springel, 2010). Hence, an unrelaxed mesh would slow down the numerical computation significantly.

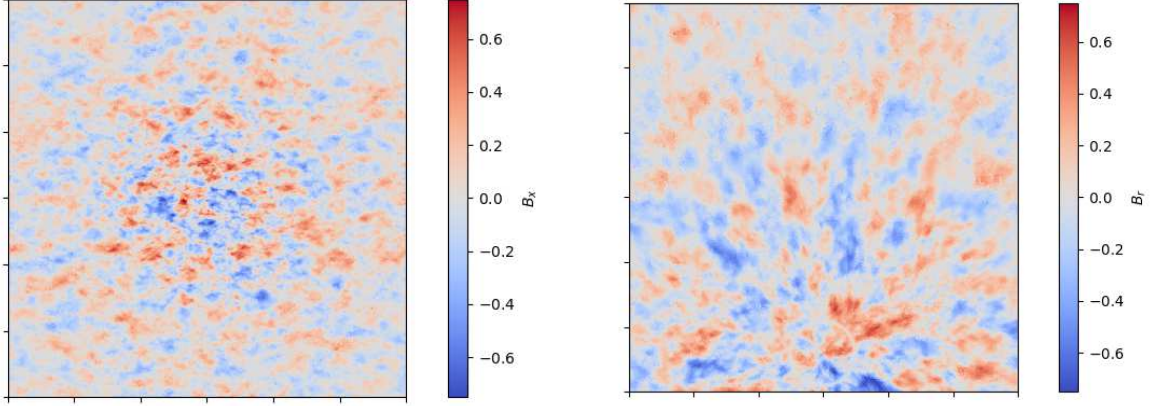


Figure 3.2.: Projected slices of the  $x$ - $y$  midplane for our model  $tB2N2$  at  $t/t_0 = 0$  with mean magnetic field strength  $\|\mathbf{B}\| = 0.5 B_0$ . *Left:* The initial  $x$ -component of the turbulent magnetic field in units of  $B_0 = 18 \mu\text{G}$  for  $\beta = 100$ . The panel spans a spatial domain corresponding to dimensions  $x \in [\pm 3 r_0]$  and  $y \in [\pm 3 r_0]$ . *Right:* Radial component of the turbulent magnetic field,  $\|\mathbf{B}_r\| = \mathbf{r} \cdot \mathbf{B}/\|\mathbf{r}\|$  in units of  $B_0$ , where the radial origin lies at the center of the upper bubble and the magnetic isolation of the bubble region is clearly visible. The panel spans a spatial domain corresponding to dimensions  $x \in [\pm 1.5 r_0]$  and  $y \in [0, 3 r_0]$ . The thin projections in  $z$ -direction have width  $dr = 0.066 r_0$  centered at  $z = 0$ .

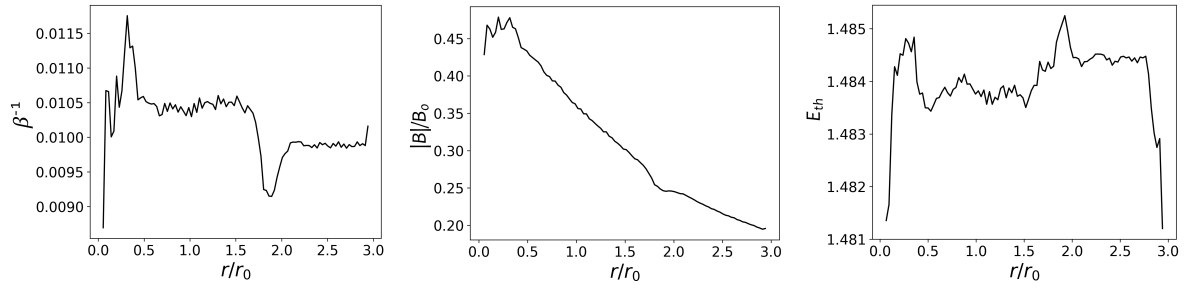


Figure 3.3.: Mass-weighted radial profiles of the initial turbulent magnetic field after rescaling and relaxing the mesh but before setting the bubbles. *Left:* On average constant magnetic-to-thermal pressure ratio  $\beta^{-1}$  throughout the cluster. *Middle:* Amplitude of the magnetic field  $\|\mathbf{B}\|$  in units of  $B_0 = 18 \mu\text{G}$  with dependence on density such that  $B \propto \rho^{1/2}$ . *Right:* On average constant internal energy (ergo isothermal temperature) throughout the cluster.

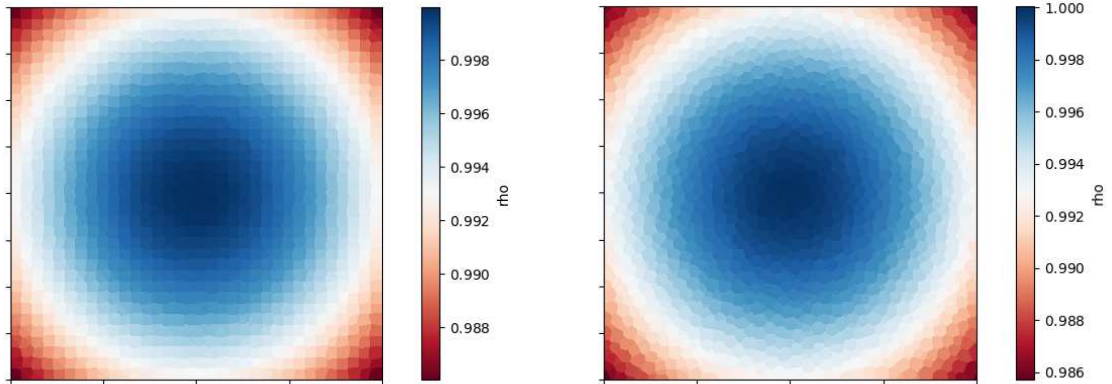


Figure 3.4.: Highly zoomed-in slices of the cluster core with color-coded density in units of  $\rho_0$ . *Left:* The initial non-relaxed grid at  $t/t_0 = 0$  consists of nearly perfect cubic cells, whose perpendicular edges would be numerically challenging in *AREPO*. *Right:* After applying the Lloyd's algorithm for some time ( $t/t_0 = 0.1$ ), the relaxed mesh looks much more optimized while its Voronoi cells try to retain a honeycomb-like shape. Both slices span a spatial domain corresponding to dimensions  $x \in [-0.1 r_0, 0.1 r_0]$  and  $y \in [-0.1 r_0, 0.1 r_0]$ .

### 3.2.2. Passive Scalars and Refinement Criteria

In order to be able to identify the bubble during its evolution, a passive scalar,  $X_{\text{bub}}$ , is used. It traces the fluid motions by recording the mass fraction of the bubble material in each Voronoi cell.  $X_{\text{bub}}$  is initially set to one within the bubble region and zero everywhere else in the simulation domain such that  $X_{\text{amb}} = 1 - X_{\text{bub}}$ . The transition layer between bubble and ambient gas is given a smoothly varying analytical profile for all number of grid cells  $N$ ,

$$X_{\text{bub},i} = \frac{1}{2} \left( 1 + \tanh \left( -\frac{r_i - r_{\text{bub}}}{a} \right) \right) \quad \forall i \in [0, N], \quad (3.11)$$

where  $r_i = \|\mathbf{r}_i - \mathbf{r}_{\text{bub}}\|$  is the distance of the  $i$ -th grid cell to the closest bubble center,  $r_{\text{bub}} = \|\mathbf{r}_{\text{bub}}\|$  is the bubble radius and  $a$  is a smoothing parameter. We have tested several values for  $a$  of otherwise unchanged simulations and could infer that our ICs are quite sensitive to this parameter (see figure A.1 in the appendix). It kind of determines how well the density gradients at the bubble surface are resolved. From this small parameter study we conclude that  $a = 0.1 r_{\text{bub}}$  has yielded the best results in terms of  $X_{\text{bub}}$  mixing. As the bubble evolves, subsequent advection and mixing ensure that cells influenced by the rising bubble can then have fractions of the initial passive scalar values. We treat a Voronoi cell as bubble material if the tracer mass fraction exceeds a certain threshold,  $X_{\text{bub}} > 10^{-3}$ , which is plotted in the left panel of figure 3.5. Throughout this thesis, we refer to a mass fraction of passive scalars and passive tracers interchangeably.

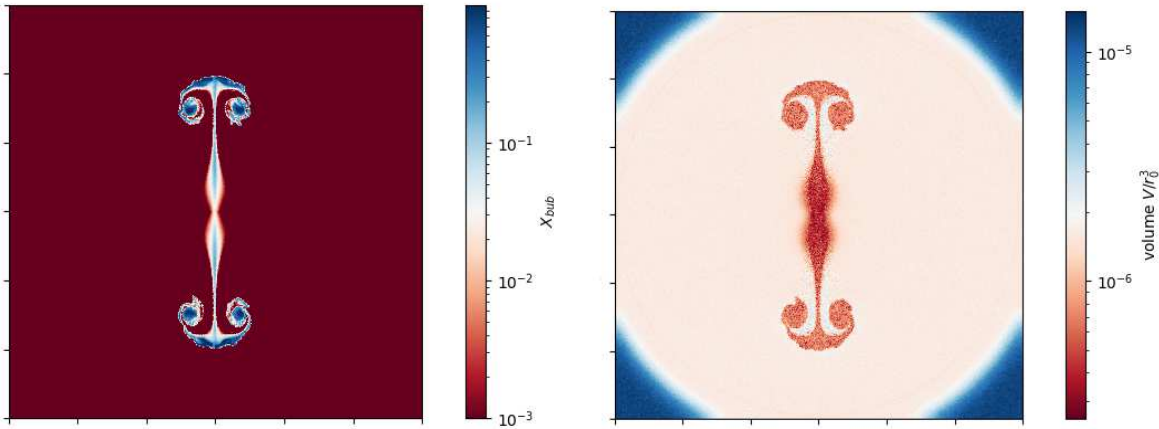


Figure 3.5.: Slices of the  $x$ - $y$  midplane showing the evolved state of the buoyantly rising bubbles at  $t/t_0 = 4$  for the hydrodynamical setup of our highest resolution. Both the passive scalars (left) and the volume of the grid cells (right) are illustrating that the analysis of the bubbles can be nicely traced while minimizing the computational costs by only using higher resolution where it is most needed numerically. Both slices span a spatial domain corresponding to dimensions  $x \in [-3 r_0, 3 r_0]$  and  $y \in [-3 r_0, 3 r_0]$ .

Different refinement criteria for the mesh are used to ensure we resolve the relevant bubble physics on the one hand and to make the computation much more efficient on the other hand. In the default case, the mass of each cell is maintained at a certain specified target mass  $m_{\text{target},0}$  (Vogelsberger et al., 2012). If a cell becomes a factor of two less massive than this threshold, this cell will be derefined (and vice versa). We use the standard criterion in cells belonging to the ambient gas. This creates large Voronoi cells at the cluster outskirts, where the density decreases considerably, which minimizes the computational cost. However, we do not want to have the same refinement criterion for the low-density bubble cells. Here, the default refinement would result in very poorly resolved bubble dynamics. Therefore, we use a volume-based refinement criterion for grid cells, whose tracer mass fraction satisfies  $X_{\text{bub}} > 10^{-3}$ , which is plotted in the

right panel of figure 3.5. If a cell's volume exceeds two times a fixed target volume  $V_{\text{target},0}$ , this cell gets refined. Due to the high density contrast ( $\rho_{\text{bub}}/\rho_{\text{amb}} \sim 10^{-2}$ ), the boundary layer between bubble and ambient cells needs a third refinement criterion, which is based on the steepness of the density gradient  $\|\nabla\rho\|$  as  $V_i^{1/3}\|\nabla\rho\| > 0.5\rho_i$ . The latter two criteria replace the default refinement criterion whenever applicable (see [Weinberger et al. \(2017\)](#) for details). To prevent runaway refinement, a minimum cell volume  $V_{\min}$  is used to restrict each cell's volume to  $V_{\min} = V_{\text{target},0}/2$ . The values of  $m_{\text{target},0}$  and  $V_{\text{target},0}$  are summarized in table 3.1 for our simulations with fiducial resolution.

### 3.2.3. Boundary Conditions

Instead of simple periodic or reflective boundary conditions, we use in-/outflow boundaries at radii  $r/r_0 \gtrsim 3$ . In *AREPO*, these special boundary conditions requires using two types of boundary cells: fluid and solid. The solid boundary cells are implemented into the Voronoi mesh of the spatial domain as a thin spherical shell with width  $dr$  at radii  $3r_0 - dr/2 < r < 3r_0 + dr/2$ . The fluid cells are built up of boundary cells at radii greater than those of the solid boundary layer. Throughout this thesis, we will refer to grid cells belonging to the spatial domain if they are having radii smaller than  $r/r_0 < 3$  for simplicity. We have chosen this type of boundary conditions in order to better maintain hydrostatic equilibrium, which we have had trouble with establishing otherwise (see also section 4.5). Furthermore, using in-/outflow boundaries has the advantage that the fluid state of the fluxes is not simply mirrored at the boundary interface but replaced with a predefined state describing the in-/outflow conditions ([Weinberger et al., 2020](#)). At the solid state, i.e. the vertex velocities are set to zero to guarantee a fixed layer of cells. Both states ensure that on the one hand no de-/refinement criterion will be checked and on the other hand no physical fluxes will be calculated for these cells. The number of cells belonging to our boundary region constitute for  $\approx 27\%$  of the total number of cells of the entire cubic box. This makes our ICs numerically much more efficient since splitting and merging of cells in a Voronoi mesh is computationally quite costly and we avoid unnecessary computational time on solving fluxes for cells, which have no physical relevance.



# Chapter 4.

## Analysis

In this chapter we analyse the simulations of our models summarized in table 3.3. We start with our fiducial run  $xB6N2$ , where we present its bubble evolution in detail by analysing the global morphology in terms of emerging RTI and KHI in section 4.1. Additionally, we discuss its energy contents, the mixing efficiency and how comparable the cooling and heating rates are. Next, we proceed by showing the results of the other simulations we have run. Basically after discussing variations of special interest for the model having uniform magnetic field lines and a very high plasma beta in section 4.2, we move on to the next case where we keep the uniform alignment but increase the magnetic pressure to satisfy  $\beta = 100$ . This corresponds to analysing run  $xB2N2$  in section 4.3. Afterwards, we present model  $tB2N2$  in section 4.4, where  $\beta = 100$  is kept but now a turbulent magnetic field is introduced. In the last section 4.5, we perform a couple of sanity checks and a convergence test in order to verify numerical reliability.

### 4.1. Bubble Evolution

The general evolution of the rising bubble is described in this section for the fiducial run  $xB6N2$  comprising a very weak magnetic field with  $\beta = 10^6$ , horizontally aligned field lines, and a relatively high viscosity coefficient with  $\nu = 10^{-2}$  without limiting the anisotropic pressure. The figure 4.1 shows, from left to right, the tracer mass fraction  $X_{\text{bub}}$ , the density  $\rho$ , the velocity in units of the sound speed  $c_s$ , the kinetic-to-thermal pressure ratio  $X_{\text{kin}} = P_{\text{kin}}/P_{\text{th}}$  and the magnetic-to-thermal pressure ratio  $\beta^{-1} = P_B/P_{\text{th}}$ . As pointed out in section 2.3.2, the cluster atmosphere is stable against convection according to the Schwarzschild criterion, but introducing an underdense bubble close to the center of the gravitational potential will not keep the system static as the bubble represents a high entropy concentration with  $dS/dr < 0$  at these radii. Furthermore, the Schwarzschild criterion only applies to small disturbances of a given equilibrium, which is not the case for an underdense bubble of several kiloparsecs in size. So instead, a simpler argument can be given considering the buoyancy force  $\|\mathbf{F}_{\text{buoy}}\| = -gV_{\text{bub}}(\rho_{\text{amb}} - \rho_{\text{bub}})$ . Since we have  $\rho_{\text{amb}} > \rho_{\text{bub}}$  the buoyancy force is stronger than the gravitational force  $\|\mathbf{F}_{\text{grav}}\| = gV_{\text{bub}}\rho_{\text{bub}}$  and the bubble starts rising buoyantly upwards the cluster potential and ambient gas starts streaming inwards to fill its wake. Thereby, the bubble will adiabatically expand to maintain pressure equilibrium with its surroundings. The shear of velocity flow, which is the velocity difference between bubble and ambient ICM, induces the KHI along the edges of the bubble since the rise velocity is subsonic,  $v/v_0 < 1$ . The motions via KHI are evident in quickly forming vortices. In addition, at the top of the bubble the RTI emerges by tearing the bubble front apart. Both instabilities can already be noticed at  $t/t_0 = 4$ , which later on highly distort the bubble interface. Those lead to turbulent mixing of the bubble material with the surrounding cluster gas until all of it will be diffused into the ICM. The perturbations induced by instabilities grow exponentially with time such that the amplitude  $A \propto \exp(t/\tau)$ . The time-scales for hydrodynamical RTI and KHI,  $\tau_{\text{RT}}$  and  $\tau_{\text{KH}}$  respectively, are given by [Chandrasekhar \(1981\)](#) or by taking the inverse of it

growth rates, e.g. from equation (4.15) for the KHI:

$$\begin{aligned}\tau_{\text{KH}} &= \frac{\rho_{\text{bub}} + \rho_{\text{amb}}}{2\sqrt{\rho_{\text{bub}}\rho_{\text{amb}}}} \frac{1}{\Delta v k} \\ \tau_{\text{RT}} &= \left| \frac{\rho_{\text{bub}} + \rho_{\text{amb}}}{\rho_{\text{bub}} - \rho_{\text{amb}}} \frac{1}{gk} \right|^{0.5}\end{aligned}\quad (4.1)$$

where  $\rho_{\text{amb}}$  is the density of the ambient gas,  $\rho_{\text{bub}}$  is the density of the bubble,  $\Delta v$  is the difference of the shearing velocities at the interface,  $g$  is the gravitational acceleration and  $k$  is the wavenumber of the perturbed length scale. The bubble is expected to survive until  $\lesssim \tau$  and starting to dissolve after that.  $\Delta v$  is sufficiently close to the terminal upward velocity  $v_t$ , which we derived in section 2.2.3 by balancing the drag force with the buoyant force. O'Neill et al. (2009) show that equation (2.18) can be written to sufficient accuracy as  $v_t \approx c_{s,0} \sqrt{r_{\text{bub}}/H}$ , where  $c_{s,0}$  is the sound speed at the cluster center,  $r_{\text{bub}}$  is the bubble radius and  $H$  is the scale height. They also study the evolution of buoyant bubbles in a three-dimensional MHD simulation with artificial bubbles. Applying the initial bubble conditions from O'Neill et al. (2009) into their simplified expression for the terminal velocity yields  $v_t \approx 0.4 c_s$ . Using the relevant values presented in this work (see section 3.1) gives  $v_t \approx 0.44 c_s \approx \Delta v$ . If we plug-in typical values for our fiducial simulation into equation (4.1), such that  $\rho_{\text{bub}}/\rho_{\text{amb}} \approx 10^{-2}$ ,  $\Delta v \approx 0.44 c_s$  and  $g \approx 3 \times 10^{-3} \text{ kpc Myr}^{-2}$ , we get the following time-scales acting on length scales comparable to the bubble size:

$$\begin{aligned}\tau_{\text{KH}} &\approx 280 (k / 20 \text{ kpc})^{-1} \text{ Myr} \\ \tau_{\text{RT}} &\approx 77 (k / 20 \text{ kpc})^{-0.5} \text{ Myr}\end{aligned}\quad (4.2)$$

Based on the time-scales the RTI should evolve  $\sim 3.5$  times faster than the KHI. If we are interested in wavelengths of perturbations close to the size of the bubble, i.e. the KHI should emerge after  $\sim 300 \text{ Myr} \approx 3t/t_0$ . By looking at our hydrodynamical runs in figure 4.24 (at the end of this chapter) we find that this is approximately the case as the bubbles are already disrupted into two relatively symmetrical eddies at  $t/t_0 = 4$ . In fact, the RTI induces circulatory motions within the bubbles, which then get further mixed by secondary KHI along the contact discontinuity. The bubbles show a high level of vorticity and transform into a torus-like structure. This is in accordance with previous findings of simulations with an unmagnetized and inviscid cluster model (Reynolds et al., 2005; Gardini, 2007). The distorted bubbles do not resemble the morphology of X-ray and radio observations of (ghost) cavities and our hydrodynamical model can therefore be excluded from further discussion. However, generally e.g. changing the density contrast or the way the bubble is inflated can substantially alter the outcome of hydrodynamical simulations. That the fiducial run *xB6N2* shows suppressed instabilities in direct comparison is related to the effects of viscosity on the buoyant evolution since stresses from the magnetic field can be neglected. For instance, there are no profound, fully formed vortices visible at  $t/t_0 = 4$  as in the hydrodynamical case, but the bubble is still shredded in a complex manner, although with much less vorticity in its wake. Therefore if the instabilities are not suppressed, the disruption of the bubble occurs much earlier as the vortex flows disturb the central bubble region and push material to either side of it as the bubble is moving upwards the cluster atmosphere. However, the anisotropic viscosity suppresses instabilities only in the direction parallel to the magnetic field lines (Dong and Stone, 2009; Suzuki et al., 2013; Berlok et al., 2019). Hence, we also examine the effects on morphology in the  $y$ - $z$  plane perpendicular to the field presented in figure 4.2. Here, the bubble remains less coherent as in the  $x$ - $y$  plane and gets shredded into distinct pieces. This results in stronger mixing at later times, where small scale structures develop. After a certain time the bubble is not able to confine itself any longer as there is not any surface tension except

for the very weak magnetic field. The bubble splits into two, while parallel to the field the bubble stays more intact. These are clear indications of anisotropic suppression of RTI and KHI. Note that it is ambiguous to define a disruption time of the bubble, which could for instance just depend on the coherence of the bubble front or on the maximum energy deposition into the ICM.

The fluid motions are tracked by the velocity vector field in the middle columns in figure 4.1. At early times the streamlines visualize how the initially static cluster gas starts to flow inwards along the edges of the bubble towards its wake. At later times,  $t/t_0 = 8$ , the streamlines signal a more turbulent flow, showing that the uplifted gas is being disintegrating into the ICM. Looking at both of the outer columns, where the magnetic vector field is plotted, we see that the initially uniform magnetic field lines get bended and dragged along with the rising bubble. As described in section 2.3.2, the fluid is coupled to the magnetic field lines, which are advected with the gas flow. Although the magnetic field is very weak with  $\beta = 10^6$ , it gets locally amplified (damped) where the field lines are getting compressed (stretched). This is shown in the last column in figure 4.1, where the inverse  $\beta$  is plotted. After some time, the magnetic field strength is being amplified by three orders of magnitude especially at the wake, tracing the rising bubble upward the gravitational potential. Here the field lines get stretched the most, thus having the highest magnetic tension forces. In addition, we see bending of field lines at the bubble front via magnetic draping (Dursi and Pfrommer, 2008). But since the magnetic field is so weak, draping effects are not strong enough to stabilize the bubble and suppress RTI. The fourth column shows the kinetic-to-thermal pressure ratio, which is of order unity in the quiescent cluster atmosphere and heavily enhanced for the bubble material, meaning that the bubble dynamics are kinetically driven. The blue shell at the top of the panels looks like a shock front, but it is actually just the boundary layer of our IC, which remains at the same location throughout the simulation (see section 3.2.3). The same quantities are plotted in figure 4.2 for the projected  $y$ - $z$  midplane. At a first glance, they show basically the same picture besides the decomposing morphology of the faster disrupted bubble. If we look for instance more carefully at  $t/t_0 = 2$  for  $X_{\text{bub}}$  and  $\rho$ , we can infer that the bubble slices perpendicular to the uniformly magnetized ICM already show signs of KHI starting to take place, whereas the parallel bubble slice at  $t/t_0 = 2$  in figure 4.1 looks very symmetric, only modified by ram pressure. So Braginskii viscosity does suppress the growth rates of KHIs, but not enough to prevent these macro-scale instabilities from emerging. One detail is also worth mentioning. The trail the rising bubble left behind in its wake is no longer bipolar due to the gas moving with the magnetic field and is probably not a projection effect.

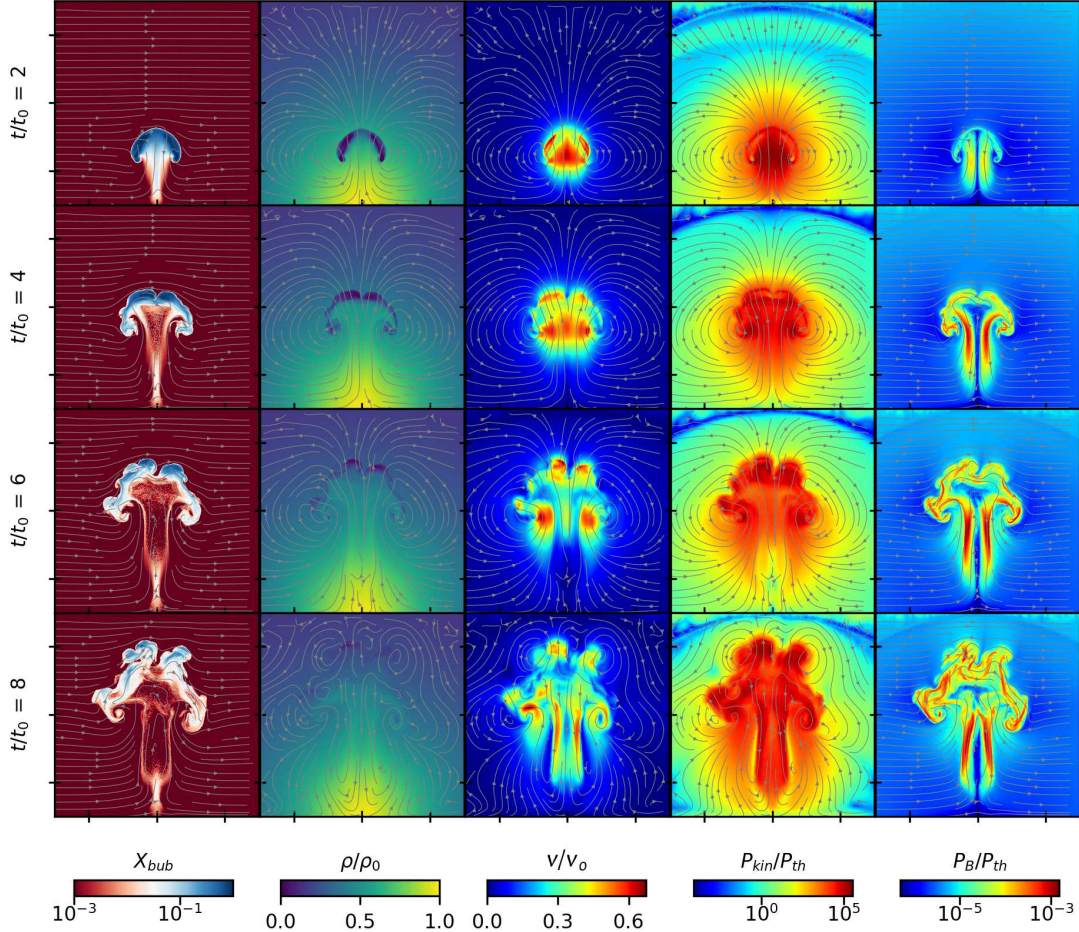


Figure 4.1.: Projected slices of the  $x$ - $y$  midplane parallel to the initially uniform magnetic field lines showing the tracer mass fraction  $X_{\text{bub}}$ , the density  $\rho$ , the velocity in units of the sound speed  $c_s$ , the kinetic-to-thermal pressure ratio  $X_{\text{kin}} = P_{\text{kin}}/P_{\text{th}}$  and the magnetic-to-thermal pressure ratio  $\beta^{-1} = P_B/P_{\text{th}}$  for our fiducial run  $xB6N2$ . Each panel spans a spatial domain corresponding to dimensions  $x \in [-1.5 r_0, 1.5 r_0]$  and  $y \in [0, 3 r_0]$ . The thin projections in  $z$ -direction have width  $dr = 0.066 r_0$  centered at  $z = 0$ . For the tracer mass fraction and the magnetic-to-thermal pressure ratio, the streamlines show the magnetic vector field. For the other three quantities the streamlines show the velocity vector field. Each vector field is presented as a thin projection as well. The color-coding is logarithmically scaled where the colorbar ticks are labeled in power of tens and linear otherwise. The colorbar is fixed for the different times shown.

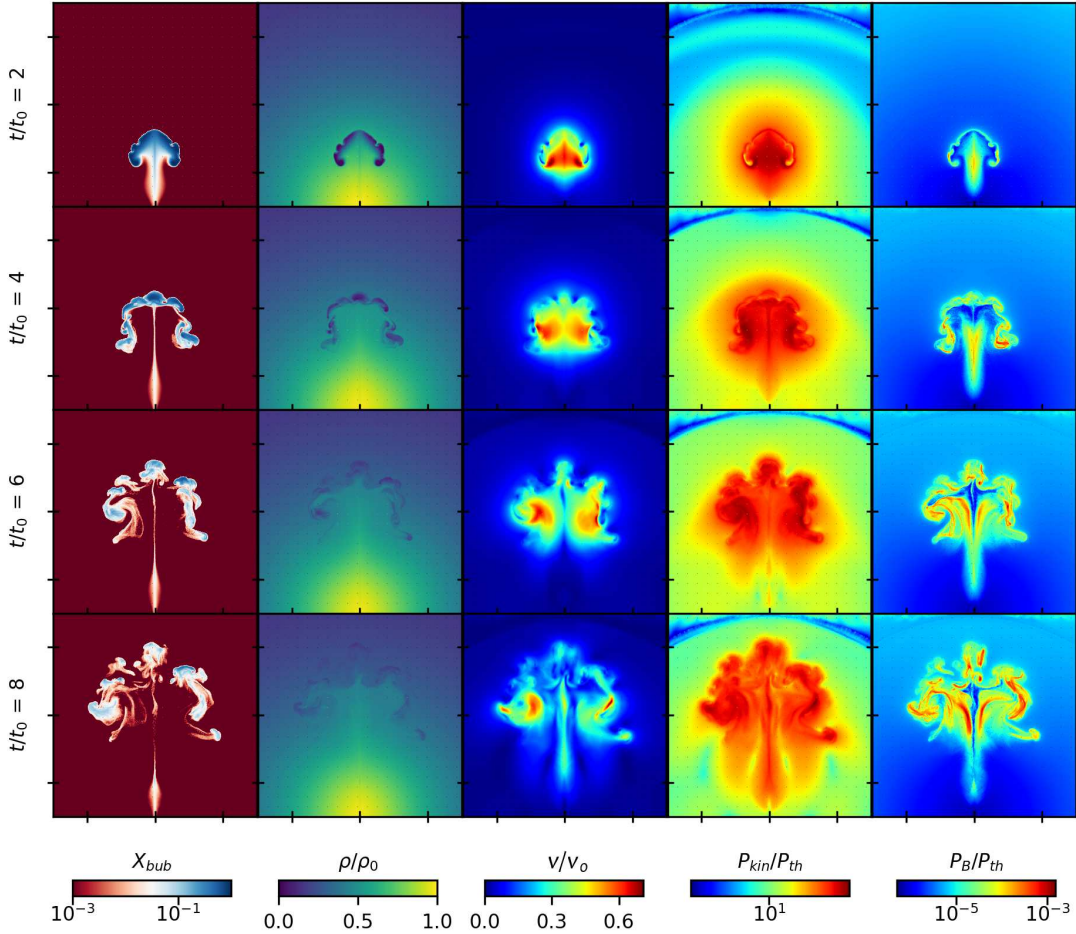


Figure 4.2.: Same quantities as in figure 4.1, but now showing projected slices of the  $y$ - $z$  midplane perpendicular to the initially uniform magnetic field lines. Each panel spans a spatial domain corresponding to dimensions  $x \in [-1.5 r_0, 1.5 r_0]$  and  $y \in [0, 3 r_0]$ . The thin projections in  $x$ -direction have width  $dr = 0.066 r_0$  centered at  $x = 0$ .

#### 4.1.1. Energy Content

The evolution of the energy components for our fiducial run are shown in figure 4.3, where we plot each mean energy density as its ratio to the total energy density,  $\epsilon_{\text{tot}} = \epsilon_{\text{kin}} + \epsilon_{\text{th}} + \epsilon_B$ , which is excluding  $\epsilon_g$  in order to see the ratios in more detail as the amount of gravitational energy is close the total energy. The gravitational energy is thus plotted separately in the fourth column as the difference to its initial value  $\Delta\epsilon_g = \epsilon_g(t) - \epsilon_g(0)$ . We refer to an energy component as an energy by taking  $E_{\text{kin}} = \int_V \rho v^2 dV/2$  for the kinetic energy,  $E_{\text{th}} = \int_V \rho u dV$  for the thermal energy,  $E_B = \int_V B^2 dV/8\pi$  for the magnetic energy and  $E_g = \int_V \Phi \rho dV$  for the gravitational potential energy. To get the mean energy densities we divide those energy terms by the total volume  $V = \int_V dV = 36\pi r_0^3$ .

As previously discussed the magnetic energy gets enhanced at the rim of the bubble but is still negligibly small compared to the other energy terms. Hence, the magnetic field is energetically subdominant in the bulk of the ICM, especially since  $\beta = 10^6$ . The gravitational energy is subtracted by the background potential energy. It can be seen that the bubble front is buoyantly rising upwards the cluster potential, while the bubble interior is not experiencing a gravitational net force. With time the bubble adiabatically expands and mixes with the ambient ICM. This is slowing down the terminal speed of the lobe due to loss of momentum to the ambient gas and

due to loss of buoyancy force because of the increased density. The thermal and kinetic energy ratios look quite similar, although being inverse to each other. The kinetic fraction just provides up to about 12% of the total energy, while contribution of thermal energy never falls below 88%. The kinetic energy contribution decreases with time throughout the bubble material. We expect the kinetic energy being converted into thermal energy on time-scales that are resolved by our simulation. This can not be clearly inferred by looking at the panels in figure 4.3, but is becoming more evident by comparing the left and right subfigures of 4.4 though. For the former, we plot the energies volume averaged over the entire spatial domain as a function of time. We do the same for the latter, but restrict the energy averages to Voronoi cells identified as bubble material. A cell is classified as a bubble cell if the tracer mass fraction exceeds a certain threshold:  $X_{\text{bub}} > 10^{-3}$ . We can see that after  $t/t_0 \approx 2$  the bubble starts loosing kinetic energy continuously while the thermal energy increases. This is an indication for heating, which will be discussed later on in section 4.1.3. However, the conversion only appears in the bubble itself since the bulk of the ICM stays relatively unaffected from a energetic point of view (see figure 4.4).

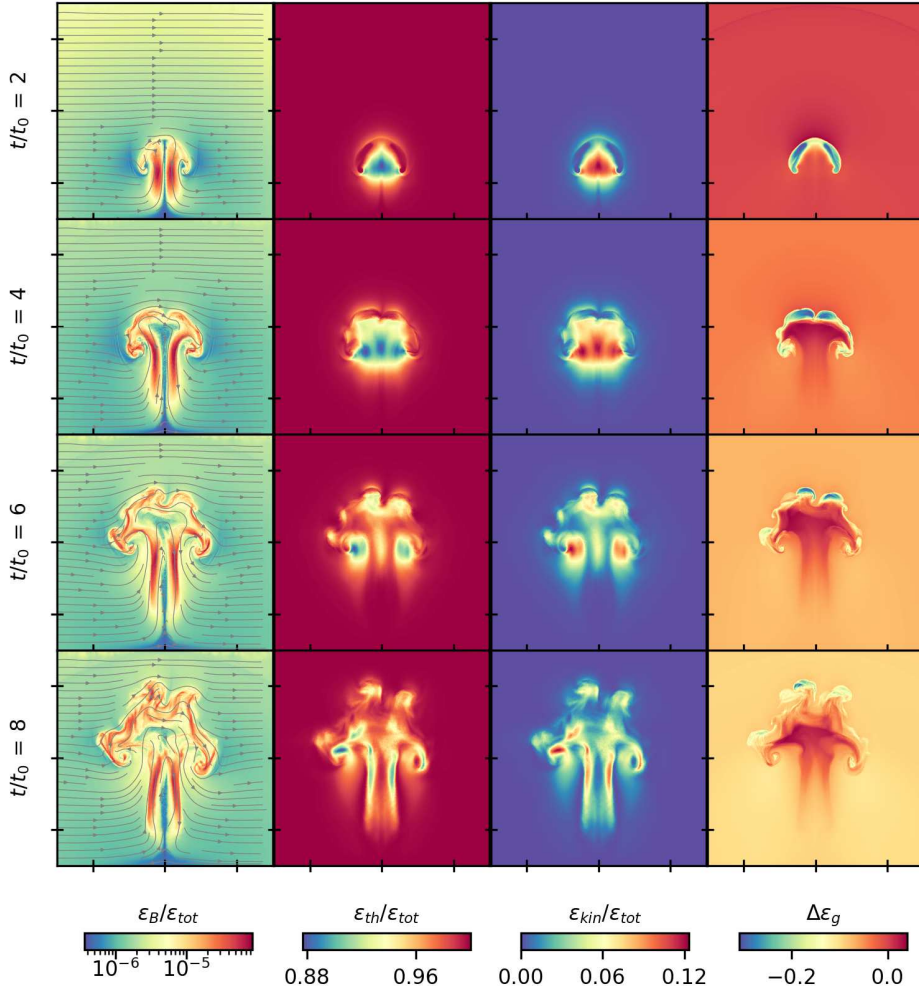
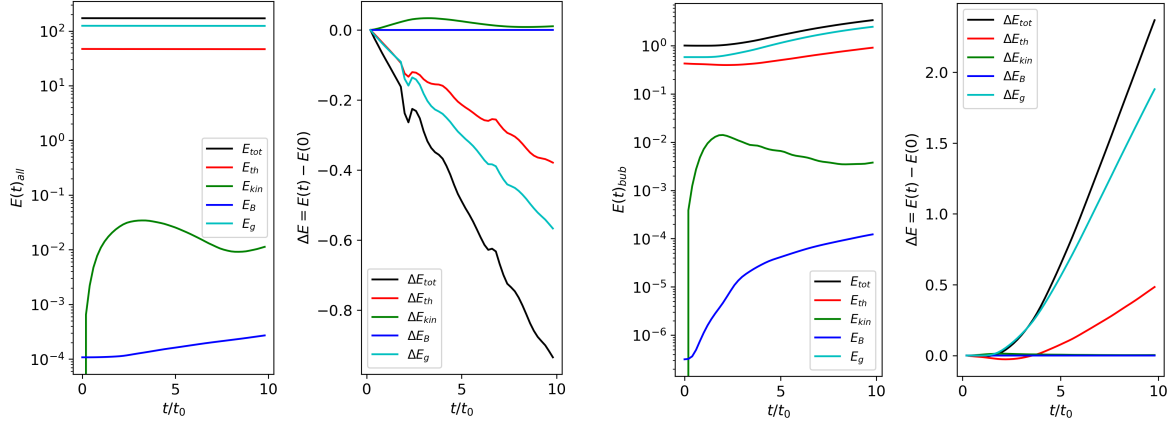


Figure 4.3.: Projected slices of the  $x$ - $y$  midplane parallel to the initially uniform magnetic field lines for our fiducial run  $xB6N2$  showing from left to right the magnetic energy density, thermal energy density and kinetic energy density normalised to the total energy density, whereas the latter is shown in the fourth column as the difference to its initial value  $\Delta\epsilon_g = \epsilon_g(t) - \epsilon_g(0)$ . Each panel spans a spatial domain corresponding to dimensions  $x \in [-1.5 r_0, 1.5 r_0]$  and  $y \in [0, 3 r_0]$ . The thin projections in  $z$ -direction have width  $dr = 0.066 r_0$  centered at  $z = 0$ .



(a) *Left:* Evolution of total energy  $E_{tot}$  and its energy components volume-averaged over time covering the entire spatial domain within  $r/r_0 < 3$ . *Right:* Relative energy changes at each time  $t$  such that  $\Delta E(t) = E(t) - E(0)$  is the energy component subtracted by its initial value.

(b) Same as in the left subfigure, now limited to the bubble region, where the latter is defined as the number of cells exceeding  $X_{\text{bub}} > 10^{-3}$ .

Figure 4.4.

### 4.1.2. Mixing

As discussed in a previous section, a buoyantly rising bubble is going to get distorted and eventually mixed with the quiescent ambient gas sooner or later depending on the level of viscosity or the strength of the magnetic field. One way to quantify the fraction of mixed gas is to compute the volume covering fraction, which we will show in figure 4.25 for the convergence study in section 4.5. Another way to estimate mixing is to compute the gas clumping factor  $C_\rho$ , which is a measurement of how density varies within a gaseous medium. The peaks of a clumping factor distribution represent gas clumps and can be interpreted as perturbations from the smooth gas density profile. The gas clumping factor is defined by averaging the cluster density profile within radial shells of constant width from the cluster center (Vazza et al., 2013):

$$C_\rho(r) = \frac{\int_\Omega \rho^2(r)d\Omega}{\left(\int_\Omega \rho(r)d\Omega\right)^2} = \frac{\langle \rho^2 \rangle_\Omega}{\langle \rho \rangle_\Omega^2} \geq 1, \quad (4.3)$$

where  $\Omega$  is the solid angle of a sphere. A homogeneous ICM with a smooth gas density distribution is considered to be not clumpy ( $C_\rho = 1$ ). However, X-ray analyses of galaxy clusters show that the gas density inferred from the X-ray surface brightness is overestimated by  $\sim \sqrt{C_\rho}$  if the ICM is clumpy. We note that averaging within spherical shells in our model setup might not be a good approximation since introducing bubbles in a homogeneous ICM breaks the spherical symmetry in the cluster. As Vazza et al. (2013) point out, a high gas clumping factor does not necessarily imply an increased presence of dense gas clumps, especially since we are not investigating distributed gas clumps which have formed due to accretion or mergers. However, we can rewrite equation (4.3) as a measure of the density variation of the ICM such that  $C_\rho$  is related to the variance and mean of the density as

$$C_\rho = \frac{\langle \rho^2 \rangle}{\langle \rho \rangle^2} = \frac{\langle \rho^2 \rangle - \langle \rho \rangle^2}{\langle \rho \rangle^2} + 1 = \frac{\langle (\rho - \langle \rho \rangle)^2 \rangle}{\langle \rho \rangle^2} + 1 = \frac{\text{Var}(\rho)}{\langle \rho \rangle^2} + 1, \quad (4.4)$$

where we omit  $\Omega$  for brevity. The mass-weighted gas clumping factor is shown on the left in figure 4.5. We plot  $C_\rho$  of the entire cluster for our fiducial run  $xB6N2$  at several times and compare it with the hydrodynamic simulation. Based on the peaks, we can infer until which radius the bubble has risen at each time given. The width of each distribution indicates how spread the bubble has become. We see that the bubble of the Braginskii run slows down due to anisotropic viscosity and only reaches out to  $r/r_0 \approx 2.5$  with its bubble front at time  $t/t_0 = 8$  while most of the bubble gas lies at  $r/r_0 \approx 1.8$ . In the hydrodynamical case, the bulk of the bubble material reaches out to  $r/r_0 \approx 2.5$  after the same time. Overall,  $C_\rho$  stays close to one at all times. The amplitudes of both samples peak roughly at the same clumping factors at each time, shifted to larger radii for *hydro*. We expected a slightly different result with  $xB6N2$  having higher clumpiness throughout the simulation, because Braginskii viscosity should damp some fluid motions from being mixed with the quiescent ICM. Instead, the left panel of figure 4.5 suggests that our viscosity driven run displays approximately the same amount of mixing as the inviscid control run. Visual comparison of figures 4.24 and 4.1 however indicate that there is less mixing in the Braginskii run than in the hydrodynamical run. Hence, using the gas clumping factor to assess the amount of mixing for an unstable rising bubble might not be very reliable and we will not continue with a deeper analysis. That the final clumpiness does not differ much is probably related to the anisotropic suppression of instabilities as the bubble rises. We have already described that the bubble is less coherent in the  $y$ - $z$  plane perpendicular to the magnetic field for our fiducial run (see figure 4.2). That is possibly why our overall picture of clumpiness is relatively vague to interpret, because the torus-like shape of an evolved bubble in a hydrodynamical environment and effects due to anisotropic viscosity might result in comparable gas clumping factors when averaging over radial shells. Furthermore, changes in density do not have to necessarily occur due to mixing. In fact, the cluster density is also affected by soundwaves and adiabatic expansion or compression of gas.

Therefore, we quantify mixing next by avoiding using a method based on averaging radial shells. We achieve this by plotting the entropy of the tracer mass fraction  $X_{\text{bub}}$  as a function of time on the right in figure 4.5. This method is described by Lecoanet et al. (2016), where they introduce a dye concentration in their simulations, which is analogous to passive scalars used in this thesis. Both quantities range from 0 to 1. So the local fraction of dye particles is similar to our tracer mass fraction  $X_{\text{bub}}$ , except that Lecoanet et al. (2016) add a diffusion term in the equation for the evolution of the dye concentration. Although we do not have such a term in our set of Braginskii-MHD equations, we can still take advantage of using the dye since we are only interested in the volume-integrated dye entropy  $S = \int \rho s dV$ . The dye entropy per unit mass is defined as  $s = -X_{\text{bub}} \ln X_{\text{bub}}$  (Lecoanet et al., 2016) and the total dye mass is given by

$$M_X = \int_V \rho X_{\text{bub}} dV. \quad (4.5)$$

To make the total entropy unitless, we divide  $S$  by its maximum entropy  $S_{\max} = -X_{\text{bub}}^* \ln X_{\text{bub}}^* \int \rho dV$ , where  $X_{\text{bub}}^* = \int \rho X_{\text{bub}} dV / \int \rho dV = M_X/M$ . The maximum entropy represents the fluid state where the dye concentration is fully mixed within the fluid. We find that a fully mixed cluster would have  $X_{\text{bub}}^* = 0$ , while a completely unmixed fluid with  $X_{\text{bub}} = 0$  or  $X_{\text{bub}} = 1$  everywhere has zero dye entropy. We show the evolution of  $S/S_{\max}$  in the right panel of figure 4.5. We infer that our hydrodynamical model shows higher entropy compared to our Braginskii run, which indicates higher level of mixing. The ICM of  $xB6N2$  becomes to 33% fully mixed at  $t/t_0 = 8$ , while the inviscid run reaches 37 percent of its maximum dye entropy. It becomes much clearer now that anisotropic viscosity suppresses mixing of a buoyantly rising bubble by evaluating the dye entropy budget of the cluster than by plotting the clumping factor. Note that  $S/S_{\max}$  is not

zero at  $t/t_0$ , because our bubble has an analytical profile for the tracer mass fraction initially, which smoothly transitions from  $X_{\text{bub}} = 0$  to  $X_{\text{bub}} = 1$  (see equation (3.11)).

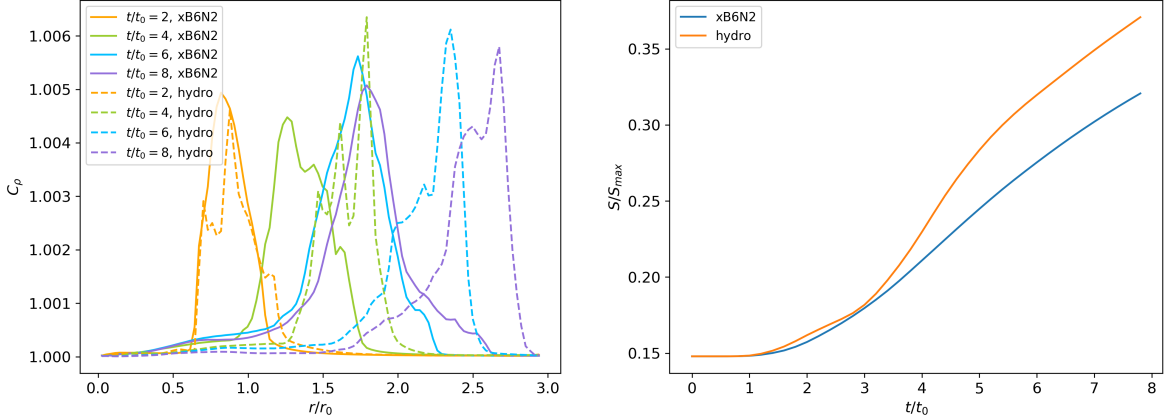


Figure 4.5.: *Left:* Mass-weighted gas clumping factor  $C_p$  averaged over thin radial shells, evaluated at different times for both the fiducial simulation (solid lines) and the hydrodynamical run (dashed lines). *Right:* Volume-integrated dye entropy  $S$  as a function of time, normalised by the maximum entropy  $S_{\text{max}}$  for a fully mixed dye concentration. A fully mixed cluster has  $S/S_{\text{max}} = 1$

#### 4.1.3. Cooling and Heating

While studying the interactions of rising bubbles in a cluster atmosphere, we are also interested in measuring the heating rate of the ICM due to MHD transport processes. As described in section 2.2.3 the cavities provide roughly enough energy to balance the AGN heating rate with the radiative cooling rate of the central gas. The probably self-regulating mechanism of heating and cooling is mitigating cooling flows in CCs and preventing its core collapse. The X-ray cooling rate  $\mathbf{Q}^-$  via bremsstrahlung can be estimated from observed X-ray surface brightness maps and is approximated by  $\mathbf{Q}^- = n^2 \Lambda(T)$ , where  $n$  is the number density and  $\Lambda(T)$  is the cooling function depending on the temperature  $T$ . We have already derived  $\mathbf{Q}^-$  and  $\Lambda(T)$  in equations (2.13) and (2.14), respectively, where we have integrated the emissivity over all frequencies. Normalized to quantities in our ICs, we get a radiative cooling rate (per unit volume) at the cluster center analogous to Kunz et al. (2011) of

$$\mathbf{Q}^- \approx 8 \times 10^{-27} \left( \frac{n}{0.03 \text{ cm}^{-3}} \right)^2 \left( \frac{k_B T}{3.34 \text{ keV}} \right)^{1/2} \text{ erg s}^{-1} \text{ cm}^{-3}. \quad (4.6)$$

In our simulations we need to compute synthetic X-ray images, where we assume the local X-ray emissivity to be proportional to  $\rho^2 T^{1/2}$  and integrate along the line of sight ( $z$ -direction) through the simulation domain (see equation (2.13)). The synthetic X-ray images of our fiducial model  $xB6N2$  are shown in the first column in figure 4.7. At the cluster center, the intensity  $I_X$  is the highest since more bremsstrahlung is emitted due to higher number densities causing more Coulomb collisions at the core. The bubble has very faint emission due to its high temperature and low density. At early times, the displacement of X-ray emission is clearly seen in the uprising cavity and its morphology shows good agreement with observations. However, despite the fact that we use a relatively high viscosity coefficient (about 8 times the Spitzer value, see section 3.1), eddies and perturbations form quite fast at the rim of the bubble, which are actually not observed. And as already discussed, the cavities are even less coherent in the  $y$ - $z$  plane perpendicular to the initial magnetic field lines. Later on as the cavity gets disturbed by KHI and RTI, more cluster gas gets mixed with its interior and more bremsstrahlung is radiated away.

It is unclear how the AGN energy is actually thermalized. Since many heating mechanism in galaxy clusters are proposed (see section 2.2.5), we will only focus on the one arising from pressure anisotropies  $\Delta p = p_{\perp} - p_{\parallel}$ , which enter Braginskii-MHD as an anisotropic viscosity tensor (see section 2.3.5). Kunz et al. (2011) show that pressure anisotropies regulate viscous heating of a weakly collisional magnetized plasma. They infer that these lead to local heating rates which are comparable to the radiative cooling rates in the ICM, if there is sufficient turbulent energy provided, which can be thermalized. In addition, they show that the balance between viscous heating and radiative cooling is thermally stable, whereas it is not with thermal conduction, which arises from an anisotropic heat flux in the Braginskii-MHD equations (which we neglect in this thesis).

We described in section 2.3.5 that the anisotropic pressure arises due to the conservation of the first adiabatic invariant for each particle on time-scales much larger than the ion cyclotron frequency:  $\mu = mv_{\perp}^2/2B = \text{const}$ . So, any change in magnetic field strength must be accompanied by a proportional change in perpendicular pressure, such that  $p_{\perp}/B \sim \text{const}$ . Certainly, a turbulent ICM will induce time-dependent fluctuations in  $B$ , but also an initial quiescent ICM as modelled with  $xB6N2$  will lead to changes in  $B$ , since the rising bubbles are subject to non-linear macro-scale instabilities like KHI and RTI (see section 4.1). Therefore, regions of positive (negative) pressure anisotropy will emerge, corresponding to locally increasing (decreasing) magnetic field strength, which is plotted in the latter columns of figure 4.6. We can see that most of the pressure anisotropy is formed at the rim of the bubble, where the primary vortices are going to be induced. The reason is that  $\Delta p$  is dependent on the rate of strain (see equation 4.9 below) and therefore is associated with turbulent motions. Since the primary vortices inject the majority of turbulent energy into the turbulence cascade, the highest level of  $\Delta p$  are reached at these eddy regions.

Comparing  $\|\mathbf{B}\|$  of the first column of figure 4.6 with the unlimited  $\Delta p$  in column three, contradictorily suggests that the pressure anisotropy is not dependent on magnetic field strength, which can be misleading since  $xB6N2$  is based on an initial  $\beta = 10^6$ , corresponding to  $\|\mathbf{B}\| = 0.1 \mu\text{G}$ . In fact, recalling from equation (2.42) shows that we have a magnetic field strength proportionality as  $\Delta p \propto d/dt(\ln B^3 \rho^{-2}) \propto \dot{B}/B$ . So even if  $B$  is small, the fractional change per unit time,  $\dot{B}/B$ , can be large. Thus in the fiducial run, unlimited  $\Delta p$  is sensitive to changes in field strength, because we see that  $\Delta p \approx 0$  in the trailing region where  $B$  is enhanced, but  $dB/dt \approx 0$  stays roughly constant. If we limit  $\Delta p$  according to equation (2.48), the pressure anisotropy is pinned to a very narrow range of possible values due to the extreme plasma beta. In fact, we find that  $\Delta p \approx 30 \times \Delta p_{\text{lim}}$  in the fourth column of figure 4.6 and we see now, that the limited anisotropic pressure coincides with  $\|\mathbf{B}\|$  instead of  $\dot{B}$ . Regions of positive (negative)  $\Delta p$  correspond to a stronger perpendicular (parallel) thermal pressure component and are color-coded in green (brown).

If the pressure anisotropy  $\Delta p$  becomes comparable to the magnetic energy density  $B^2/8\pi$ , micro-scale instabilities will be triggered (see section 2.3.6), which are not described by Braginskii-MHD and are not resolved in our simulations. In kinetic simulations, these micro-scale instabilities regulate pressure anisotropy such that they sustain marginal stability (Rosin et al., 2011). Hence, in order to model viscous stresses correctly,  $\Delta p$  is limited within thresholds for stability of firehose and mirror instability (see equation (2.48)),

$$-2 < \frac{8\pi\Delta p_{\text{lim}}}{B^2} < 1, \quad (4.7)$$

where we abbreviate  $f p_{\text{lim}} = 8\pi\Delta p_{\text{lim}}/B^2$  for convenience, which is plotted in the second and third columns of figure 4.7. The difference between both columns is that the second one takes

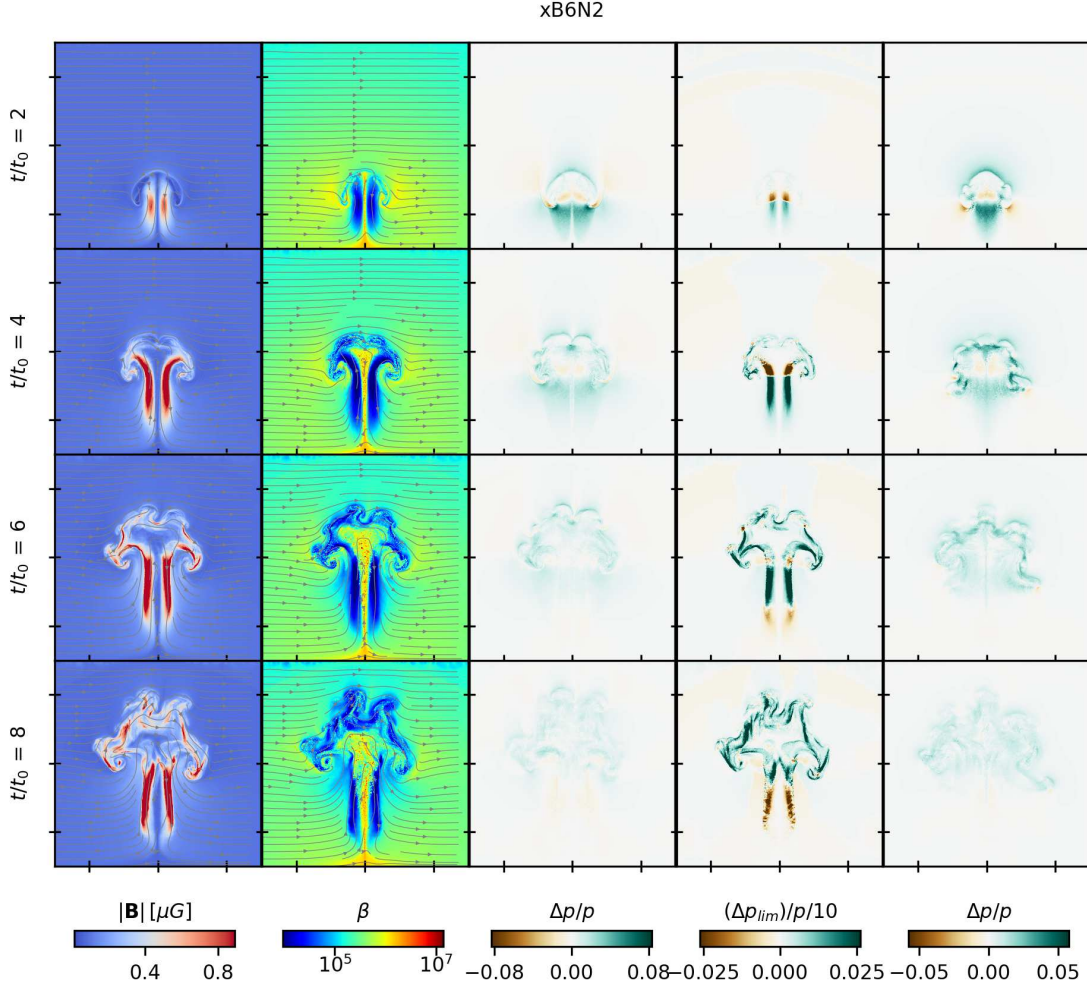


Figure 4.6.: Projected slices of the  $x$ - $y$  midplane parallel to the initially uniform magnetic field lines for our fiducial run  $xB6N2$  showing from left to right the magnetic field strength in micro Gauss, the plasma beta and the unlimited and limited pressure anisotropy. The last column is identical to the third column except that it shows the projected  $y$ - $z$  midplane. Each panel spans a spatial domain corresponding to dimensions  $x \in [-1.5 r_0, 1.5 r_0]$  and  $y \in [0, 3 r_0]$ . The thin projections in  $z$ -direction have width  $dr = 0.066 r_0$  centered at  $z = 0$ .

the unlimited fp and clips them to lie within  $[-2, 1]$ , while the third column limits  $f_{p,\text{lim}}$  before plotting it as a projected slice. The projection represents a small average in  $z$ -direction of almost entirely values being either -2 or 1. Therefore, the third column appears as if  $f_{p,\text{lim}}$  would not be saturated inside the bubble region, but basically it just shows a shifted mean to smaller values compared to column two, where fp ranges up to orders of magnitude of  $\pm 10^3$ . Eitherway, firehose-unstable (mirror-unstable) regions appear as saturated red (violet) patches. We note that the limiters are just artificially implemented in the post-processing for the presented run  $xB6N2$ . The IC itself has been simulated without limiting  $\Delta p$ . Thus, since the patches in the second column are over-saturated, it shows that micro-scale instabilities are excited very quickly. In other words, the patches indicate regions of departure from marginal stability. This is not surprising considering the very low magnetic field strength ( $\beta = 10^6$ ), which shrinks the range of the limits in equation (4.7) significantly.

From equation (2.44) we see that  $\Delta p$  is proportional to the parallel viscosity coefficient and can be interpreted as an anisotropic viscous flux. This enables us to calculate the heating rate due to parallel viscous dissipation of motions. Its derivation follows the arguments presented by Kunz et al. (2011). Starting from the viscosity tensor  $\boldsymbol{\Pi}$ , the viscous heating rate  $\boldsymbol{Q}^+$  is given

by

$$\mathbf{Q}^+ = -\boldsymbol{\Pi} : \nabla \mathbf{v} = \Delta p \left( \mathbf{b} \mathbf{b} : \nabla \mathbf{v} - \frac{1}{3} \nabla \cdot \mathbf{v} \right). \quad (4.8)$$

The term in parentheses is the rate of strain, which is related to the ion-ion collision frequency as

$$\nu_{ii} \Delta p = 2.88 p \left( \mathbf{b} \mathbf{b} : \nabla \mathbf{v} - \frac{1}{3} \nabla \cdot \mathbf{v} \right). \quad (4.9)$$

So, the rate of strain induces pressure anisotropies, which are relaxed on the ion-ion collision time-scale, whenever turbulent motions occur. If we assume that  $\nu_{ii}$  is independent from micro-scale instabilities, equation (4.9) states that the production of pressure anisotropy by macro-scale fluid motions is balanced by isotropization via Coulomb collisions. Using equation (4.9) together with  $\nu_{ii} = 0.96 p / (\nu_{||} \rho)$ , we can rewrite equation (4.8) solely in terms of the pressure anisotropy,

$$\mathbf{Q}^+ = \frac{1}{2.88} \nu_{ii} \frac{(\Delta p)^2}{p} = \frac{(\Delta p)^2}{3 \nu_{||} \rho} = \frac{(\Delta p)^2}{3 \mu}, \quad (4.10)$$

which is always positive (see also Berlok et al. 2019). So, the parallel viscous heating rate (per unit volume) is achieved by assuming that the pressure anisotropy is a source of free energy that is eventually converted into heat by collisions (Kunz et al., 2011).  $\mathbf{Q}^+$  from equation (4.10) is plotted in the fourth and fifth columns of figure 4.7, where the latter is restricted by applying limiters for  $\Delta p$ . The fourth column shows that the unlimited viscous heating rate is the highest in the wake of the bubble at early times when the bubble is about to break apart. There, the rate can go up to  $\mathbf{Q}_{max}^+ = 3.4 Q_0^+$ , where  $Q_0^+ \approx 10^{-25} \text{ erg s}^{-1} \text{ cm}^{-3}$ , which is basically the same value as calculated by Kunz et al. (2011).. Also the rims of the bubble are quite pronounced with average heating rates of  $\mathbf{Q}_{avg}^+ = 0.01 Q_0^+$ . Converting the code units of typical heating rates into physical units yields

$$\mathbf{Q}_{avg}^+ = 0.01 Q_0^+ \approx 1.1 \times 10^{-27} \text{ erg s}^{-1} \text{ cm}^{-3}, \quad (4.11)$$

$$\mathbf{Q}_{max}^+ = 3.4 Q_0^+ \approx 3.5 \times 10^{-25} \text{ erg s}^{-1} \text{ cm}^{-3}. \quad (4.12)$$

The maximum value peaks at about a factor 40 times larger than the radiative cooling rate, which we estimated in equation (4.6), whereas the average value only reaches one tenth of the cooling rate. This means that unlimited Braginskii heating is capable of balancing radiative cooling at some local regions, but it is not throughout the entire cluster core and not continuously over time. As the viscosity coefficient is quite high, viscous stresses can have an effect on the fluid motion and dissipate into thermal energy. At later times the turbulent motions get weaker and concomitant pressure anisotropy, which is quadratically proportional to the heating rate. Hence, the latter decreases accordingly. By looking at the  $y$ - $z$  plane (see fifths column of figure 4.6), a similar picture becomes apparent. Except for the strong heating rate in the wake at  $t/t_0 = 2$ , the values for viscous heating perpendicular to the  $x$ - $y$  plane lie in the same range and are pronounced at the rim of the evolving bubble. The last column of figure 4.7 shows again parallel viscous heating, but with hard-wall limited  $\Delta p$ . The colorbar is scaled in a similar interval as before multiplied by 10. So the limited values are weaker by roughly a factor of 20 overall compared to the unlimited ones. In addition, viscous heating appears at different regions now, because the pressure anisotropy is much more sensitive to changes in the magnetic field strength in the limited case. This can be seen in the upper panel at  $t/t_0 = 2$ , where the very weak magnetic field lines have not been much compressed or stretched yet compared to the initial uniform alignment. Together with equation (4.7), yields that  $\Delta p_{lim}$  becomes much smaller than

$\Delta p$  if  $B^2$  stays very weak. Only when  $B^2$  is locally increasing in compressed regions,  $\Delta p_{\text{lim}}$  becomes noticeably larger. It is useful to compare column five of figure 4.7 with column four of figure 4.6 to infer that both  $Q_{\text{lim}}^+$  and  $\Delta p_{\text{lim}}/p$  coincide with each other. When the rising bubble evolves, the field lines get compressed, the magnetic field gets enhanced and pressure anisotropy induced in these regions is limited by a smaller factor, which in turn leads to viscous heating.

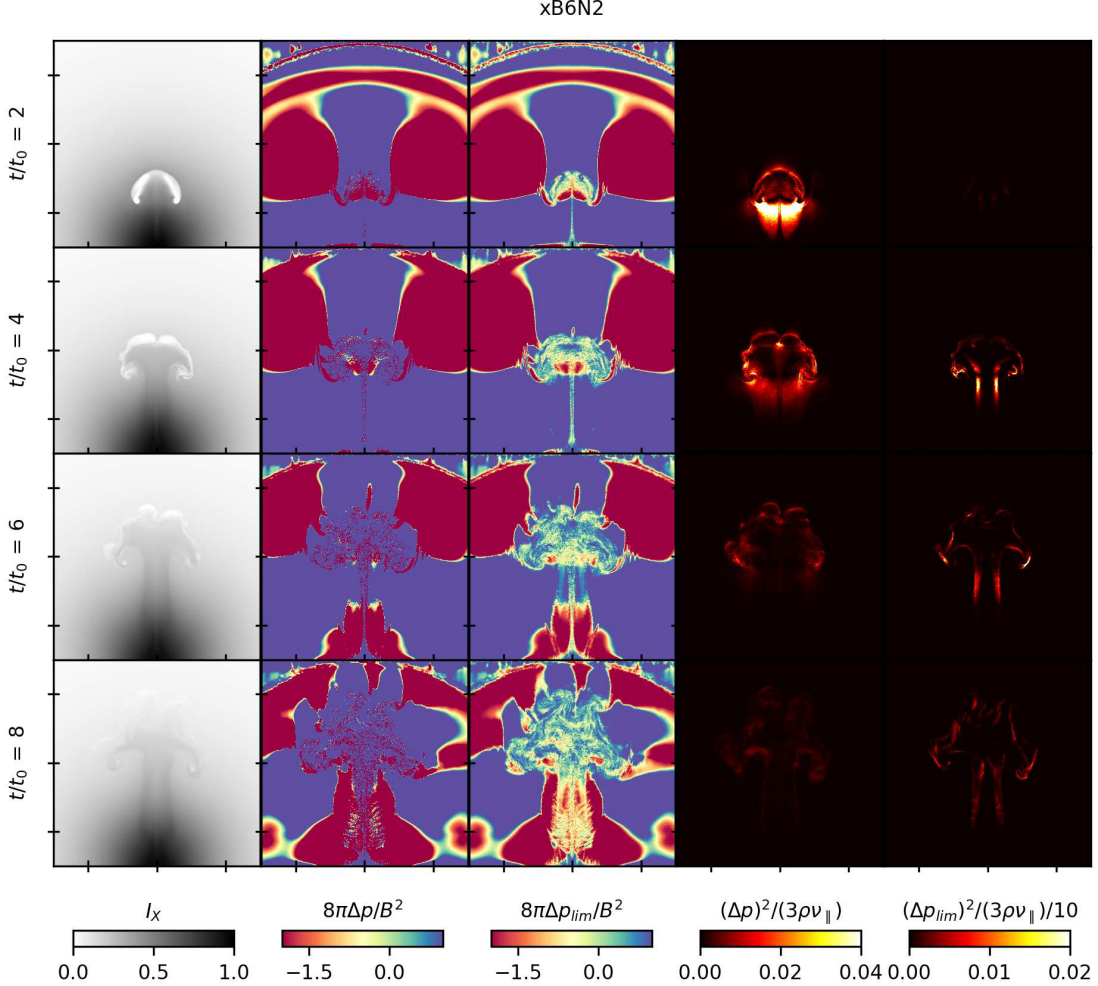


Figure 4.7.: Projected slices of the  $x$ - $y$  midplane parallel to the initially uniform magnetic field lines for our fiducial run  $xB6N2$  showing the synthetic X-ray surface brightness map, the departure from marginal stability for the pressure anisotropy and the parallel viscous heating rate (both each unlimited and limited according to equation (2.49)). Each panel spans a spatial domain corresponding to dimensions  $x \in [-1.5 r_0, 1.5 r_0]$  and  $y \in [0, 3 r_0]$ . The thin projections in  $z$ -direction have width  $dr = 0.066 r_0$  centered at  $z = 0$ .

We show the volume-weighted average heating and cooling rate separately over time in figure 4.8. The left subfigure shows that the cooling rate averaged over the entire spatial domain stays nearly constant at  $Q^- = 10^{-26} \text{ erg s}^{-1} \text{ cm}^{-3}$ , whereas the average unlimited viscous heating rate does not increase above  $Q^+ = 10^{-29} \text{ erg s}^{-1} \text{ cm}^{-3}$ , which puts the latter to the same order of magnitude as the local (non-averaged) limited heating rate  $Q_{\text{lim}}^+$ . Instead of looking at the total cluster average, we plot the average heating rate of the bubbles in the right subfigure, where we define a bubble cell if the passive tracer exceeds  $10^{-3}$ . The cooling rate is now slightly decreasing over time, since the bubble rises upwards into lower dense regions of the cluster core. The average bubble heating rate is only one order of magnitude smaller than cooling at early times, when macro-scale instabilities induce turbulent motions, which produces pressure anisotropy. So, with an initially very weak, non-turbulent magnetic field, parallel viscous heating is not capable of

balancing cooling throughout the bulk of the ICM. It only becomes quite noticeable in the bubble region itself over a short time-scale. The dependence on the bubble location becomes clear by looking at the radial profiles in figure 4.9. The region influenced by bubble motions adiabatically expands over time and dissipates energy across a larger range of radial shells. But as already pointed out, the average viscous heating rate nowhere reaches significantly high values compared to radiative cooling for our fiducial model.

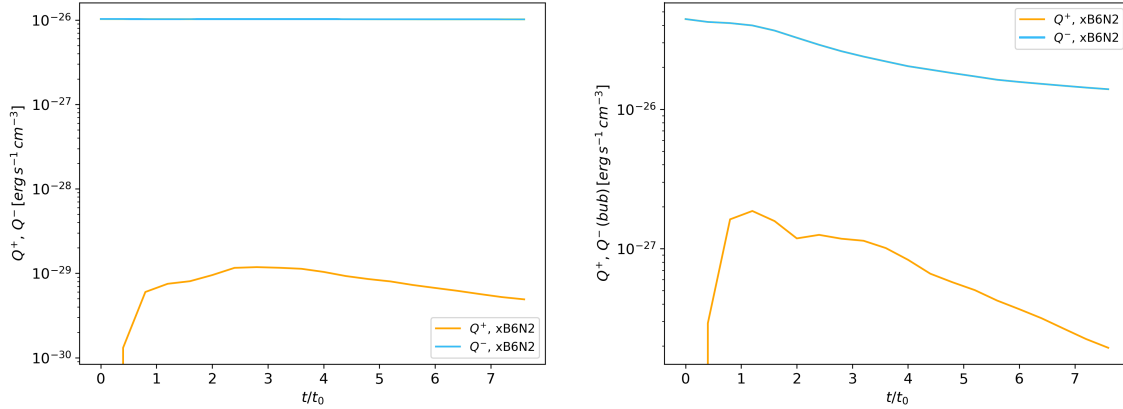


Figure 4.8.: *Left:* Time evolution of the volume-weighted averaged heating and cooling rate in physical units.  
*Right:* Same as left subfigure, but restricted to bubble cells with  $X_{\text{bub}} > 10^{-3}$ .

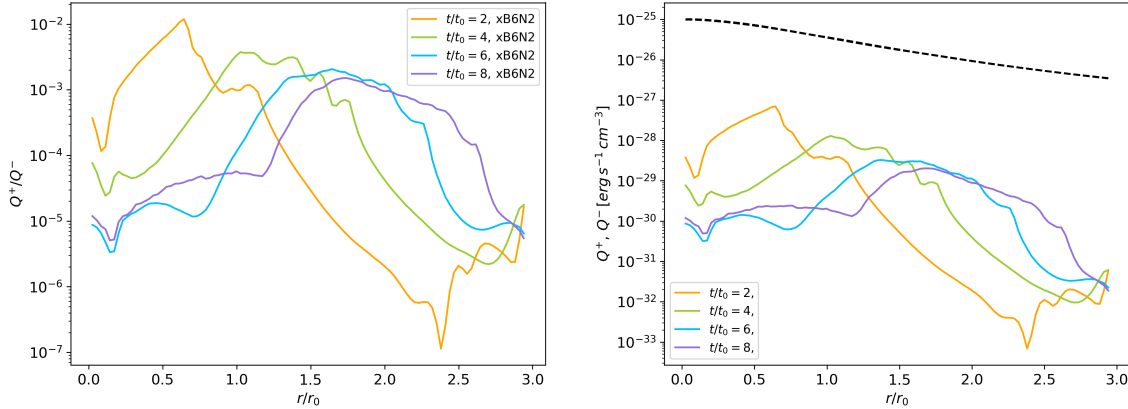


Figure 4.9.: *Left:* Mass-weighted radial profiles of the ratio between heating and cooling rate at specific times.  
*Right:* Mass-weighted radial profiles of the heating rate (solid lines) and cooling rate (dashed line) in physical units at specific times. The cooling rate stays nearly constant at all times.

## 4.2. Uniform $\mathbf{B}$ , $\beta = 10^6$

So far, we have described and analysed the global evolution of our fiducial run  $xB6N2$ , which models the ICM as an extremely weakly magnetized plasma. We also inferred viscous heating rates from the fluid motions having a Reynolds number of approximately 50, while the pressure anisotropy was not limited. In section 4.2.1 we analyse the results when on the one hand the viscosity coefficient is reduced by a factor of ten as in model  $xB6N3$  (yielding  $\text{Re} = 500$ ), and on the other hand when the viscosity is not reduced specifically, but the pressure anisotropy is limited as in model  $xB6N2lim$  according to the thresholds given by equation (2.48). In section 4.2.2 we analyse how an isotropic Braginskii viscosity affects the evolution of an buoyantly rising bubble. The initial orientation and the strength of the magnetic field is kept unchanged in all of these three cases.

### 4.2.1. Parameter Study - Reducing and Limiting $\nu_{\parallel}$

For run  $xB6N3$ , the reduced viscosity coefficient implies an increasing Reynolds number to  $\text{Re} = 500$ . As pointed out in section 3.1, this results in a modelled ICM, which is just about 20 percent as viscous as we have estimated for the Spitzer value. So, it should be much less efficient in suppressing KHIs or viscous heating than our fiducial run. We expect a similar outcome for  $xB6N2lim$ , if the limiters are applied to pressure anisotropy since the interval where  $\Delta p$  is not pinned to marginal stability becomes very narrow for a very high plasma beta (see section 4.1.3). We can see its evolution in morphology in figure 4.10, where the passive tracer mass fraction is plotted for several different Braginskii runs and compared to the hydrodynamical run in the first column. The rising bubbles show no striking differences between runs *hydro*,  $xB6N2lim$  and  $xB6N3$ . This implies that firstly, the micro-scale instabilities are triggered so fast in  $xB6N2lim$  that actually very little pressure anisotropy can be produced, which induces viscous stresses. Secondly, the unlimited viscous stresses in  $xB6N3$  are not strong enough to suppress RTI effectively and the bubble material gets mixed with the ambient medium on time-scales comparable to the *hydro* run. Therefore, in order to resemble the coherent cavities observed in X-ray surface brightness maps, the viscosity coefficient must be at least close to the Spitzer value. Furthermore it is interesting to note, if we compare the wake of  $xB6N2lim$  with  $xB6N2$ , we identify just a mono-line of vertically stripped gas in the limited run, whereas in the unlimited case there are clearly two projected stripes of gas visible. These stripes also indicate enhanced magnetic field strengths due to stretched/compressed field lines. From this point of view,  $xB6N3$  seems to be an intermediate case, where the duality is slightly apparent. Also the bubble front of  $xB6N2$  at  $t/t_0 = 2$  is wider compared to  $xB6N2lim$ , where the morphology has more like a bullet shape.

How well each model mixes its bubble material with the ambient ICM can be seen in figure 4.11, where we plot the volume-integrated passive tracer entropy  $S$  as a function of time (see section 4.1.2). The two models being discussed in this section have levels of entropy close to the *hydro* run, implying nearly unsuppressed mixing rates. Thereby, the limited run with  $\nu_{\parallel} = 10^{-2}$  is slightly less viscous than the unlimited run with  $\nu_{\parallel} = 10^{-3}$ . Hence, confirming our qualitative analysis. The violet line representing the isotropic model differs significantly and will be discussed in section 4.2.2. We find the following ordering

$$S_{\text{hydro}} > S_{\text{lim}} > S_{\text{Brag}} > S_{\text{iso}}, \quad (4.13)$$

precisely as expected.

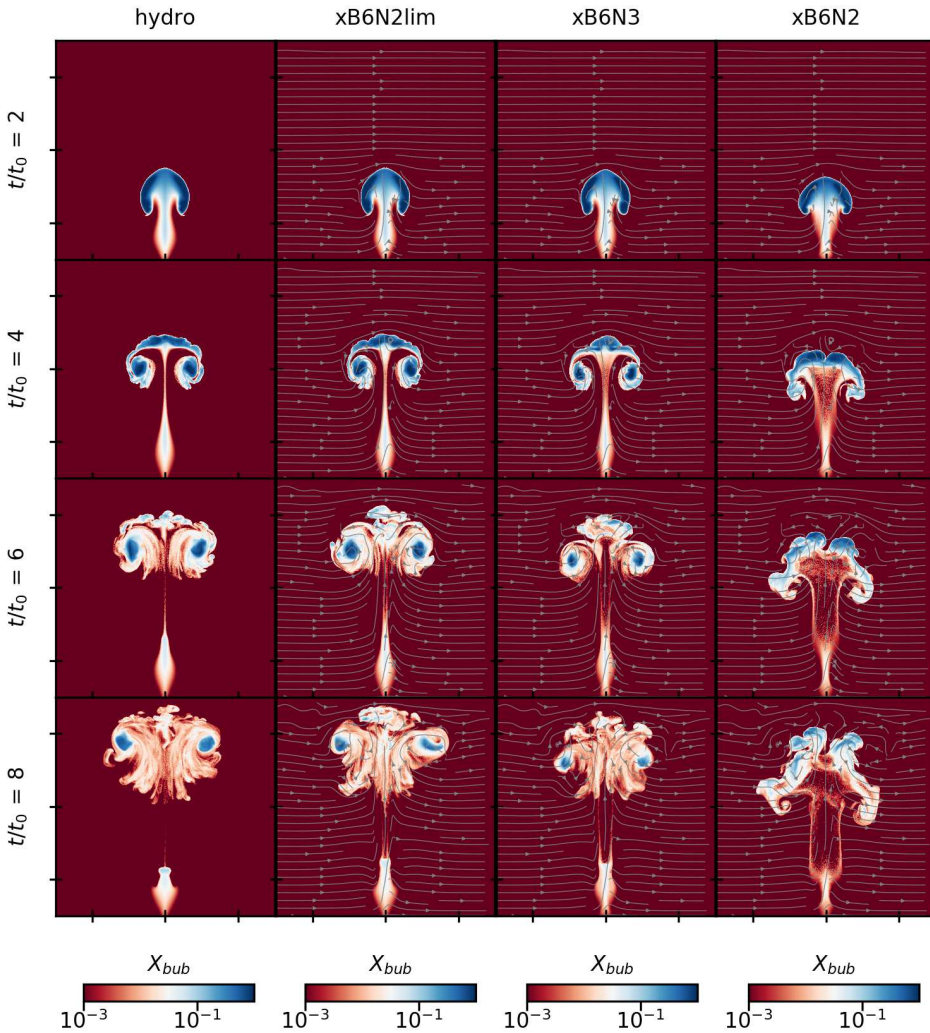


Figure 4.10.: Projected slices of the  $x$ - $y$  midplane parallel to the initially uniform magnetic field lines showing the tracer mass fraction  $X_{\text{bub}}$  for several models including from left to right *hydro*, *xB6N2lim*, *xB6N3* and the fiducial run *xB6N2*. Each panel spans a spatial domain corresponding to dimensions  $x \in [-1.5 r_0, 1.5 r_0]$  and  $y \in [0, 3 r_0]$ . The thin projections in  $z$ -direction have width  $dr = 0.066 r_0$  centered at  $z = 0$ .

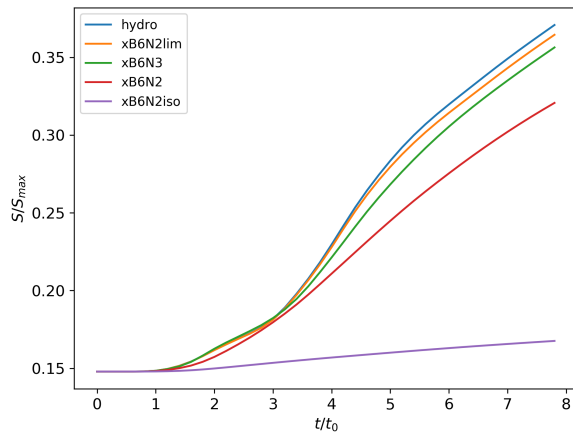


Figure 4.11.: Volume-integrated dye entropy  $S$  as a function of time, normalised by the maximum entropy  $S_{\text{max}}$  for a fully mixed dye concentration. A fully mixed cluster has  $S/S_{\text{max}} = 1$ . It shows the mixing efficiency of the bubble material for the given runs or in other words how viscous the evolving bubbles become.

In the first three columns of figure 4.12 we show the evolution over time of the limited pressure anisotropy, the limited range of marginal stability and the limited viscous heating rate for  $xB6N2lim$ . By directly comparing the "physically" limited  $\Delta p_{\text{lim}}$  (first column) with the "artificially" limited one of  $xB6N2$  in the fourth column of figure 4.6, we can infer that the bubble region produces ten times more pressure anisotropy in the former case.

The parallel viscous heating rates for simulation  $xB6N2lim$  (third column of figure 4.12) are fairly of the same order of magnitude than the unlimited rates  $Q^+$  for  $xB6N2$  shown in the fourth column of figure 4.7. In addition, we can infer that the "physically" limited  $\Delta p$  in  $xB6N2lim$  locally induces about one order of magnitude more viscous heating than the "artificially" limited  $\Delta p$  in  $xB6N2$ . So, after considering both "physically" and "artificially" mixing and heating rates, it becomes clear that it is not sufficient to simply mimic limited pressure anisotropy by clipping its values during the post-processing after the simulation has been already run.

The last three columns of figure 4.12 show the unlimited results of  $\Delta p$ ,  $f_p$  and  $Q^+$  for run  $xB6N3$ . The unlimited viscous heating rates are smaller than about a factor of ten compared to  $xB6N2$ . This might be quite surprising as  $Q^+$  is proportional to  $1/\nu_{\parallel}$ , naively indicating that lowering the viscosity coefficient would result in an increased heating rate. But since  $Q^+ \propto (\Delta p)^2$ , the production of the latter must be considered more powerful. And indeed, by comparing  $\Delta p$  of  $xB6N3$  with  $xB6N2$  (third column of figure 4.6) we infer that  $\Delta p(xB6N2) \approx 10 \times \Delta p(xB6N3)$ , resulting in a ten times smaller heating rate for  $xB6N3$ , considering that  $\nu_{\parallel}(xB6N2) = 10 \times \nu_{\parallel}(xB6N3)$ .

Nonetheless,  $xB6N2lim$  and  $xB6N3$  show different bubble regions where viscous heating emerges. The reason is the same as we have already discussed in section 4.1.3 and occurs because of the extremely high plasma beta. If  $\Delta p$  is limited, it becomes sensitive to changes in magnetic field strength. Where the field lines get compressed, pressure anisotropy is produced which enters viscous heating quadratically. If it is unlimited, production of  $\Delta p$  is dominated by the rate of strain of turbulent motions. We do not present radial profiles of the  $Q^+/Q^-$  ratio or the alike, because the graphs are quite similar to the ones plotted for  $xB6N2$ , except that the heating rates are even weaker.

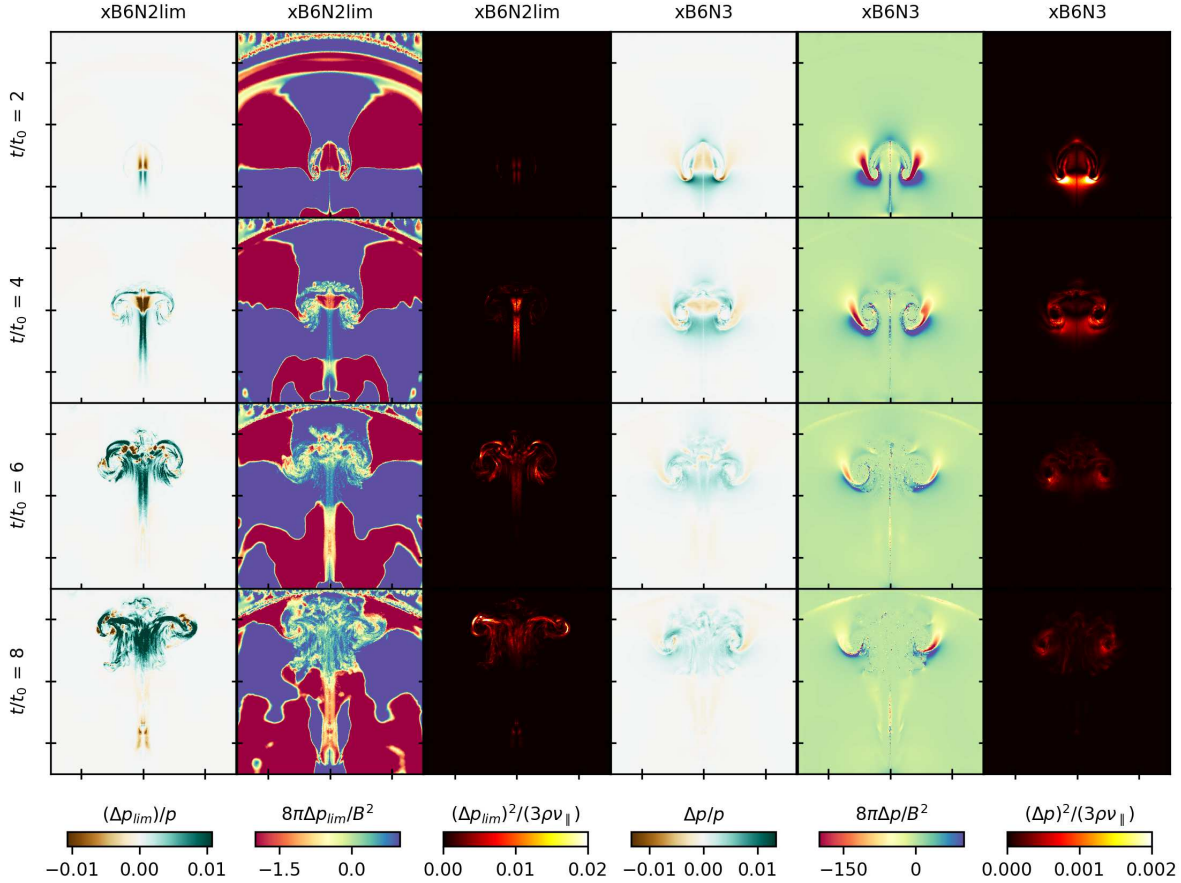


Figure 4.12.: Projected slices of the  $x$ - $y$  midplane parallel to the initially uniform magnetic field lines showing from left to right the limited pressure anisotropy, departure from marginal stability and viscous heating for  $xB6N2lim$ , and the unlimited  $\Delta p$ ,  $f_p$  and  $Q^+$  for run  $xB6N3$ . Each panel spans a spatial domain corresponding to dimensions  $x \in [-1.5 r_0, 1.5 r_0]$  and  $y \in [0, 3 r_0]$ . The thin projections in  $z$ -direction have width  $dr = 0.066 r_0$  centered at  $z = 0$ .

### 4.2.2. Isotropic Viscosity

Instead of modelling buoyantly rising bubbles affected by anisotropic viscosities within Braginskii-MHD, we take the isotropic viscosity tensor as introduced in equation (2.47) and discuss in this section how the bubbles evolve if the viscous stresses are not dependent on the direction of the magnetic field lines. We can see the isotropic result with  $\text{Re} = 50$  in figure 4.13, which we can compare with the isotropic runs "5" from Reynolds et al. (2005) and "H2" from Dong and Stone (2009). As our tracer mass fraction and synthetic X-ray image show, Navier-Stokes viscosity suppresses KHIs and RTIs and thus prevents mixing quite efficiently. Directly comparing  $xB6N2iso$  with  $xB6N2$  reveals a drastically altered bubble evolution, where the bubble remains intact throughout the simulation time. Especially the bubble front stays coherent and undisturbed from macro-scale instabilities. However, a mushroom-like trailing region is forming over time, which is in good agreement with the findings by Reynolds et al. (2005); Dong and Stone (2009). The synthetic X-ray surface brightness map also matches with observations of X-ray cavities in real galaxy clusters (see figure 2.2 for Perseus-A). The isotropic mixing rate is plotted as the violet line in figure 4.11 indicating that the entropy of the passive tracer reaches only 17% of its maximum entropy level for a fully mixed ICM at  $t/t_0 = 8$ . This value is about one half of the run  $xB6N2$  with anisotropic viscosity at the end of the simulation. Hence, the latter is not as efficient as an isotropic viscosity at suppressing KHI, because the effective anisotropic viscosity is dependent on the field line direction and therefore its damping effect on motions is reduced.

From the vorticity map, showing the absolute curl of velocity  $\|(\nabla \times v)\|$  in units of  $1/t_0$ , we can infer that the bubble interior is relatively quiescent and not driven by turbulent motions. Although the highest levels of vorticity are induced at the rim of the bubble as it rises upwards through the cluster atmosphere, these are not sufficiently high to trigger KHI or RTI. In addition, pressure support might play a role in form of draping of magnetic field lines at the bubble front, where magnetic pressure is enhanced by nearly a factor of 100. The isotropic morphology and vorticity generation resembles the findings by Dursi and Pfrommer (2008) performing 3D simulations of overdense bubbles rising in an initially uniformly magnetized medium.

We note that a run with an isotropic Navier-Stokes viscosity of  $\nu_{\text{iso}} = 10^{-3}$  ( $\text{Re} = 500$ ) does not show a coherent bubble surface. Note that this level of viscosity is roughly  $\sim 80\% \nu_{\text{sp}}$  the Spitzer value (see section 3.1), which is quite interesting considering the following study. Using deep *Chandra* observations of the Coma cluster, Zhuravleva et al. (2019) find from analysing density fluctuations down to the viscous dissipation scale that the effective isotropic viscosity in the bulk ICM is suppressed by a factor of  $\sim 100$  by comparing with hydrodynamic simulations based solely on Coulomb collision rates. This implies that the cluster gas appears to be much more turbulent with a large effective Reynolds number and that their results fit best with hydrodynamic simulations using level of isotropic viscosity with  $\nu_{\text{iso}} \sim 0.01 \nu_{\text{sp}}$  of the Spitzer value. In figure 4.13, our isotropic viscosity coefficient is roughly 8 times as viscous as the Spitzer value. If we lower  $\nu_{\text{iso}}$  by one order of magnitude ( $\sim 80\% \nu_{\text{sp}}$ ), the evolution of our bubble shows emerging KHIs resulting in disrupted bubble interfaces. We suppose that if we would have run another simulation with  $\nu_{\text{iso}} \sim 1\% \nu_{\text{sp}}$  (consistent with Zhuravleva et al. 2019), the bubble would have been shredded much sooner not resembling the morphology of observed (ghost) cavities. Therefore, isotropic dissipation of momentum is not very likely the correct physics for suppressing fluid macro-instabilities. Zhuravleva et al. (2019) conclude that the suppressed effective viscosity can be explained by preferring non-hydrodynamic models including anisotropic transport and plasma micro-instabilities in order to account for the enhanced collision rates.

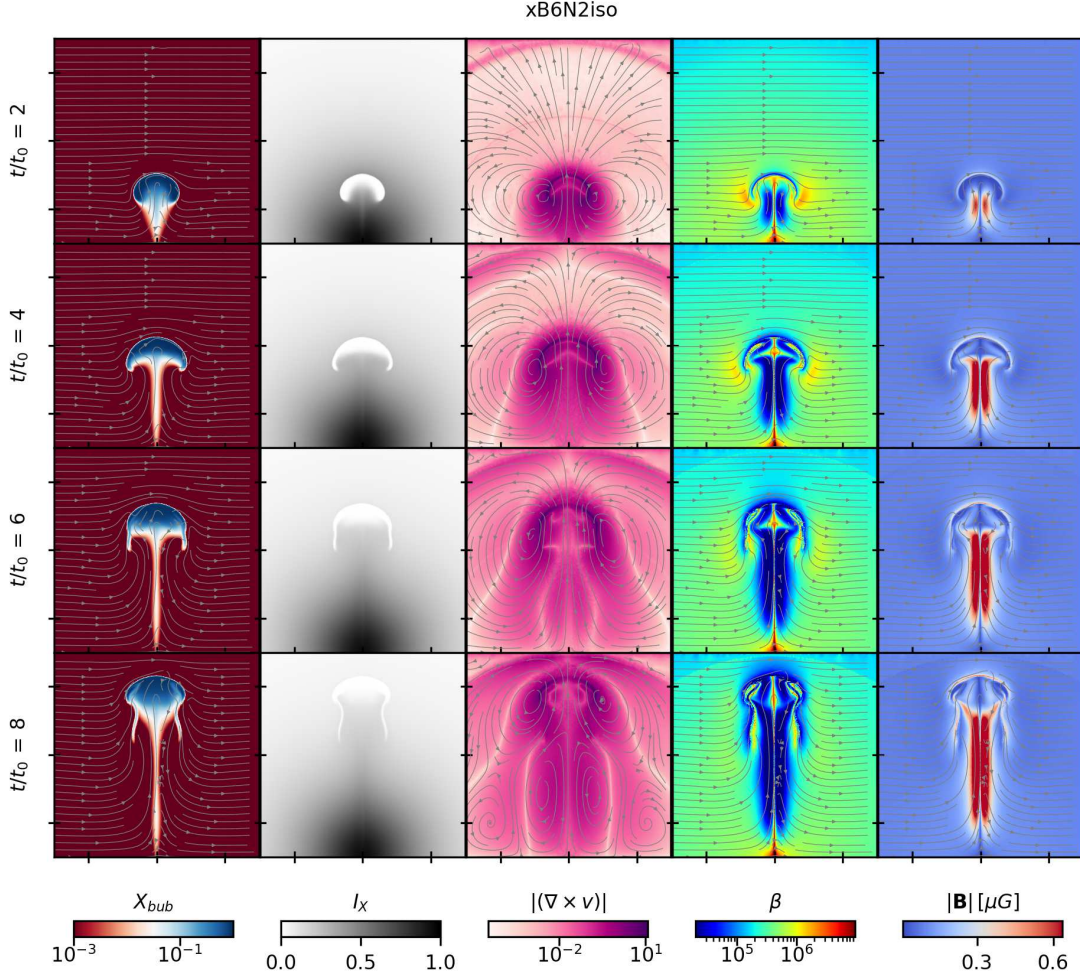


Figure 4.13.: Projected slices of the  $x$ - $y$  midplane parallel to the initially uniform magnetic field lines showing from left to right the tracer mass fraction, the line-of-sight integrated X-ray emissivity, the absolute vorticity in units of  $t_0$ , the plasma beta and the magnetic field strength in micro Gauss for run  $xB6N2iso$ . The first, fourth and fifth columns show streamlines of the magnetic vector field, while the third column shows the vector field of the velocity. Each panel spans a spatial domain corresponding to dimensions  $x \in [-1.5 r_0, 1.5 r_0]$  and  $y \in [0, 3 r_0]$ . The thin projections in  $z$ -direction have width  $dr = 0.066 r_0$  centered at  $z = 0$ .

### 4.3. Uniform $\mathbf{B}$ , $\beta = 100$

In this section we present model  $xB2N2lim$ , where we keep the initially uniformly magnetized medium, but increase the magnetic field strength from  $\|\mathbf{B}\| = 0.1 \mu\text{G}$  to  $\|\mathbf{B}\| = 9 \mu\text{G}$  by setting the plasma beta to  $\beta = 100$ . Additionally, our modelled B-field becomes radially dependent on the density such that  $B(\mathbf{r}) = \rho(\mathbf{r})^{1/2}$ , which is in accordance with the findings by Bonafede et al. (2010) for fitting an isothermal cluster profile (see section 2.3.3). Figure 4.14 shows qualitatively the mixing efficiency and the evolution in morphology of the rising bubble of run  $xB2N2lim$  by plotting the tracer mass fraction  $X_{\text{bub}}$  and the line-of-sight integrated X-ray intensity  $I_X = \rho^2 T^{1/2}$ . Odd columns show the projected  $x$ - $y$  midplane, while even columns show the  $y$ - $z$  midplane perpendicular to the uniformly aligned field lines. A striking difference between the two planes becomes immediately apparent. The plasma beta is now four orders of magnitude greater than in the discussed models before, hence making the anisotropic effect of magnetic tension pronounced. The magnetic field is so strong that the macro-scale fluid motions become two-dimensionalized with respect to the magnetic field direction. In the  $x$ - $y$  midplane parallel to the field, RTIs are suppressed by high magnetic tensions and viscous stresses. Conversely, in the  $y$ - $z$  midplane perpendicular to the field, neither Braginskii viscosity nor magnetic tension is very efficient in suppressing RTI and we see elongated fingers emerging from the rising bubble.

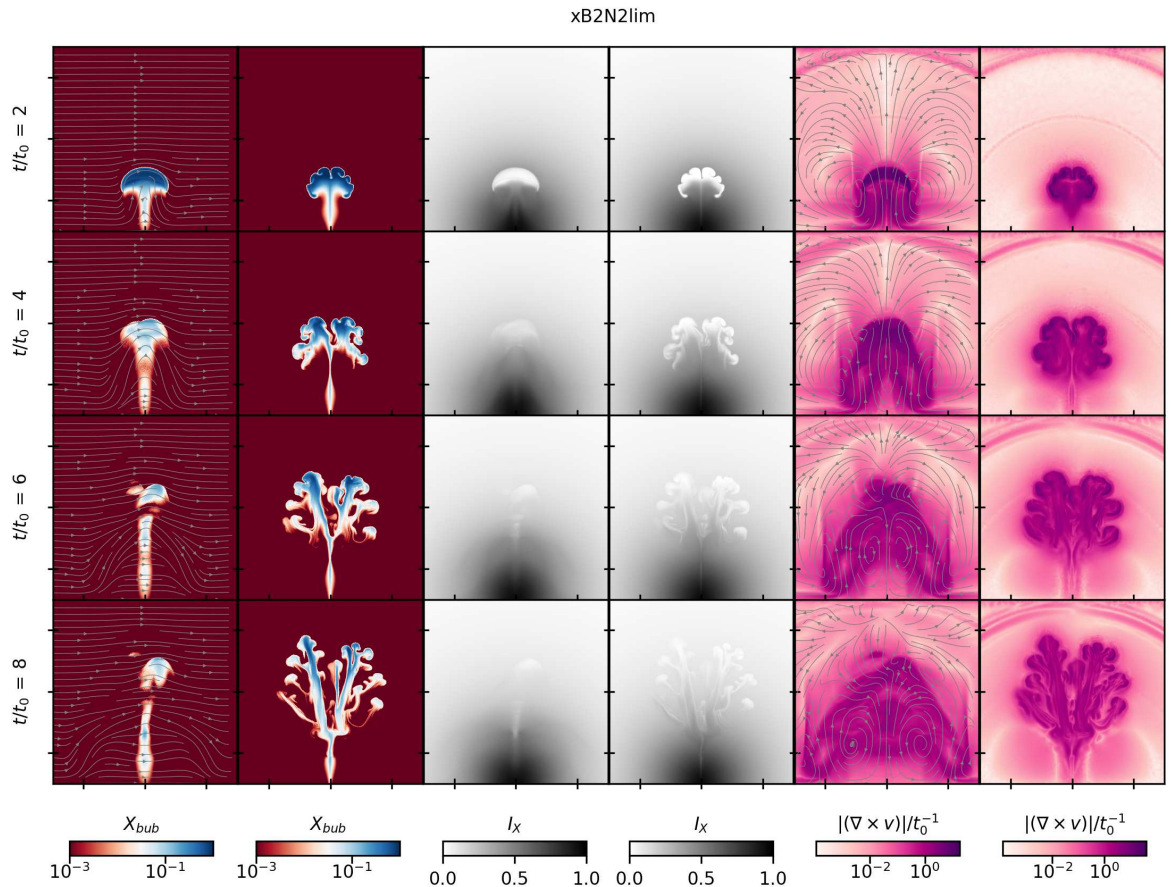


Figure 4.14.: Projected slices of  $xB2N2lim$  alternating between the  $x$ - $y$  midplane parallel to the initially uniform magnetic field lines and the  $y$ - $z$  midplane perpendicular to it. The first two columns show the tracer mass fraction  $X_{\text{bub}}$  with streamlines of the magnetic vector field, the middle columns the synthetic X-ray surface brightness map and the last two columns the absolute vorticity with streamlines of the velocity vector field. Each panel spans a spatial domain corresponding to dimensions  $[-1.5 r_0, 1.5 r_0]$  and  $[0, 3 r_0]$ . The thin projections have width  $dr = 0.066 r_0$ .

The occurrence of these fingers might be supported by the fact that the initial bubble region

has not been magnetically isolated from the ambient uniformly aligned field lines. As described in section 2.3.1 the plasma fluid is tied to the field lines. So as the bubble buoyantly rises, it drags the field lines with it, which inhibits the bubble material to escape due to the relatively high magnetic tension effects. Together with the fast-growing RTI, where perturbations are quite unsuppressed in the perpendicular direction, the elongated fingers become apparent as a physical consequence.

The magnetic field strength and the limited pressure anisotropy can be seen for both midplanes in figure 4.15. We find that the production of  $\Delta p_{\text{lim}}$  reaches roughly the same order of magnitude as the unlimited  $\Delta p$  in run  $xB6N2$  (see figure 4.6). Therefore, as long as the magnetic pressure of the ICM is sufficiently large compared to the thermal pressure, the pressure anisotropy clipped to lie within kinetically motivated thresholds does not shrink noticeably and simultaneously mixing is suppressed by magnetic tension. This is in contrast to a very weakly magnetized ICM where  $\Delta p_{\text{lim}}$  induced viscous stresses alone are not capable of keeping the bubble material unmixed (see section 4.2.1). We have ran both  $xB2N2$  and  $xB2N2lim$ , but focus only on the latter in this section, because both look very similar in terms of morphological evolution and their derived quantities. They do not differ much, because both  $\Delta p$  and  $\Delta p_{\text{lim}}$  vastly never trigger the firehose or mirror micro-instabilities, which can be seen in the latter two columns of figure 4.15 for  $xB2N2lim$ . Except for the  $y-z$  midplane at  $t/t_0 = 2$  the thresholds for marginal stability are almost nowhere reached. Note that we plot  $f_p$  here without projection to ensure not to dilute the panels with a mean computed from averaging positive and negative values. If the micro-scale instabilities are never triggered, then implies that the viscous stresses can be entirely described by Braginskii-MHD and are not inhibited at some spatial regions. In this case we do not expect to see a physically motivated disagreeing outcome by comparing  $xB2N2$  and  $xB2N2lim$ .

Therefore, we focus on analysing  $\Delta p_{\text{lim}}$  of run  $xB2N2lim$  in the middle two columns of figure 4.15. The bubble interior itself and its trailing region are dominated by the parallel pressure component (color-coded in brown), whereas the rim of the bubble is dominated by the pressure component perpendicular to the local magnetic field lines (color-coded in dark-green). The regions where  $\Delta p_{\text{lim}}$  is induced coincide quite well with regions of higher levels of vorticity, which confirms that pressure anisotropy is produced where fluid motions generate a non-negligible amount of rate of strain, which is not dependent on the strength of the magnetic field (see equation 2.44). Whether  $\Delta p_{\text{lim}}$  is positive or negative depends partially on the local direction of the field line  $\mathbf{b}$  and also on the gradient and divergence of velocity. So one can tell from  $\Delta p \propto d/dt(\ln B^3) \propto \mathbf{b}\mathbf{b} : \nabla\mathbf{v}\nabla \cdot \mathbf{v}$  whether the magnetic field is increasing in time or decreasing. It is quite interesting to note that both projected midplanes do not significantly differ in the amount of pressure anisotropy they produce.

In order to clarify that it physically does not matter for the bubble evolution whether the anisotropic pressure is limited or not, we plot the viscous heating rates for the simulations  $xB2N2$  and  $xB2N2lim$  in figure 4.16. It becomes evident that not only are the buoyantly rising bubbles evolving quite similar, but also dissipate nearly the same amount of heat, which is comparable to the unlimited viscous heating rate of  $xB6N2$  with  $\beta = 10^6$  in figure 4.7. Hence, the rate of viscous heat  $Q^+$  seems to be not dependent on the initial plasma beta used for modelling the ICM of an isothermal cluster core, if one ignores the kinetic limiters. On the other hand, it does depend significantly if the limiters are considered.

If the pressure anisotropy is driven to be at marginal stability of the micro-scale instabilities according to equation (2.49), we can rewrite the expression for viscous heating (4.10) together

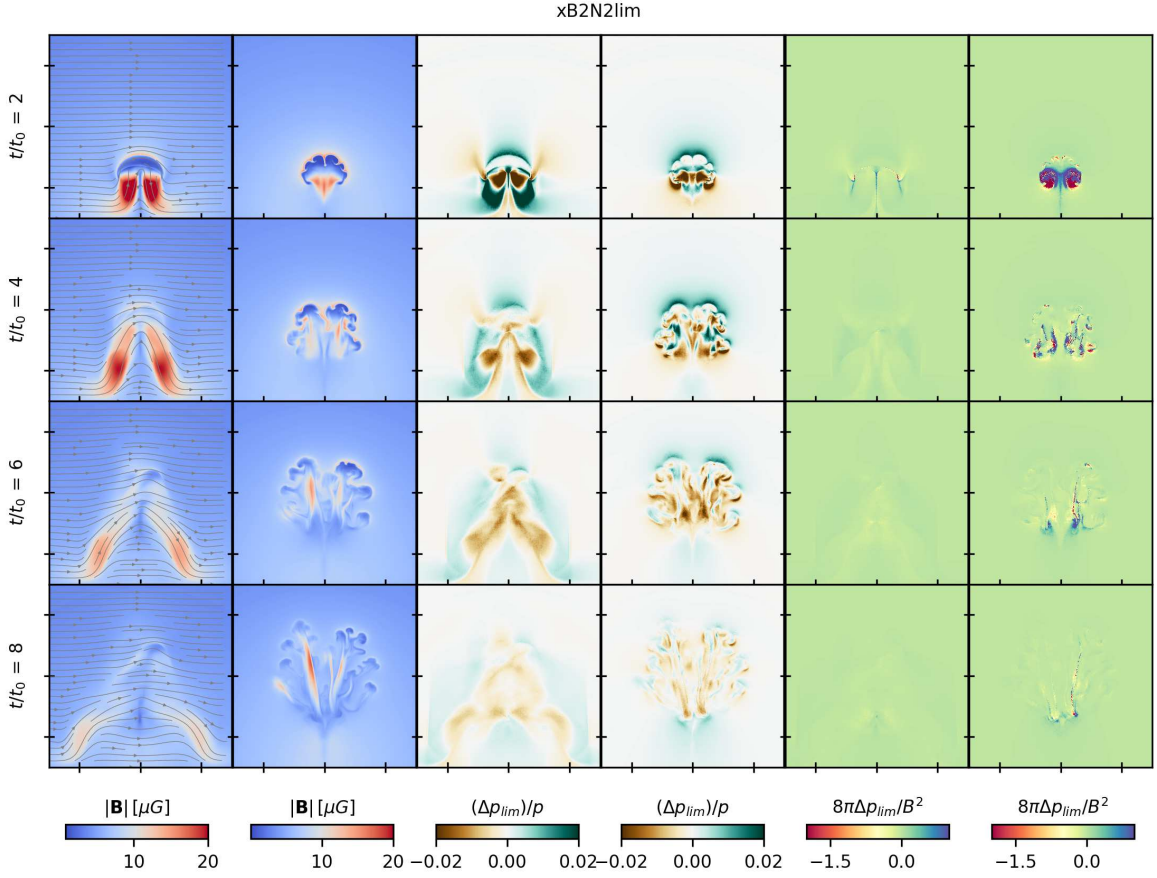


Figure 4.15.: Projected slices of  $xB2N2lim$  alternating between the  $x$ - $y$  midplane parallel to the initially uniform magnetic field lines and the  $y$ - $z$  midplane perpendicular to it. The first two columns are showing the magnetic field strength in micro Gauss  $\|\mathbf{B}\|$ , the middle columns the limited pressure anisotropy  $\Delta p_{lim}$  and the last two columns departure from marginal stability  $fp$ . Each panel spans a spatial domain corresponding to dimensions  $[-1.5 r_0, 1.5 r_0]$  and  $[0, 3 r_0]$ . Except for the latter two, the thin projections have width  $dr = 0.066 r_0$ .

with the Spitzer viscosity of equation (2.30) to

$$Q_{lim}^+ = 7.7 \times 10^{-27} \xi^2 \left( \frac{\|\mathbf{B}\|}{10 \mu G} \right)^4 \left( \frac{k_B T}{3.34 \text{ keV}} \right)^{-5/2} \text{ erg cm}^{-3} \text{ s}^{-1}, \quad (4.14)$$

where  $\xi$  is either -2 ( $p_{\parallel}$  dominated firehose unstable) or 1 ( $p_{\perp}$  dominated mirror unstable). In fact, equation (4.14) assumes that  $\Delta p_{lim}$  reaches marginal stability in the entire spatial domain such that there is no spatial region where the microinstabilities are not triggered. Note the strong dependence on magnetic field strength,  $Q^+ \propto B^4$ , which becomes immediately clear here compared to equation (4.10). We can infer that locally  $Q_{lim}^+ \approx Q^-$  by comparing the limited heating rate (4.14) with the cooling rate (4.6) if normalised to the same ICs. This is only to some extent consistent with the results found by Kunz et al. (2011). In fact our estimate (per unit volume) in equation (4.14) is equal to the one stated by Kunz et al. (2011), but they claim that both viscous heating and radiative cooling should approximately balance themselves at all radii inside the cluster core due to turbulent dissipation,  $Q_{lim}^+(r) \simeq Q^-(r)$ . This is not what we infer from plotting the mass-weighted radial profiles for the ratio  $Q^+/Q^-$  at different times of the bubble evolution for runs  $xB2N2$  and  $xB2N2lim$  in the right subfigure of 4.17. Instead we see that the ratio only barely reaches  $10^{-2}$  inside the bubble region at early times. At later times the ratio shrinks continuously down to several  $10^{-4}$ , which can be also seen in the left subfigure of 4.17, where we plot both rates separately restricted to cells classified as bubble material as

a function of time. Outside the bubble region viscous heating rates are negligibly small and are not even close to balance radiative cooling. This seems to be in contrast with Kunz et al. (2011). However they assume a turbulent ICM with a constant source of driving the turbulent motions, where the production of pressure anisotropy triggers the micro-scale instabilities in order to sustain marginal stability within limits already derived in equation (4.7). These limits are  $fp = [-2, 1]$ , where  $fp = 8\pi\Delta p/B^2$ . In our simulation setup, the bubble does not drive such strong motions in a volume filling fashion.

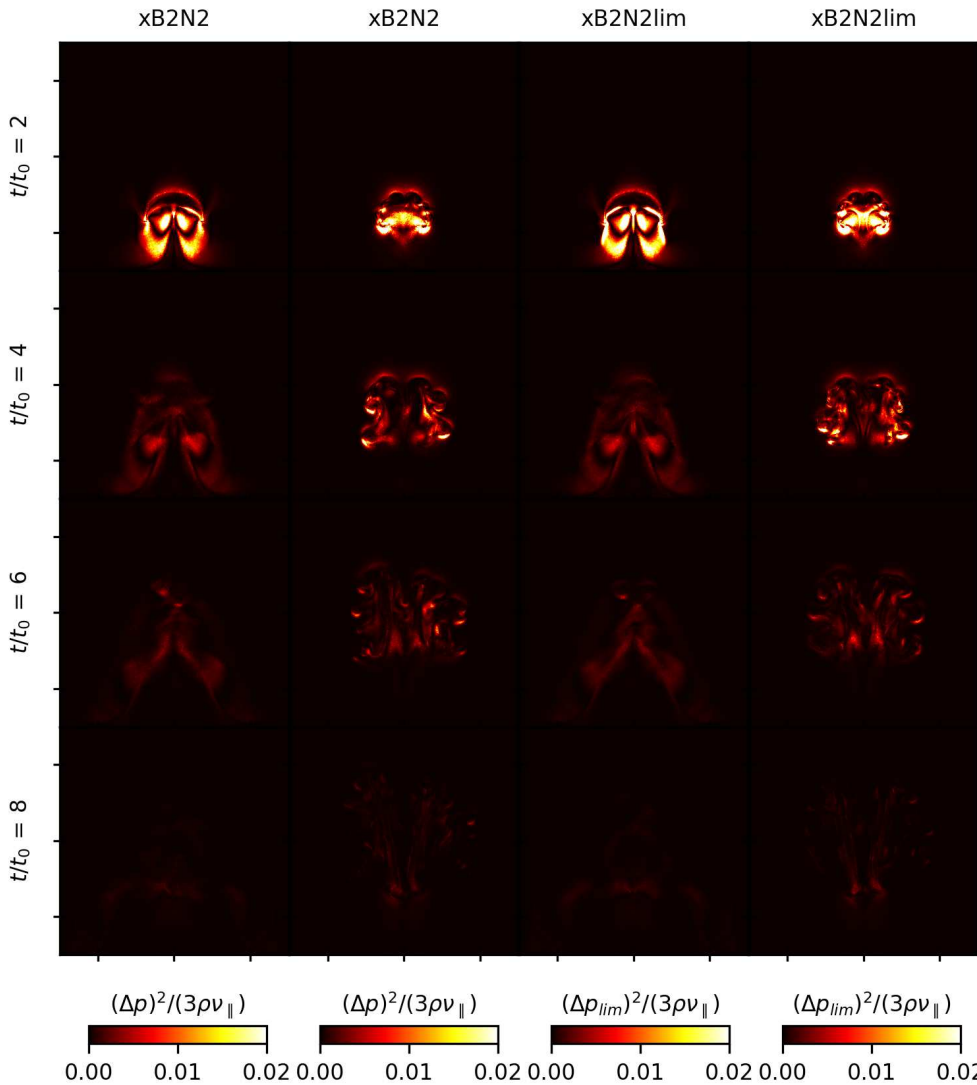


Figure 4.16.: Projected slices alternating between the  $x$ - $y$  midplane parallel to the initially uniform magnetic field lines and the  $y$ - $z$  midplane perpendicular to it. The first two columns show the unlimited parallel viscous heating of  $xB2N2$  and the last two columns the limited parallel viscous heating of  $xB2N2lim$ . Each panel spans a spatial domain corresponding to dimensions  $[-1.5 r_0, 1.5 r_0]$  and  $[0, 3 r_0]$ . The thin projections have width  $dr = 0.066 r_0$ .

We try to reproduce their assumption by restricting  $fp$  for each cell in our computational domain to be exactly either -2 or 1. This allows us to quantify the viscous heating rate as a theoretically maximum averaged over the entire cluster core, which is plotted in the left subfigure of 4.18 as a function of time. We infer that indeed the average  $Q^+$  becomes comparable to the radiative cooling rate as the ratio between both stays almost constantly at one at all radii (see right subfigure of 4.18). Therefore, we conclude that the estimated balance by Kunz et al. (2011) is satisfied with our ICs considering the given assumptions. So on condition that a

cluster atmosphere has a steady source of driving turbulence, parallel viscous heating in terms of a specific heating mechanism among several others can be potentially high enough to not be neglected in order to solve the cooling flow problem. In our simulation setup, however, the AGN bubble on its own is not a sufficient source. Other sources of driving, e.g. mergers, could increase the heating rate (see discussion in chapter 5).

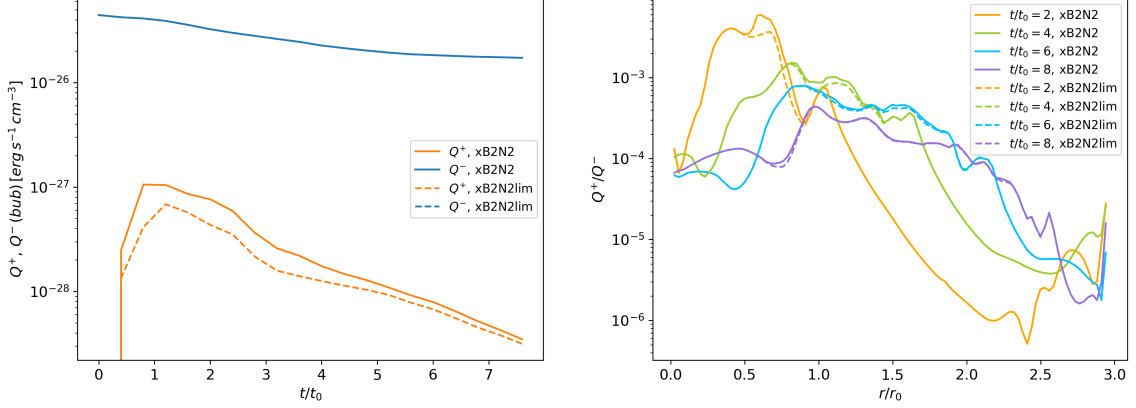


Figure 4.17.: *Left:* Time evolution of the volume-weighted averaged heating and cooling rate in physical units, restricted to bubble cells with  $X_{\text{bub}} > 10^{-3}$ . Solid lines show the rates for the unlimited run  $\text{x}B2N2$  and dashed lines for the limited run  $\text{x}B2N2\text{lim}$ . *Right:* Mass-weighted radial profiles of the ratio between heating and cooling rate for both models at specific times.

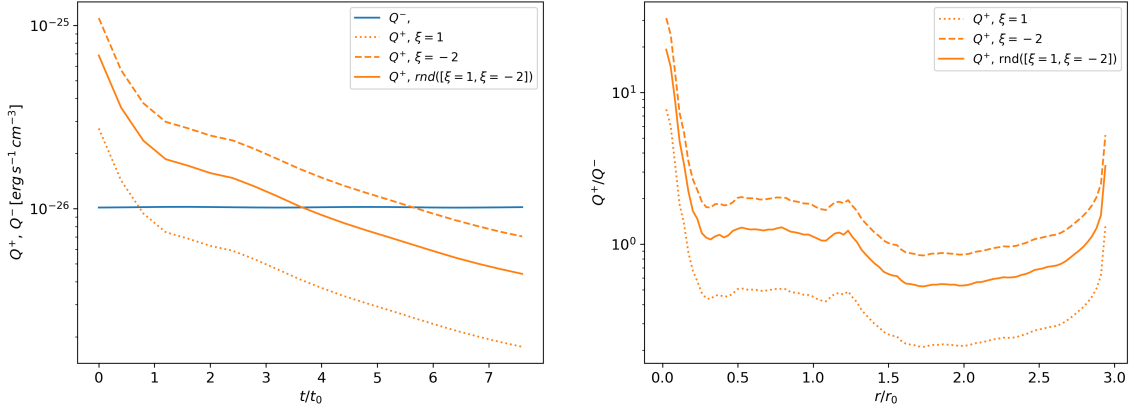


Figure 4.18.: *Left:* Volume-averaged viscous heating rate and radiative cooling rate for the entire cluster domain as if the pressure anisotropy for each cell has a value exactly such that the lower (upper) threshold for reaching marginal stability by triggering the firehose (mirror) micro-instability is taken, plotted as the dashed (dotted) line. The orange solid line represents the case as if for each cell  $\text{fp} = 8\pi\Delta p_{\text{lim}}/B^2$  is randomly given either the lower or the upper limit value. *Right:* Similar to left subfigure but now plotted as mass-weighted radial profiles at time  $t/t_0 = 4$ .

#### 4.4. Turbulent $\mathbf{B}$ , $\beta = 100$

After discussing in detail the different models with an uniformly magnetized ICM in previous sections, we analyse the model  $tB2N2lim$  in this section, where the magnetic field is initialized according to a Kolmogorov power spectrum at an injection scale slightly larger than the bubble size (the characteristic length scale). The magnetic field configuration is described in section 3.1.1. Its result is a turbulent ICM with a roughly constant plasma beta and internal energy throughout the spatial domain with a field strength dependence on density as  $B \propto \rho^{1/2}$  and magnetically isolated bubbles. These properties make the turbulent magnetic field model  $tB2N2lim$  our most sophisticated model presented in this thesis.

In section 4.3 we showed that simulations with  $\beta = 100$  display roughly the same behaviour regardless of whether pressure anisotropic limiters are used or not. Thus, we choose to solely show the physically more relevant simulation  $tB2N2lim$  where  $\Delta p_{\text{lim}}$  is limited. The bubble evolution is plotted in figure 4.19 for both the projected  $x$ - $y$  and the  $y$ - $z$  midplane. In comparison to the uniform magnetic field alignment with  $\beta = 100$  discussed previously in section 4.3, we do not see elongated Rayleigh-Taylor fingers or mushroom-like vortex-rings emerging in the turbulent ICM. We do see different patterns in how the bubble gets mixed with the ambient gas between the two presented midplanes. One spatial direction seems to be more efficient in suppressing macro-scale instabilities than the other. We assume that this observation is simply due to the Gaussian random distribution of the initial magnetic field in  $k$ -space.

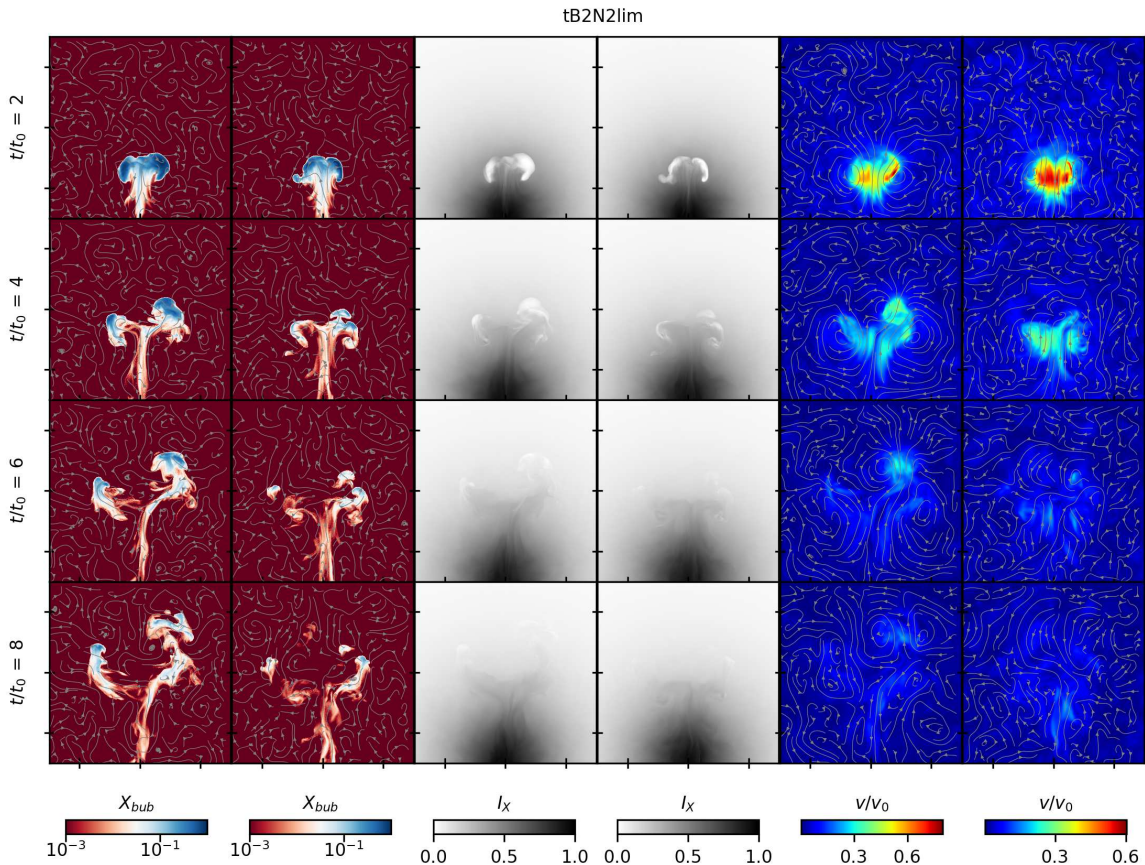


Figure 4.19.: Projected slices of  $tB2N2lim$  alternating between the  $x$ - $y$  midplane and the  $y$ - $z$  midplane. The first two columns are showing the tracer mass fraction  $X_{\text{bub}}$  with superimposed streamlines of the magnetic vector field, the middle two columns the synthetic X-ray surface brightness maps  $\rho T^{1/2}$  and the last two columns show the velocity field  $v/v_0$ . Each panel spans a spatial domain corresponding to dimensions  $[-1.5 r_0, 1.5 r_0]$  and  $[0, 3 r_0]$ . The thin projections have width  $dr = 0.066 r_0$ .

Nonetheless, the overall mixing and dissipation rates are relatively high. Neither the magnetic tension effects nor the viscous stresses are capable of suppressing RTI and KHI on longer time-scales, not even in the  $x$ - $y$  plane where the bubble interior stays most coherent over time. The turbulent fluid motions become strongly anisotropic due to the Lorentz force and the turbulent eddies dissolve in the turbulent cascade and interact between different modes (see section 2.3.3).

In figure 4.20 we compare several quantities, which are all linked together physically as we already pointed out by discussing them in previous sections. The pressure anisotropy is proportional to the rate of strain (see equation 2.44), which in turn depends on turbulent motions represented by the curl of the velocity vector - the vorticity.  $\Delta p$  also increases with an enhanced magnetic field (see equation 2.42), induced by compressed field lines and represented by the magnetic field strength and the plasma beta. Furthermore, the production of anisotropic pressure is an indicator for how much viscous heating dissipates into the ICM. By looking at the fourth column in figure 4.20, we do see the same levels of  $\Delta p_{\text{lim}}$  in the rising bubble and its wake as in  $xB2N2lim$ . Additionally, also the ambient gas becomes anisotropic to relevant amounts due to the turbulent motions. The ambient pressure anisotropy is mainly negative indicating that on the one hand the magnetic field lines get rather stretched than compressed or on the other hand the injected turbulent velocities fade out and their gradients decrease. At locally confined regions  $\Delta p_{\text{lim}}$  triggers the firehose (mirror) instability as can be seen in the fifth column as saturated red (violet) small patches. However, the majority of the plasma lies within  $f_p = 8\pi\Delta p_{\text{lim}}/B^2$ , where no clipping is needed in order to keep the MHD description of the fluid applicable. Note that  $f_p$  is not shown in projection to avoid plotting a smoothed out average value.

The viscous heating rate lies in the same order of magnitude as in the other simulations with a non-turbulent field. A noticeable difference in run  $tB2N2lim$  is the fact that at early times not only the bubble interior itself reaches relevant heating rates, but also the ambient ICM produces enough  $\Delta p_{\text{lim}}$  to induce sufficiently high levels of  $Q^+$ . Since there is no driver for constantly injecting turbulence into our cluster atmosphere, the initial turbulent motions start to dissipate their kinetic energy and the ambient gas becomes quiescent again at later times as in the uniformly magnetized models. Here, by initial we mean that the turbulent velocities are entirely introduced by the Lorentz force due to the tangled magnetic field, because they are set to zero at  $t/t_0 = 0$ . The additional source of heat from the turbulent ICM however, is still not capable of balancing the radiative cooling rate as can be seen in figure 4.21. We note that we account for viscous heating from the ambient turbulent motions in the left subfigure by using the vorticity map as a new threshold for averaging  $Q^+$  instead of the tracer mass fraction. Even so,  $Q_{\text{turb}}^+$  is still about a factor of ten smaller than  $Q^-$  at early times and drops down to even a hundredth of the latter later on, which is basically repeating the same graph as for  $Q_{\text{bub}}^+$  of run  $xB2N2lim$  in figure 4.17.

The mass-weighted radial profiles in the right subfigure of 4.21 reveal a similar result. Although the limited turbulent run shows slightly higher heating-to-cooling ratios compared to the unlimited turbulent simulation  $tB2N2$ , the overall picture shows that  $Q^+/Q^-$  decreases continuously with time. As in  $xB2N2lim$  the ratio barely reaches values of  $10^{-2}$  at the beginning of the simulation, where the initially injected turbulent velocities contribute most of the ICMs pressure anisotropy to support viscous heating. This becomes apparent as the orange line stays relatively constant at  $Q^+/Q^- \approx 2 \times 10^{-3}$  even at the outer radii, whereas for  $xB2N2lim$  in figure 4.17 viscous heating establishes itself only inside the bubble region and drops down to  $Q^+/Q^- \approx 2 \times 10^{-6}$  at the outer radii for the same time  $t/t_0 = 2$ . At later times the turbulent motions get dissipated and in turn no new turbulent energy sources are introduced (except for RTI and KHI induced turbulent eddies). Hence, the overall  $Q^+/Q^-$  ratio decreases down to  $\sim 10^{-3}$  for the bubble region and even lower at the ambient radii. This shows that turbulent

viscous heating as computed in our isothermal cluster model is still too low in terms of being a neutralising agent for radiative cooling throughout scales of space and time. Nonetheless, as we pointed out with figure 4.18, viscous heating has the potential in doing so, if there would be constant driving of turbulence in the cluster core such that pressure anisotropy would steadily be lying within levels of marginal stability.

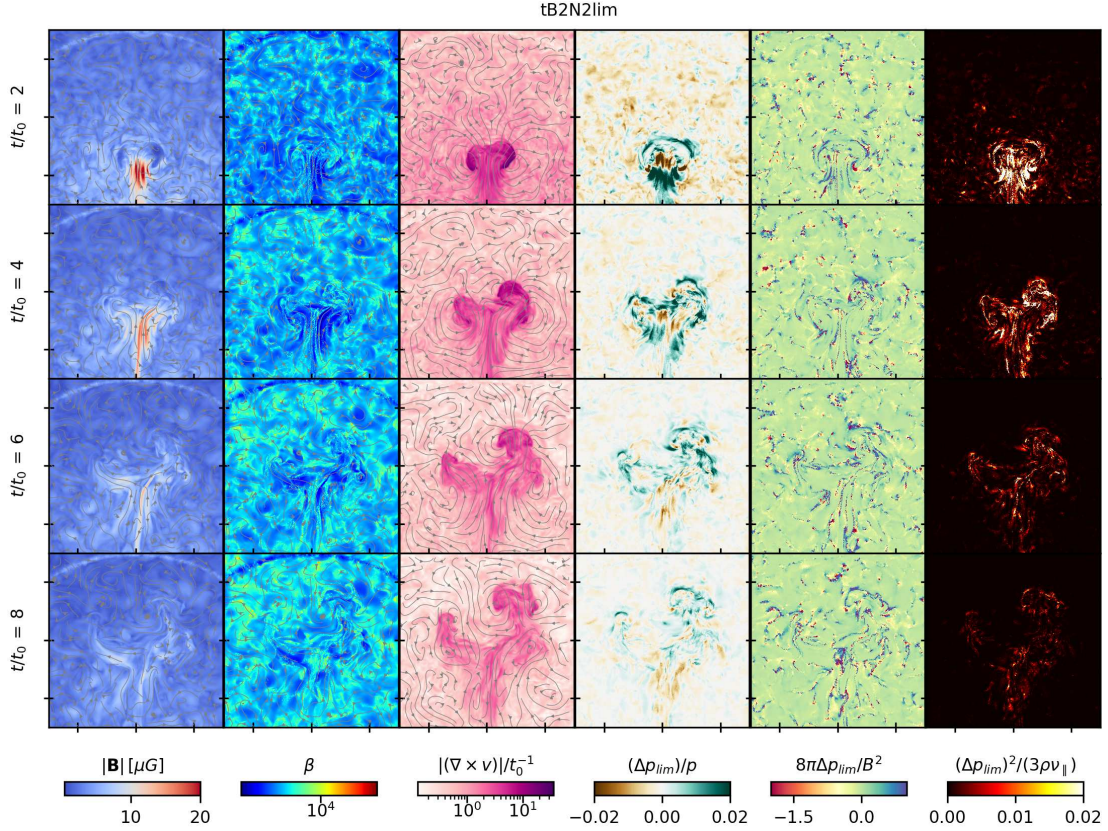


Figure 4.20.: Projected slices of the  $x$ - $y$  midplane showing from left to right the magnetic field strength in micro Gauss, the plasma beta, the absolute vorticity, the limited pressure anisotropy, the departure from marginal stability  $f_p$  and the viscous heating rate. The first and second columns show streamlines of the magnetic vector field, while the third column shows the vector field of the velocity. Each panel spans a spatial domain corresponding to dimensions  $x \in [-1.5 r_0, 1.5 r_0]$  and  $y \in [0, 3 r_0]$ . The thin projections (except for  $f_p$ ) in  $z$ -direction have width  $dr = 0.066 r_0$  centered at  $z = 0$ .

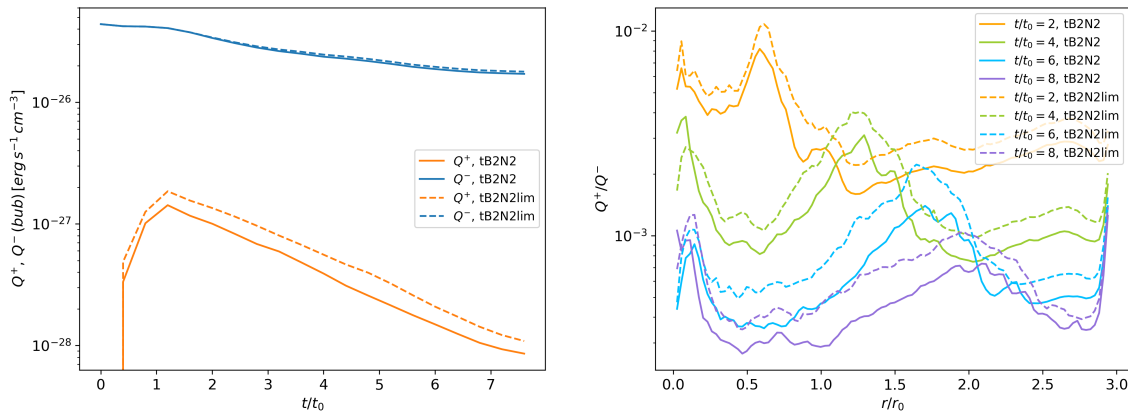


Figure 4.21.: *Left:* Time evolution of the volume-weighted averaged heating and cooling rate in physical units, restricted to grid cells with vorticity levels exceeding  $\|(\nabla \times v)\| > 5/t_0$ . Solid lines show the rates for the unlimited run  $tB2N2$  and dashed lines for the limited run  $tB2N2lim$ . *Right:* Mass-weighted radial profiles of the ratio between heating and cooling rate for both models at specific times.

## 4.5. Sanity Check and Convergence Test

As a last part of our analysis, we check on the one hand that our ICs show numerical convergence and on the other hand if they maintain hydrostatic equilibrium over time. First, in order to test for hydrostatic equilibrium, we perform a simulation without bubbles and check that the velocities within the unperturbed ICM approaching zero. Without using the special boundaries for our ICs, which we have described in section 3.2.3, the cluster atmosphere does not stand still and instead fluid velocities emerge moving towards the outer edges of the spatial domain. This can be explained since we clip the density distribution at  $3r/r_0$ , where the analytical beta-profile has not become asymptotically close to zero. Hence, the cluster cannot maintain hydrostatic equilibrium in this case. One could clip the density distribution at arbitrarily large  $r/r_0$  to ensure that  $\rho \approx 0$  approaches zero at the outer radii, but this would expand the spatial domain to unreasonable large dimensions in terms of total number of cells to keep the resolution constant. Therefore, we introduced in-/outflow boundaries, which results in very low absolute velocities throughout the ICM such that we can confirm hydrostatic equilibrium.

Next, we calculate the percentage change in total energy and in total mass within the boundaries of our domain. In figure 4.22 we show the results for our simulation *hB6N2* with the fiducial resolution. The total energy is the sum of kinetic, thermal, magnetic and gravitational energy (for notation see section 4.1.1). We find that by the end of the simulation the loss both in total energy and total mass is less than one percent of the initial value. Despite that the total energy is not perfectly conserved, we conclude that our simulations are still feasible and that our outer boundary conditions work fine. In addition, we have checked that the HD run and the ideal MHD run (i.e. without viscosity) with a very weak magnetic field ( $\beta = 10^6$ ) are nearly indistinguishable in terms of morphology and show the same characteristics during their evolution.

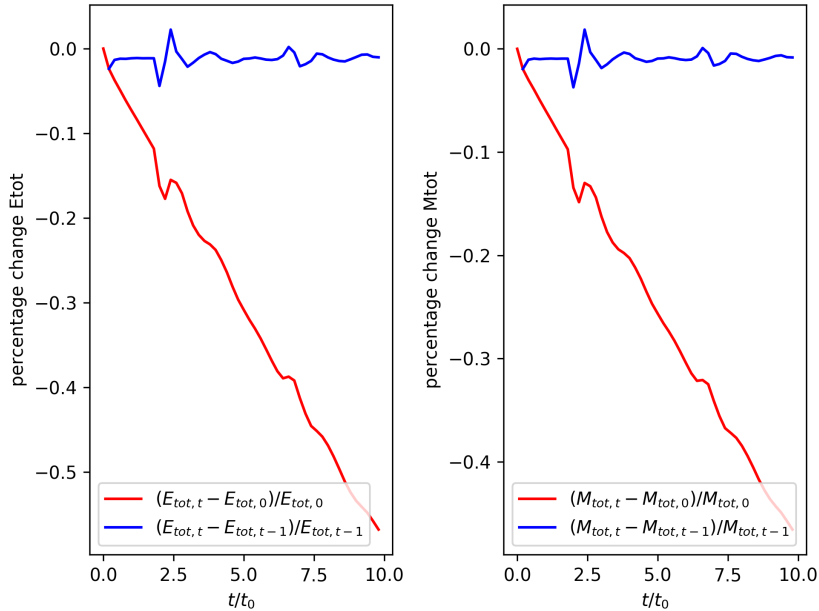


Figure 4.22.: *Left:* The red curve shows the percentage change in total energy taken over the simulation time, where  $E_{\text{tot}} = E_{\text{kin}} + E_{\text{th}} + E_B + E_g$ . The blue curve shows the fractional percentage change in total energy for each timestep. *Right:* Similar to the left subfigure, here plotted with total mass, where  $M_{\text{tot}} = \int_V m \, dV$ .

Next, we perform a resolution study to confirm that our fiducial resolution is numerically converged. This is important to show that the physical dynamics of the fluid motions are

resolved (to a certain degree). We use the same approach as done by Dong and Stone (2009) since our model setup is quite similar (see section 3.1). We take the hydrodynamic runs at four different resolutions, where each resolution gets increased by multiplying the number of cells by a factor of  $\sim 3$ . Note that the simulation labeled "Higher" is identical to our fiducial one. We show the convergence for the kinetic energy as a function of time and for  $\langle v_y \rangle_M$  as a function of radius  $r$  in figure 4.23.  $\langle v_y \rangle_M$  is the absolute value of the vertical component of the velocity, mass-averaged over a spherical shell at each radii. As Dong and Stone (2009) state,  $\langle v_y \rangle$  should be indicating convergence quite well since it is a proxy for the buoyant motion of the bubbles. This does not become very clear by looking at figure 4.23. The two lowest and the two highest resolutions seem to coincide with each other, but looking at all of them there is no asymptotic convergence towards higher resolutions identifiable. The difference becomes even more noticeable for the kinetic energies and hints at whether we resolve KHI or not. For both of the higher resolutions, length scales of the perturbations of the KHI seem to be resolved, which induce turbulent motions at the bubble interface and thus higher levels of kinetic energy. In addition, those fluid cells get dissolved and mixed faster with the ambient gas, which slows down the rising bubble as it expands, damping  $\langle v_y \rangle$  a little bit. In fact, we do want the KHI to be resolved in order to be able to infer how effectively Braginskii viscosity suppresses the macro-scale instabilities. Therefore, we focus on analysing the fiducial run as it is very close to our highest resolution simulation both quantitatively in terms of  $E_{\text{kin}}$  and  $\langle v_y \rangle$  and qualitatively in terms of morphology. We expect, if we would have gone even one step higher in resolution, it would still resemble the curves of our highest resolution. We note that increasing the resolution even further would not be easily achievable, because the Braginskii timestep is proportional to the cell size squared,  $\Delta t_{\text{Brag}} \propto (\Delta x)^2$  (see section 2.4.1).

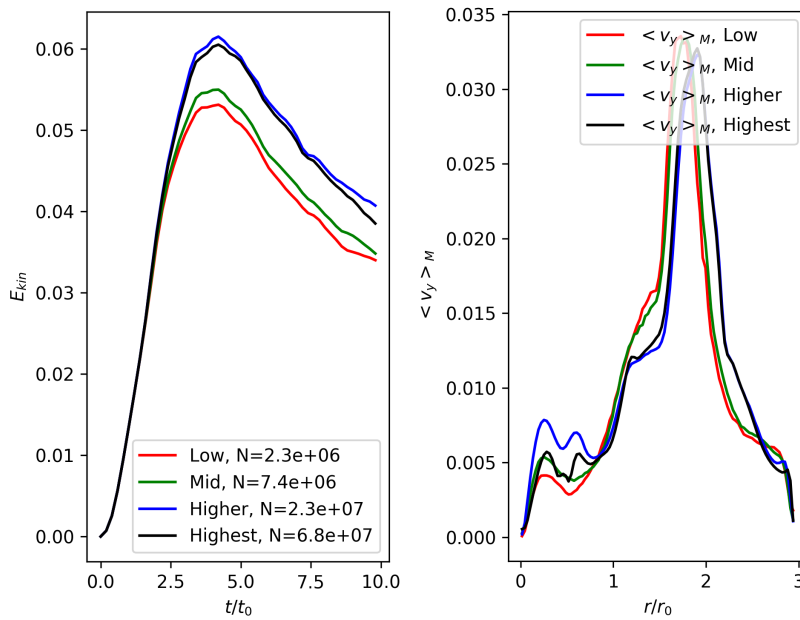


Figure 4.23.: *Left:* Convergence test plotting the kinetic energy for each of our hydrodynamic resolutions. The resolution labeled "Higher" is identical to our fiducial resolution. We set the next higher resolution by increasing the number of cells  $N$  by a factor of  $\sim 3$ . *Right:* Convergence test plotting the vertical component of the velocity, mass averaged over a spherical shell as a function of radius of that shell at  $t/t_0 = 5$ .

We also compare the bubble morphology for each of our four resolutions in figure 4.24. The passive scalar mass fraction is plotted to focus on differences due to mixing. The global evolution

has been already analysed in section 4.1, which we will not repeat here. We confirm that the first two and the last two resolutions show similar morphologies to each other. A main difference between both groups is that the rise velocity of the bubble front scales with resolution. This correlation has been found for jet-inflated bubbles as well (Bourne and Sijacki, 2017; Weinberger et al., 2017). The bubble front travels further in higher resolution simulations, which implies that it is important to sufficiently resolve the velocity gradient. It can also be clearly seen that the two big eddies, induced by KHI, and the mixed bubble gas they drag along with them, get much better resolved with higher number of cells. This is needed to quantify e.g. viscous heating (see section 4.1.3). The highest resolved simulation shows higher tracer mass fractions at the top of the bubble, which indicates a suppression of RTI compared to the fiducial resolution run. Also the eddies stay more compacted and pronounced over time.

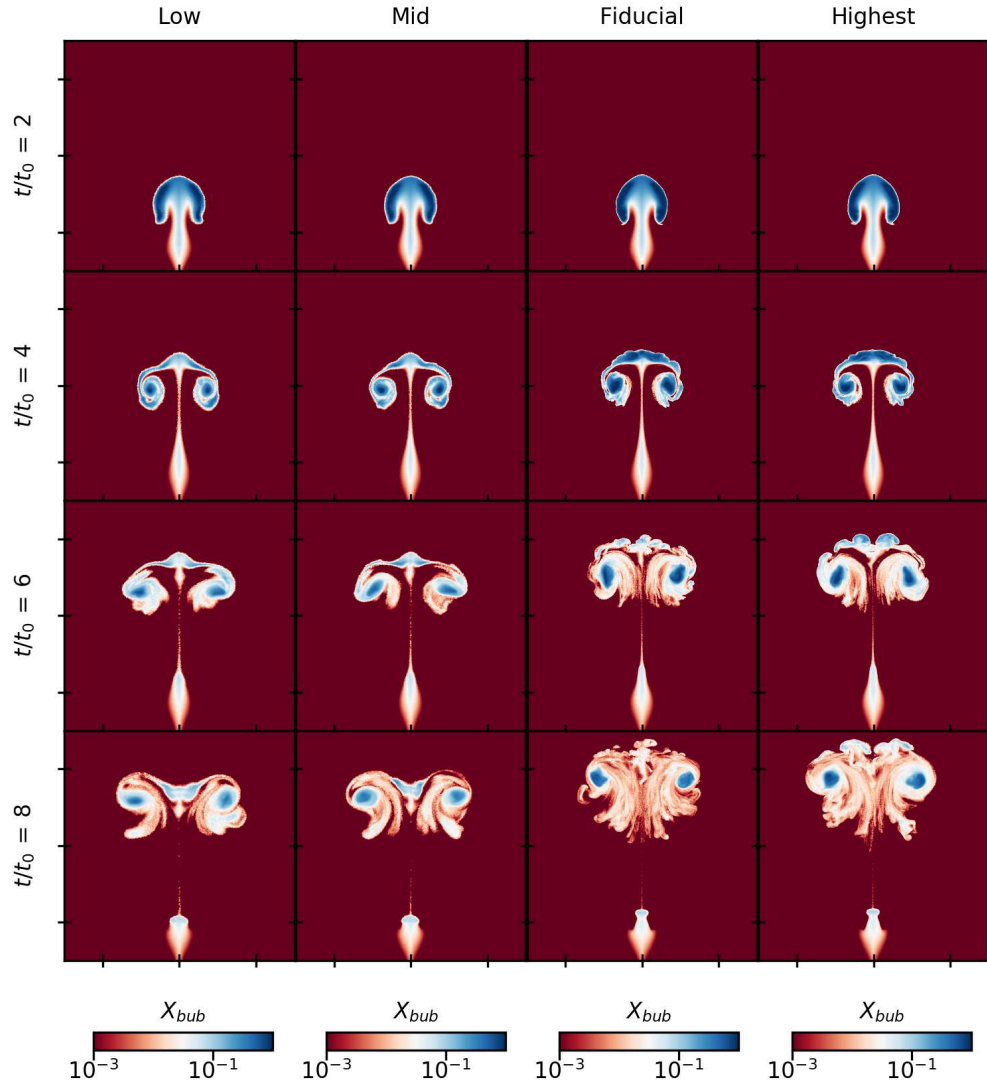


Figure 4.24.: Projected slices of the  $x$ - $y$  midplane showing the tracer mass fraction  $X_{\text{bub}}$  for each of our hydrodynamic resolutions. Each panel spans a spatial domain corresponding to dimensions  $x \in [-1.5 r_0, 1.5 r_0]$  and  $y \in [0, 3 r_0]$ . The thin projections in  $z$ -direction have width  $dr = 0.066 r_0$  centered at  $z = 0$ .

As already mentioned above, there seems to be a jump in mixing content of bubble material with the ambient gas between the medium and the fiducial resolution. We quantify the amount of mixed gas by plotting the normalised volume fraction as a function of the tracer mass fraction at

time  $t/t_0 = 8$  in figure 4.25. Both of the higher resolution runs have their values of the covering volume fraction shifted towards lower tracer mass fractions compared to the lower resolution runs. The former ones also peak at higher volume fractions of mixed gas. This shows quantitatively that our higher resolved simulations result in more mixing. This is in contrast to the resolution studies by Bourne and Sijacki (2017) and Ehlert et al. (2018) with jet-inflated bubbles, where they find mixing to be suppressed at higher resolutions. In Bourne and Sijacki (2017) and Ehlert et al. (2018) this is due to less numerical mixing in *AREPO*. We believe our higher resolutions induce more mixing because the hydrodynamic KHI is significantly better resolved than in our lower resolution runs. Indeed, KHI rolls are visible at the leading edge of the bubble in our two higher resolved runs, but not in the lower resolution runs. In order to understand why our simulations have mixing via KHI and Ehlert et al. (2018) do not, we estimate the growth rate of the KHI in the two setups. To quantify the growth rate of the hydrodynamic KHI, we take its dispersion relation for a planar sheet in the incompressible, inviscid limit Chandrasekhar 1981, see also section two in Berlok and Pfrommer (2019):

$$\omega_{\pm} = \frac{\delta \pm i2\sqrt{1+\delta}}{2+\delta} \Delta v k, \quad (4.15)$$

where  $k$  is the wavenumber (related to the wavelength of the roll by  $k = 2\pi/\lambda$ ),  $\Delta v$  is the flow velocity and  $\delta$  is the density contrast  $\delta = \rho_{\text{bub}}/\rho_{\text{amb}} - 1$ . The growth rate  $\sigma$  is given by the imaginary part of equation (4.15), such that  $\sigma = -\text{Im}(\omega)$ . Thus, for a density contrast of  $\rho_{\text{bub}}/\rho_{\text{amb}} = 10^{-2}$  we get a growth rate of  $\sigma \approx 0.2\Delta v k$ , which resembles our model setup. Ehlert et al. (2018) fix the density contrast to be  $\rho_{\text{bub}}/\rho_{\text{amb}} = 10^{-4}$ , which yields a growth rate of  $\sigma \approx 0.02\Delta v k$ . So in our simulations, the KHI is one order of magnitude more efficient than in the setup by Ehlert et al. (2018). Since numerical dissipation depends on the grid resolution and the KHI growth rate is proportional to the wavenumber, ergo the grid resolution (Berlok and Pfrommer, 2019), we conclude that the large difference in density contrast might explain why mixing is not suppressed in our fiducial simulation.

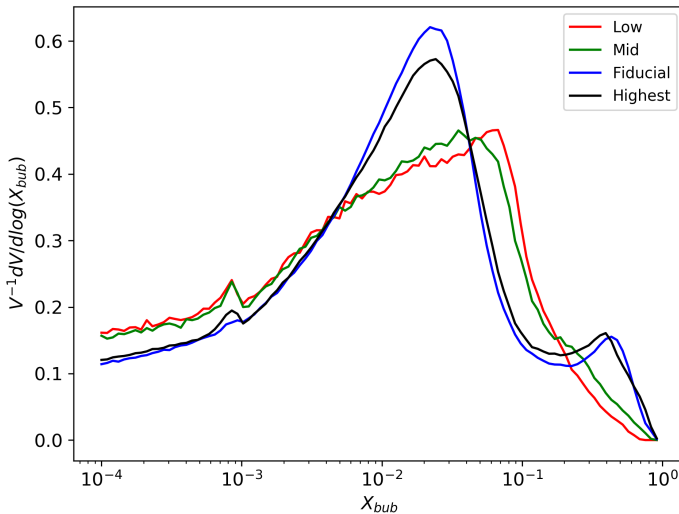


Figure 4.25.: Normalised volume covering fraction of a given tracer mass fraction of the hydrodynamic runs for each of our numerical resolutions at time  $t/t_0 = 8$  to show the mixing efficiency of the bubble. The volume covering fraction is plotted in accordance to Ehlert et al. (2018).

# Chapter 5.

## Discussion

We have shown in section 4.4 with our simulations that not even a turbulent ICM is capable of sufficiently heating the cluster atmosphere to levels of radiative cooling in a volume filling fashion. Our heating estimates are thereby restricted to only consider parallel viscous heating rates arising from anisotropic pressures. Additional heating channels need to be taken into account for a total picture, but quantifying all of them would be far beyond the scope of this thesis. A promising source is heating by mixing as supported by *Hitomi* observations of the Perseus cluster core (Hillel and Soker, 2017). The heating-mixing mechanism is caused by dissipation of modes induced by KHI. To get the heating rate via mixing of the ambient cluster gas we would need to calculate the time derivative of the ambient thermal energy,  $\int_V u(X_{\text{bub}} - 1) dV$ , since we expect the thermal energy at the bubble rim to increase if mixing is dominant (Yang and Reynolds, 2016a). This estimate will still not yield how much of the heating is due to mixing, because an uncertain fraction of this rate is due to  $p dV$  work. Since our ICs are based on the setup by Dong and Stone (2009), we can refer to their findings that the internal energy of buoyant bubbles only increases by a few percent at late times concluding that heating by mixing is not very effective for an initially static ICM. However, Dong and Stone (2009) do not include a turbulent configuration of the ambient gas in their studies. Actually, a turbulent atmosphere enhances mixing in comparison to our quiescent ICM with the same thermal-to-magnetic pressure ratio. But the turbulent mixing rate does not become more efficient than the  $\beta = 10^6$  case and even for the latter Dong and Stone (2009) find that changes in internal energy are not notable. Hence, we suppose that mixing is subdominant as a heating source in our simulations.

If we want to increase the heating rate based on viscous heating alone, we probably need to include AGN-driven bubbles in our ICs, where lobes are inflated self-consistently by sub-relativistic jets. These jets will drive and inject turbulent energy into the cluster core region with high amounts of vorticity in their wake. Additionally, the jet interior will have a highly tangled magnetic field, whose field lines get strongly bended. This turbulent confinement leads to increasing levels of rate of strain and magnetic field strength and eventually higher  $Q^+$  rates. How much closer that viscous heating rate will be to  $Q^-$  compared to our setup with artificially static bubbles might depend on the specific jet model implementation. So for instance, whether multiple epochs of jet activity will be simulated to inject turbulent modes on a roughly constant rate, which can ultimately lead to isotropic jet heating of the entire cluster core region (McNamara and Nulsen, 2012). Here, isotropic means that due to jet precession and atmospheric pressure gradients multiple sequentially inflated lobes can possibly deposit their energy via weak shocks and sound waves (Bambic and Reynolds, 2019) over much of the cluster volume of the inner atmosphere. Such a fully turbulence-driven cluster atmosphere will theoretically be capable of balancing  $Q^+/Q^- \sim 1$  as we have shown in figure 4.18.

As Kunz et al. (2011) show, the global self-regulated mechanism of viscous heating and radiative cooling, which can mitigate cooling flows and prevent a cluster core collapse, can probably also be established locally. If we recall equation (4.14) from section 4.3 for the viscous heating rate (per unit volume),

$$Q_{\text{lim}}^+ = 7.7 \times 10^{-27} \xi^2 \left( \frac{\|\mathbf{B}\|}{10 \mu\text{G}} \right)^4 \left( \frac{k_B T}{3.34 \text{ keV}} \right)^{-5/2} \text{ erg cm}^{-3} \text{ s}^{-1},$$

we infer that the strong dependence on  $\|\mathbf{B}\|$  comprises the implicit dependence on density and the rate of strain of the turbulence. So, as turbulent velocities increase, concomitant will the magnetic field strength and thus the dissipation rate  $Q^+$  will increase accordingly. Therefore,  $Q^+$  can be locally self-regulating, in a sense that it is completely independent of the AGN, acting as an external source providing the turbulent energy globally (Kunz et al., 2011). But with the addition, that the local self-regulation is only maintained as long as there is enough turbulence to pin the pressure anisotropy at its stability thresholds. Kunz et al. (2011) note that due to the constraint on the turbulent rate of strain (set by micro-scale instabilities), not all of the external power injected by driving turbulence is necessarily thermalized locally. In fact, the turbulence may have an effective excess in its amount of power, where only those turbulent modes get dissipated at the local viscous scale that do not trigger the microinstabilities. The remaining power could be transported elsewhere (Kunz et al., 2011).

## 5.1. Effective Reynolds Number

By analysing the unlimited fiducial run in section 4.1, we also calculated the parallel viscous heating rate  $Q_{\text{lim}}^+$ , where  $\Delta p$  is artificially restricted according to the micro-scale limiters in the post-processing analysis. With the model *xB6N2lim* the entire simulation has already been run while applying the hard-wall limiters to the pressure anisotropy, which is affecting the evolution of the bubble significantly (see figure 4.10). Thus, we have studied how the viscous heating rate changes in this case in figure 4.11. St-Onge et al. (2020) find that if  $\Delta p_{\text{lim}}$  is limited to remain within the firehose and mirror instability thresholds according to inequality (2.48), then implies an enhanced collisionality in the unstable regions given by

$$\nu_{\text{eff}} \sim \beta(\mathbf{b}\mathbf{b} : \nabla\mathbf{v}), \quad (5.1)$$

where  $\nu_{\text{eff}}$  is the effective ion-ion collision frequency and the right-hand side is the product of the plasma beta and the rate of strain while assuming incompressibility (see equation (2.44)). In case of *xB6N2lim*, we have set  $\beta = 10^6$  and thus according to equation (5.1), the enhanced collisionality will reduce viscous stresses drastically, which we could verify with our simulations, because *xB6N2lim* and *hydro* are very close in terms of mixing efficiency and show much lower dye entropy  $S$  compared to the unlimited run *xB6N2*. From equation (5.1) Melville et al. (2016) and St-Onge et al. (2020) estimate the effective parallel-viscous Reynolds number  $\text{Re}_{\parallel\text{eff}}$  as

$$\text{Re}_{\parallel\text{eff}} = \frac{v_L L}{\mu_{\parallel\text{eff}}} \sim \beta^2 \mathcal{M}^4, \quad (5.2)$$

where  $\mu_{\parallel\text{eff}} = v_{\text{th}}^2 / \nu_{\text{eff}}$  is the effective parallel viscosity and  $\mathcal{M} = v_L / v_{\text{th}}$  is the mach number (see also section 2.3.4). So, for  $\beta = 10^6$  the effective viscosity becomes negligible and in turn  $\text{Re}_{\parallel\text{eff}}$  indicates a highly turbulent medium. As the KHI and RTI inject energy into the turbulent cascade via field-stretching/compressing turbulent velocities (see section 2.3.3), the parallel rate of strain scales as  $|\mathbf{b}\mathbf{b} : \nabla\mathbf{v}| \sim v_L / l_{\parallel} \propto l_{\parallel}^{-2/3}$  (St-Onge et al., 2020). Hence the magnitude of the rate of strain is largest at the effective parallel viscous scale  $l_{\text{eff}}$ , where turbulent motions are dissipated. At this viscous cutoff, St-Onge et al. (2020) find that

$$l_{\text{eff}} \sim L \text{Re}_{\parallel\text{eff}}^{-3/4} \propto B^3, \quad (5.3)$$

which is smaller than the unlimited viscous scale  $l_{\text{visc}}$ , which we have introduced in section 2.3.3:  $V^{1/3} \sim \lambda_{\text{mfp}} \sim l_{\text{visc}} > l_{\text{eff}}$ . While choosing higher values for  $\beta$ ,  $B$  is decreasing and thus lowering

the viscous cutoff scale, which in turn requires higher numerical resolution in order to correctly picture the level of viscosity in the system.

The effective Reynolds number also needs to be accounted for when considering the numerical diffusivity for the highest wavenumbers limited by the grid resolution in a given volume (Donnert et al., 2018). They argue that  $\text{Re}$  of a turbulent fluid flow is not only set by the viscous dissipation scale but is also reduced by the cut-off of velocity power at the numerical dissipation scale. So, if the grid resolution does not resolve the smallest scales of the velocity (or magnetic field) power spectrum, numerical errors take away that power, which effectively reduces the rate of strain and thus results in smaller viscous heating rates. In other words, a less diffusive numerical code reaches higher effective Reynolds numbers and a more broader dynamical range at the same resolution. This relation is quantified by Donnert et al. (2018) as

$$\text{Re}_{\text{eff}} \approx \left( \frac{L}{\epsilon \Delta x} \right)^{4/3}, \quad (5.4)$$

where  $L$  is the outer injection scale,  $\Delta x = V^{1/3}$  is the resolution element and  $\epsilon$  is a factor depending on the diffusivity of the numerical method used. For the finite-volume code *AREPO* this factor is assumed to be  $\epsilon \approx 7$ , which is smaller than for smoothed-particle hydrodynamics (SPH) or hybrid codes (see references in Donnert et al. (2018)). Equation (5.4) implies that decreasing either the factor  $\epsilon$  or the grid resolution increases  $\text{Re}_{\text{eff}}$ , which in turn broadens the inertial range (shrinks the effective dissipation scale), increases the velocity power (rate of strain) on small scales and reduces viscosity.

Furthermore, bubble stability crucially depends on the numerical method used while the re-solution is kept the same. What role different hydrodynamical schemes play on the evolution of buoyantly rising bubbles has been studied by Ogiya et al. (2018). After initialising each simulation in the same way, Ogiya et al. (2018) find that KHI fully dissolves the bubble in the ICM on relatively short time-scales for the meshless finite mass (MFM) scheme and the *RAMSES* simulations, while for smoothed-particle hydrodynamics (SPH) the bubble survives. So the choice of a hydrodynamical solver can lead to systematic differences on the outcome, whether it captures the relevant fluid instabilities.

## 5.2. Limitations

As pointed out in chapter 3, we model an idealized cluster core in order to isolate the effects of Braginskii viscosity in a weakly collisional ICM. Therefore, we have to neglect some realismness in our cluster model in favor of comprehensibility of the underlying physical processes. Step by step we add more complexity to our simulations, but some limitations remain untouched nonetheless.

At first, instead of a CC, we assume a perfect isothermal ICM with no small- or large-scale gas motions throughout the atmosphere. In real systems this is rarely the case since the gas can be disturbed by recent merger events or the AGN activity itself. So, the cluster atmosphere does not need to be necessarily relaxed. Nonetheless, we set buoyant bubbles into a hydrostatic equilibrium modelled by a single- $\beta$  density profile. Such beta profiles sufficiently fit the density distribution and X-ray surface brightness profiles for an isothermal cluster, but studies find that they yield wrong mass profiles in the cluster outskirts (Xue and Wu, 2000). Nevertheless, since we model the core region, we are not computing the mass distribution at radii near  $r_{200}$ . Moreover, the gravitational potential is following the beta profile instead of a more sophisticated NFW distribution for dark matter.

We do not model the formation and inflation of the bubble via a powerful radio jet. In fact, we completely ignore the jet-feedback mechanism (JFM) (Soker, 2016), where jet-driven bubbles are inflated over multiple epochs of activity. Soker (2016) find that the morphology of simulated bubbles matches with observations, if they are inflated by slow (sub-relativistic), massive jets. The jets play a crucial role affecting the stability and mixing efficiency of the longevity of the bubbles after they are inflated. According to Soker (2016), studying the dynamics of the buoyant evolution of a bubble initially at rest is not very desirable and simulations approaching the JFM should be favoured.

As mentioned in section 2.2.1, the exact composition of the bubble interior cannot be inferred directly due to the very low bubble densities. But observations suggest that radio lobes are actually filled with a strongly magnetized relativistic plasma (Laing and Bridle, 2014). An additional pressure component is needed for the bubbles to explain the discrepancy with the observed ambient ICM pressure (Croston and Hardcastle, 2014), see section 2.2.3. CR protons seem to be a likely candidate for such a pressure contribution. These protons could be accelerated in the jet to build a relativistic plasma population (Pfrommer, 2013). However, we treat the bubble material simply as a very hot thermal gas with  $\gamma = 5/3$  and omit CR protons completely, although CR heating can become quite efficient in the very centers of CCs to offset radiative cooling (Jacob and Pfrommer, 2017b). In addition, we assume that the lobe interior is magnetized the same way as the ambient ICM (either uniform or turbulent), whereas numerical studies find that very likely a toroidal magnetic field dominates and stabilizes the bubble inflated by energetic jets (O’Neill and Jones, 2010; Huarte-Espinosa et al., 2011; Soker, 2016).

Furthermore, we lack an explicit term for radiative cooling in our energy equation (2.36). Using equation (2.12), the cooling time at the very center of our cluster core is  $t_{\text{cool}} \approx 1.8 \text{ Gyr}$ , which increases to  $t_{\text{cool}} \approx 9 \text{ Gyr}$  at the outer boundary of our domain. Hence, the cluster cooling times are longer than the simulation times, allowing us to neglect cooling in our simulations. However in real CCs, cooling gas accretes onto the central SMBH and induces motions. We also neglect thermal conductivity in terms of an anisotropic heat flux tensor in our set of Braginskii-MHD equations. On the one hand, anisotropic conduction can make the radial temperature gradient unstable in CCs and thus introduce the heat flux driven buoyancy instability (HBI), which may suppress anisotropic thermal conduction (Kunz et al., 2012; McNamara and Nulsen, 2012). On the other hand, if the CC is threaded with a tangled magnetic field, thermal conductivity is suppressed below the Spitzer value by at least one order of magnitude (McNamara and Nulsen, 2007). Conductive heating is neither thermally stable (Kunz et al., 2011) nor can it balance radiative cooling throughout the core (Yang and Reynolds, 2016b), but probably becomes efficient in the outer skirts of the cluster (Jacob and Pfrommer, 2017a).

We also consider the plasma fluid as a mono-phase fluid, only consisting of fully ionized hydrogen, whereas in real clusters the hydrogen mass fraction is about 3/4 (with 1/4 helium mass fraction and negligible metal fraction). Taking this into account would not just tune the mean molecular weight, it would also affect the viscosity coefficient, since  $\nu_{||}$  then depends on the collision frequencies  $\nu_{\text{H-H}}$ ,  $\nu_{\text{H-He}}$  and  $\nu_{\text{He-He}}$  (see Appendix B in Berlok and Pessah 2015).

Lastly, we do not attempt to include the temperature dependence of  $\nu_{||} \propto T^{5/2}/\rho$  according to Spitzer (1962) in our calculations. However, Reynolds et al. (2005) state that they could confirm with their simulations that the evolution of the bubbles is not qualitatively affected by the constant non-Spitzer  $\nu_{||}$  assumption. On the other hand, the temperature dependent viscosity coefficient inside lobes would very likely be unphysically large. If such a bubble is i.e. 100 times hotter (and in turn 100 times less dense) than the ambient ICM, the Spitzer viscosity would be three orders of magnitude greater. Therefore, numerical simulations use an upper limit for  $\mu_{\text{sp}}$  (Kingsland et al., 2019).

# Chapter 6.

## Conclusions and Future Perspective

We have performed 3D Braginskii-MHD simulations of artificial AGN-inflated bubbles in an isothermal cluster core to study the buoyant rise of these bubbles and its evolution including the effects of weak magnetic fields and anisotropic viscosity. We have varied different cases of viscosity (constant factor, un-/limited, isotropic) and the magnetic field (geometry, strength) to increase the level of complexity step by step in order to get a comprehensible picture on the impacts on the modelled ICM. Our conclusions are as follows:

1. If the magnetic tensions are negligibly weak ( $\beta = 10^6$ ) and Braginskii viscosity sufficiently strong, the bubble evolution is drastically altered whether the pressure anisotropy  $\Delta p$  is bounded due to micro-scale instabilities or not. If pressure anisotropy is limited within marginal stability levels, the very high plasma beta shrinks the range of  $\Delta p_{\text{lim}}$  significantly and concomitant the viscous stresses are highly suppressed by the microinstabilities such that they can no longer prevent the bubbles from disruption, resembling the inviscid case. If  $\Delta p$  is not limited, viscous stresses are capable of effectively suppressing macro-scale instabilities like RTI and KHI such that the bubble rim stays coherent over much longer time-scales compared to the inviscid case. Independent of  $\Delta p$ , we show that a very high density contrast between bubble and ambient gas density suppresses KHI as well.
2. Anisotropic dissipation of momentum transport is distinctively affecting the bubble morphology by initiating uniformly aligned magnetic field lines into a weakly collisional plasma. In the direction parallel to the field, macro-scale instabilities are efficiently suppressed, while having little effect perpendicular to the field.
3. The magnetic field is not dramatically enhanced at the bubble front as it buoyantly rises. The field lines are probably not compressed as much to form a efficient draping layer in order to provide sufficient stability.
4. We computed the mixing efficiency of the bubble interior with the ambient gas in three different ways by deriving the volume covering fraction, the gas clumping factor and the dye entropy  $S$ . We conclude that analysing the dye entropy is the most insightful method while being intellegibly to interpret. We find the following ordering:  $S_{\text{hydro}} > S_{\text{lim}} > S_{\text{Brag}} > S_{\text{iso}}$ .
5. Isotropic Navier-Stokes viscosity resembles observed X-ray cavities quite well and suppresses RTI and KHI effectively over the entire simulation time. None of our other simulated models reaches mixing rates as low as with isotropic viscosity. However, we are probably overestimating the isotropic viscosity coefficient by a factor of  $\sim 800$ .
6. Using a stronger magnetic field, where  $\beta = 10^2$  is in accordance with observed values of galaxy clusters, reveals an invariance in bubble evolution in terms of mixing efficiency and viscous heating regardless of whether limiting pressure anisotropy or not. We show that the plasma beta is high enough to yield a broader range for the rate of strain such that the production of  $\Delta p_{\text{lim}}$  rarely triggers microinstabilities, effectively resulting in unsuppressed Braginskii viscosity.
7. Production of anisotropic pressure leads to parallel viscous heating, which depends on the rate of strain of turbulent motions and enhanced magnetic field strength induced by

strongly bended field lines. The inferred viscous heating rates  $Q^+$  are not high enough to balance radiative cooling  $Q^-$  in a volume filling fashion. This shows that viscous dissipation is not very efficient in heating the ICM in our simulations.

- Averaged over the entire cluster (regardless of field geometry):  $Q^+/Q^- \sim 10^{-3}$
  - Averaged over the bubble region (regardless of field geometry):  $Q^+/Q^- \lesssim 10^{-1}$
  - $Q^+$  seems to be independent on the initial plasma beta, if one ignores kinetic limiters
  - As predicted by [Kunz et al. \(2011\)](#), if levels of pressure anisotropy reach marginal stability thresholds throughout the entire spatial domain where  $\beta = 10^2$ :  $Q^+/Q^- \sim 1$
  - For  $\beta = 10^6$ :  $Q^+ \sim (10 - 100) \times Q_{\text{lim}}^+$
  - For  $\beta = 10^2$ :  $Q^+ \sim Q_{\text{lim}}^+$
8. If the ICM is turbulent with an initial magnetic field following a Kolmogorov power spectrum, not even magnetic field lines with coherence lengths greater than the bubble size can prevent the deformation of the bubbles. The contribution of viscous heating from ambient turbulent motions has no significant impact on the  $Q^+/Q^-$  ratio as these motions get relatively quickly dissipated and are not re-injected again.

In future work, it will be insightful to study the effects of Braginskii-MHD on a more sophisticated cool-core cluster model in order to investigate whether Braginskii viscosity is a primary mechanism for suppressing fluid instabilities ([Kingsland et al., 2019](#)) and/or viscous heating is a significant heating channel to viably quench cooling flows. Such advanced simulations should include self-consistently inflated bubbles driven by AGN jets, a NFW density profile, a mixture of relativistic CRs and hot thermal gas for the bubble interior and an initial tangled magnetic field, whose turbulent energy will be injected over multiple AGN outbursts. The simulations should be able to resolve the (effective) viscous dissipation scale and account for micro-scale instabilities in form of e.g. hard-wall limiters to capture the physics of the ICM correctly.

# Appendix A.

## Supplementary Figures

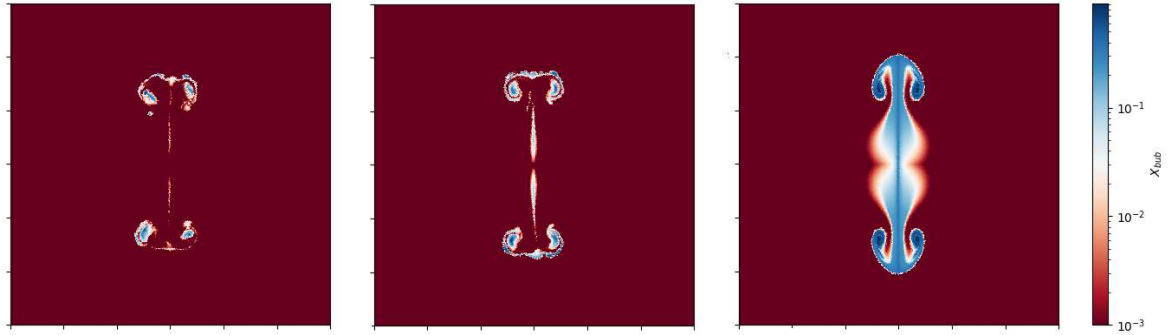


Figure A.1.: Low resolution simulations of the *hydro* model which have been run with different values of the smoothing parameter  $a$  for the analytical profile of the tracer mass fraction used in equation (3.11). From left to right  $a$  is equal to 0.01, 0.05 and 0.5, respectively.

Symbol	Quantity
$\beta$	plasma beta
$\beta$	index of King model
$c$	speed of light
$c_s$	isothermal sound speed
$g$	gravitational acceleration
$G$	gravitational constant
$\gamma$	ratio of specific heats
$g_{\text{ff}}$	Gaunt factor
$h$	Hubble parameter
$H_0$	Hubble constant
$\hbar$	reduced Planck constant
$k$	wave number
$k_B$	Boltzmann constant
$k_B T$	temperature in eV
$L$	characteristic length scale
$m_e$	electron mass per particle
$m_p$	proton mass per particle

Table A.1.: List of common physical quantities used in this thesis.

Symbol	Quantity
$\mu$	mean molecular weight
$\mu$	dynamic viscosity
$n_e$	electron number density
$n_i$	ion number density
$\nu_{ii}$	ion-ion collision frequency
$\nu$	kinematic viscosity
$\nu_{\parallel}$	anisotropic viscosity
$P_B$	magnetic pressure
$P_{\text{th}}$	thermal pressure
$\rho_{\text{amb}}$	ambient density
$\rho_{\text{bub}}$	bubble density
$S$	entropy
$T_g$	gas temperature in K
$t_H$	Hubble time
$u$	internal energy
$v_{\text{th}}$	thermal velocity
$\omega$	angular frequency
$Ze$	electrical charge

Table A.2.: List of common physical quantities, continued.

## Appendix B.

### Bibliography

- Alfvén, H. (1942). Existence of Electromagnetic-Hydrodynamic Waves. *Nature*, 150(3805):405–406.
- Bambic, C. J. and Reynolds, C. S. (2019). Efficient Production of Sound Waves by AGN Jets in the Intracluster Medium. *Astrophys. J.*, 886(2):78.
- Bauer, F. E., Fabian, A. C., Sanders, J. S., Allen, S. W., and Johnstone, R. M. (2005). The prevalence of cooling cores in clusters of galaxies at  $z \approx 0.15\text{--}0.4$ . *Mon. Not. R. Astron. Soc.*, 359(4):1481–1490.
- Baumjohann, W. and Treumann, R. A. (1997). *Basic Space Plasma Physics*. Imperial College Press, first edition.
- Berlok, T. (2014). Instabilities in weakly magnetized, hot, heterogenous plasmas: Magnetic fields and the helium content in the intracluster medium. Master’s thesis, University of Copenhagen. Supervisor: Martin E. Pessah.
- Berlok, T., Pakmor, R., and Pfrommer, C. (2019). Braginskii viscosity on an unstructured, moving mesh accelerated with super-time-stepping. *Mon. Not. R. Astron. Soc.*, 2938:2919–2938.
- Berlok, T. and Pessah, M. E. (2015). PLASMA INSTABILITIES in the CONTEXT of CURRENT HELIUM SEDIMENTATION MODELS: DYNAMICAL IMPLICATIONS for the ICM in GALAXY CLUSTERS. *Astrophys. J.*, 813(1):22.
- Berlok, T. and Pfrommer, C. (2019). On the Kelvin–Helmholtz instability with smooth initial conditions – linear theory and simulations. *MNRAS*, 485(1):908–923.
- Birzan, L., McNamara, B. R., Nulsen, P. E. J., Carilli, C. L., and Wise, M. W. (2008). Radiative Efficiency and Content of Extragalactic Radio Sources: Toward a Universal Scaling Relation between Jet Power and Radio Power. *Astrophys. J.*, 686(2):859–880.
- Birzan, L., Rafferty, D. A., McNamara, B. R., Wise, M. W., and Nulsen, P. E. J. (2004). A Systematic Study of Radio-induced X-Ray Cavities in Clusters, Groups, and Galaxies. *Astrophys. J.*, 607(2):800–809.
- Blanton, E. L., Clarke, T. E., Sarazin, C. L., Randall, S. W., and McNamara, B. R. (2010). Active galactic nucleus feedback in clusters of galaxies. *Proc. Natl. Acad. Sci. U. S. A.*, 107(16):7174–7178.
- Blanton, E. L., Sarazin, C. L., and McNamara, B. R. (2003). Chandra Observation of the Cooling Flow Cluster Abell 2052. *Astrophys. J.*, 585(1):227–243.
- Blanton, E. L., Sarazin, C. L., McNamara, B. R., and Wise, M. W. (2001). [ITAL]Chandra[/ITAL] Observation of the Radio Source/X-Ray Gas Interaction in the Cooling Flow Cluster Abell 2052. *Astrophys. J.*, 558(1):L15–L18.
- Boettcher, M., Harris, D. E., and Krawczynski, H. (2012). *Relativistic Jets from Active Galactic Nuclei*. Wiley-VCH Verlag, first edition.
- Bonafede, A., Feretti, L., Murgia, M., Govoni, F., Giovannini, G., Dallacasa, D., Dolag, K., and Taylor, G. B. (2010). The coma cluster magnetic field from faraday rotation measures. *Astron. Astrophys.*, 513(5):1–21.
- Bourne, M. A. and Sijacki, D. (2017). AGN jet feedback on a moving mesh: cocoon inflation, gas flows and turbulence. *MNRAS*, 472(4):4707–4735.
- Bourne, M. A., Sijacki, D., and Puchwein, E. (2019). AGN jet feedback on a moving mesh: Lobe energetics and X-ray properties in a realistic cluster environment. *Mon. Not. R. Astron. Soc.*, 490(1):343–349.
- Braginskii, S. I. (1965). Transport Processes in a Plasma. *Reviews of Plasma Physics*, 1:205.
- Brüggen, M. and Kaiser, C. R. (2001). Buoyant radio plasma in clusters of galaxies. *Mon. Not. R. Astron. Soc.*, 325(2):676–684.
- Brüggen, M. and Scannapieco, E. (2009). Self-regulation of active galactic nuclei in galaxy clusters. *Mon. Not. R. Astron. Soc.*, 398(2):548–560.

- Brunetti, G. and Lazarian, A. (2007). Compressible turbulence in galaxy clusters: Physics and stochastic particle re-acceleration. *Mon. Not. R. Astron. Soc.*, 378(1):245–275.
- Carilli, C. L. and Taylor, G. B. (2002). Cluster Magnetic Fields. *Annu. Rev. Astron. Astrophys.*, 40(1):319–348.
- Carroll, B. W. and Ostlie, D. A. (2014). *An Introduction to Modern Astrophysics*, volume Pearson custom library. Pearson Education Limited, second edition.
- Cavaliere, A. and Fusco-Femiano, R. (1976). X-rays from hot plasma in clusters of galaxies. *Astronomy and Astrophysics*, 49:137–144.
- Chandrasekhar, S. (1981). *Hydrodynamic and hydromagnetic stability*. Dover Publications, Inc., New York, second edition.
- Chen, C. H. K., Matteini, L., Schekochihin, A. A., Stevens, M. L., Salem, C. S., Maruca, B. A., Kunz, M. W., and Bale, S. D. (2016). Multi-Species Measurements of the Firehose and Mirror Instability Thresholds in the Solar Wind. *Astrophys. J.*, 825(2):L26.
- Chew, G. F., Goldberger, M. L., and Low, F. E. (1956). The Boltzmann Equation and the One-Fluid Hydro-magnetic Equations in the Absence of Particle Collisions. *Proceedings of the Royal Society of London Series A*, 236(1204):112–118.
- Churazov, E., Bruggen, M., Kaiser, C. R., Böhringer, H., and Forman, W. (2001). Evolution of buoyant bubbles in m87. *The Astrophysical Journal*, 554(1):261–273.
- Churazov, E., Sunyaev, R., Forman, W., and Böhringer, H. (2002). Cooling flows as a calorimeter of active galactic nucleus mechanical power. *Mon. Not. R. Astron. Soc.*, 332(3):729–734.
- Clarke, T. E., Kronberg, P. P., and Böhringer, H. (2001). A New Radio-X-Ray Probe of Galaxy Cluster Magnetic Fields. *Astrophys. J.*, 547(2):L111–L114.
- Courant, R., Friedrichs, K., and Lewy, H. (1928). Über die partiellen Differenzengleichungen der mathematischen Physik. *Mathematische Annalen*, 100:32–74.
- Croston, J. H. and Hardcastle, M. J. (2014). The particle content of low-power radio galaxies in groups and clusters. *Mon. Not. R. Astron. Soc.*, 438(4):3310–3321.
- Croston, J. H., Hardcastle, M. J., Birkinshaw, M., Worrall, D. M., and Laing, R. A. (2008). An XMM-Newton study of the environments, particle content and impact of low-power radio galaxies. *Mon. Not. R. Astron. Soc.*, 386(3):1709–1728.
- Dolag, K., Bykov, A., and Diaferio, A. (2008). Non-thermal processes in cosmological simulations. *Space Science Reviews*, 134:311–335.
- Dong, R. and Stone, J. M. (2009). Buoyant bubbles in intracluster gas: Effects of magnetic fields and anisotropic viscosity. *Astrophys. J.*, 704(2):1309–1320.
- Donnert, J., Vazza, F., Brüggen, M., and ZuHone, J. (2018). *Magnetic Field Amplification in Galaxy Clusters and Its Simulation*, volume 214. The Author(s).
- Dopita, M. A. and Sutherland, R. S. (2003). *Astrophysics of the Diffuse Universe*. Springer Berlin Heidelberg.
- Dursi, L. J. and Pfrommer, C. (2008). Draping of Cluster Magnetic Fields over Bullets and Bubbles—Morphology and Dynamic Effects. *Astrophys. J.*, 677(2):993–1018.
- Ehlert, K., Weinberger, R., Pfrommer, C., Pakmor, R., and Springel, V. (2018). Simulations of the dynamics of magnetized jets and cosmic rays in galaxy clusters. *Mon. Not. R. Astron. Soc.*, 481(3):2878–2900.
- Fabian, A. C. (2012). Observational Evidence of AGN Feedback.
- Fabian, A. C., Celotti, A., Blundell, K. M., Kassim, N. E., and Perley, R. A. (2002). The properties of the X-ray holes in the intracluster medium of the Perseus cluster. *Mon. Not. R. Astron. Soc.*, 331(2):369–375.
- Fabian, A. C. and Sanders, J. S. (2007). Heating and cooling in the Perseus cluster core. *ESO Astrophys. Symp.*, 2007:65–73.

- Fabian, A. C., Sanders, J. S., Allen, S. W., Canning, R. E., Churazov, E., Crawford, C. S., Forman, W., Gabany, J., Hlavacek-Larrondo, J., Johnstone, R. M., Russell, H. R., Reynolds, C. S., Salomé, P., Taylor, G. B., and Young, A. J. (2011). A wide Chandra view of the core of the Perseus cluster. *Mon. Not. R. Astron. Soc.*, 418(4):2154–2164.
- Fabian, A. C., Sanders, J. S., Ettori, S., Taylor, G. B., Allen, S. W., Crawford, C. S., Iwasawa, K., Johnstone, R. M., and Ogle, P. M. (2000). Chandra imaging of the complex X-ray core of the Perseus cluster. *Mon. Not. R. Astron. Soc.*, 318(4):3–8.
- Fabian, A. C., Walker, S. A., Russell, H. R., Pinto, C., Sanders, J. S., and Reynolds, C. S. (2017). Do sound waves transport the AGN energy in the Perseus cluster? *Mon. Not. R. Astron. Soc. Lett.*, 464(1):L1–L5.
- Ferrari, C., Govoni, F., Schindler, S., Bykov, A. M., and Rephaeli, Y. (2008). Observations of Extended Radio Emission in Clusters. *Space Science Reviews*, 134(1-4):93–118.
- Gardini, A. (2007). Buoyant bubbles in a cooling intracluster medium. *Astron. Astrophys.*, 464(1):143–154.
- Gaspari, M. and Churazov, E. (2013). Constraining turbulence and conduction in the hot ICM through density perturbations. *Astron. Astrophys.*, 559:1–18.
- Giacconi, R., Branduardi, G., Briel, U., Epstein, A., Fabricant, D., Feigelson, E., et al. (1979). The einstein (heao 2) x-ray observatory. *The Astrophysical Journal*, 230:540–550.
- Gilkis, A. and Soker, N. (2012). Heating the intra-cluster medium perpendicular to the jets axis. *Mon. Not. R. Astron. Soc.*, 427(2):1482–1489.
- Gitti, M., Brighenti, F., and McNamara, B. R. (2012). Evidence for agn feedback in galaxy clusters and groups. *Adv. Astron.*, 2012(Icm).
- Gitti, M., McNamara, B. R., Nulsen, P. E. J., and Wise, M. W. (2007). Cosmological Effects of Powerful AGN Outbursts in Galaxy Clusters - Insights from an XMM-Newton Observation of MS 0735+7421. *Astrophys. J.*, 660(2):1118–1136.
- Govoni, F., Dolag, K., Murgia, M., Feretti, L., Schindler, S., Giovannini, G., Boschin, W., Vacca, V., and Bonafede, A. (2010). Rotation measures of radio sources in hot galaxy clusters. *Astron. Astrophys.*, 522(8):1–23.
- Guo, X., Sironi, L., and Narayan, R. (2017). Electron Heating in Low-Mach-number Perpendicular Shocks. I. Heating Mechanism. *Astrophys. J.*, 851(2):134.
- Ha, J.-H., Ryu, D., and Kang, H. (2018). Properties of Merger Shocks in Merging Galaxy Clusters. *Astrophys. J.*, 857(1):26.
- Hardcastle, M. J. and Croston, J. H. (2005). The Chandra view of extended X-ray emission from Pictor A. *Mon. Not. R. Astron. Soc.*, 363(2):649–660.
- Hardcastle, M. J. and Krause, M. G. (2014). Numerical modelling of the lobes of radio galaxies in cluster environments - II. Magnetic field configuration and observability. *Mon. Not. R. Astron. Soc.*, 443(2):1482–1499.
- Hawley, J. F., Fendt, C., Hardcastle, M., Nokhrina, E., and Tchekhovskoy, A. (2015). Disks and Jets. Gravity, Rotation and Magnetic Fields. *Space Science Reviews*, 191(1-4):441–469.
- Hazeltine, R. D. and Waelbroeck, F. L. (2004). *The framework of plasma physics*. Westview.
- Hillel, S. and Soker, N. (2017). Hitomi observations of Perseus support heating by mixing. *MNRAS*, 466(1):L39–L42.
- Hitomi Collaboration et al. (2016). The quiescent intracluster medium in the core of the Perseus cluster. *Nature*, 535(7610):117–121.
- Hitomi Collaboration et al. (2018). Atmospheric gas dynamics in the Perseus cluster observed with Hitomi. *PASJ*, 70(2):9.
- Huarte-Espinosa, M., Krause, M., and Alexander, P. (2011). 3D magnetohydrodynamic simulations of the evolution of magnetic fields in Fanaroff-Riley class II radio sources. *Mon. Not. R. Astron. Soc.*, 417(1):382–399.

- Hudson, D. S., Mittal, R., Reiprich, T. H., Nulsen, P. E., Andernach, H., and Sarazin, C. L. (2010). What is a cool-core cluster? a detailed analysis of the cores of the X-ray flux-limited HiFLUGCS cluster sample. *Astron. Astrophys.*, 513(6):1–40.
- Jacob, S. and Pfrommer, C. (2017a). Cosmic ray heating in cool core clusters - I. Diversity of steady state solutions. *Mon. Not. R. Astron. Soc.*, 467(2):1449–1477.
- Jacob, S. and Pfrommer, C. (2017b). Cosmic ray heating in cool core clusters - II. Self-regulation cycle and non-thermal emission. *Mon. Not. R. Astron. Soc.*, 467(2):1478–1495.
- Kannan, R., Springel, V., Pakmor, R., Marinacci, F., and Vogelsberger, M. (2016). Accurately simulating anisotropic thermal conduction on a moving mesh. *Mon. Not. R. Astron. Soc.*, 458(1):410–424.
- Kingsland, M., Yang, H. Y. K., Reynolds, C. S., and Zuhone, J. Z. (2019). Effects of Anisotropic Viscosity on the Evolution of AGN Bubbles in Galaxy Clusters.
- Kolmogorov, A. (1941). The Local Structure of Turbulence in Incompressible Viscous Fluid for Very Large Reynolds' Numbers. *Akademii Nauk SSSR Doklady*, 30:301–305.
- Kravtsov, A. V. and Borgani, S. (2012). Formation of galaxy clusters. *Annual Review of Astronomy and Astrophysics*, 50(1):353–409.
- Kuchar, P. and Enßlin, T. A. (2011). Magnetic power spectra from Faraday rotation maps. *Astron. Astrophys.*, 529:A13.
- Kulsrud, R. M. and Ostriker, E. C. (2006). Plasma Physics for Astrophysics. *Physics Today*, 59(1):58.
- Kunz, M. W., Bogdanović, T., Reynolds, C. S., and Stone, J. M. (2012). Buoyancy instabilities in a weakly collisional intracluster medium. *Astrophys. J.*, 754(2).
- Kunz, M. W., Schekochihin, A. A., Cowley, S. C., Binney, J. J., and Sanders, J. S. (2011). A thermally stable heating mechanism for the intracluster medium: Turbulence, magnetic fields and plasma instabilities. *Mon. Not. R. Astron. Soc.*, 410(4):2446–2457.
- Kunz, M. W., Schekochihin, A. A., and Stone, J. M. (2014). Firehose and Mirror Instabilities in a Collisionless Shearing Plasma. *Physical Review Letters*, 112(20):205003.
- Laing, R. A. and Bridle, A. H. (2014). Systematic properties of decelerating relativistic jets in low-luminosity radio galaxies. *Mon. Not. R. Astron. Soc.*, 437(4):3405–3441.
- Lecoanet, D., McCourt, M., Quataert, E., Burns, K. J., Vasil, G. M., Oishi, J. S., Brown, B. P., Stone, J. M., and O'Leary, R. M. (2016). A validated non-linear kelvin-helmholtz benchmark for numerical hydrodynamics. *Mon. Not. R. Astron. Soc.*, 455(4):4274–4288.
- Li, Y., Ruszkowski, M., and Bryan, G. L. (2016). AGN Heating in Simulated Cool-Core Clusters.
- Lloyd, S. (1982). Least squares quantization in pcm. *IEEE Transactions on Information Theory*, 28(2):129–137.
- Longair, M. S. (2011). *High Energy Astrophysics*. Cambridge University Press, third edition.
- McNamara, B. and Nulsen, P. (2007). Heating Hot Atmospheres with Active Galactic Nuclei. *Annu. Rev. Astron. Astrophys.*, 45(1):117–175.
- McNamara, B. R. and Nulsen, P. E. (2012). Mechanical feedback from active galactic nuclei in galaxies, groups and clusters. *New J. Phys.*, 14.
- McNamara, B. R., Nulsen, P. E. J., Wise, M. W., Rafferty, D. A., Carilli, C., Sarazin, C. L., and Blanton, E. L. (2005). The heating of gas in a galaxy cluster by X-ray cavities and large-scale shock fronts. *Nature*, 433(7021):45–47.
- McNamara, B. R., Wise, M., Nulsen, P. E. J., David, L. P., Sarazin, C. L., Bautz, M., Markevitch, M., Vikhlinin, A., Forman, W. R., Jones, C., and Harris, D. E. (2000). [ITAL]Chandra[/ITAL] X-Ray Observations of the Hydra A Cluster: An Interaction between the Radio Source and the X-Ray-emitting Gas. *Astrophys. J.*, 534(2):L135–L138.

- Melville, S., Schekochihin, A. A., and Kunz, M. W. (2016). Pressure-anisotropy-driven microturbulence and magnetic-field evolution in shearing, collisionless plasma. *Mon. Not. R. Astron. Soc.*, 459(3):2701–2720.
- Mendygral, P. J., Jones, T. W., and Dolag, K. (2012). MHD simulations of active galactic nucleus jets in a dynamic galaxy cluster medium. *Astrophys. J.*, 750(2).
- Mendygral, P. J., O'Neill, S. M., and Jones, T. W. (2011). Synthetic observations of simulated active galactic nucleus jets: X-ray cavities. *Astrophys. J.*, 730(2).
- Minati, F. (2014). The matryoshka run: A eulerian refinement strategy to study the statistics of turbulence in virialized cosmic structures. *Astrophys. J.*, 782(1).
- Mittal, R., Hudson, D. S., Reiprich, T. H., and Clarke, T. (2009). AGN heating and ICM cooling in the HIFLUGCS sample of galaxy clusters. *Astron. Astrophys.*, 501(3):835–850.
- Muñoz, D. J., Springel, V., Marcus, R., Vogelsberger, M., and Hernquist, L. (2013). Multidimensional, compressible viscous flow on a moving Voronoi mesh. *Mon. Not. R. Astron. Soc.*, 428(1):254–279.
- Navarro, J. F., Frenk, C. S., and White, S. D. M. (1997). A universal density profile from hierarchical clustering. *The Astrophysical Journal*, 490(2):493–508.
- Nulsen, P. E. J., McNamara, B. R., Wise, M. W., and David, L. P. (2005). The Cluster-Scale AGN Outburst in Hydra A. *Astrophys. J.*, 628(2):629–636.
- Ogiya, G., Biernacki, P., Hahn, O., and Teyssier, R. (2018). Physical and numerical stability and instability of AGN bubbles in a hot intracluster medium.
- O'Neill, S. M., De Young, D. S., and Jones, T. W. (2009). THREE-DIMENSIONAL MAGNETOHYDRODYNAMIC SIMULATIONS OF BUOYANT BUBBLES IN GALAXY CLUSTERS. *Astrophys. J.*, 694(2):1317–1330.
- O'Neill, S. M. and Jones, T. W. (2010). Three-dimensional simulations of bi-directed magnetohydrodynamic jets interacting with cluster environments. *Astrophys. J.*, 710(1):180–196.
- O'Sullivan, E., Giacintucci, S., David, L. P., Gitti, M., Vrtilek, J. M., Raychaudhury, S., and Ponman, T. J. (2011). Heating the hot atmospheres of galaxy groups and clusters with cavities: The relationship between jet power and low-frequency radio emission. *Astrophys. J.*, 735(1).
- Pakmor, R., Bauer, A., and Springel, V. (2011). Magnetohydrodynamics on an unstructured moving grid. *Mon. Not. R. Astron. Soc.*, 418(2):1392–1401.
- Pakmor, R. and Springel, V. (2013). Simulations of magnetic fields in isolated disc galaxies. *Mon. Not. R. Astron. Soc.*, 432(1):176–193.
- Pakmor, R., Springel, V., Bauer, A., Mocz, P., Munoz, D. J., Ohlmann, S. T., Schaal, K., and Zhu, C. (2016). Improving the convergence properties of the moving-mesh code AREPO. *Mon. Not. R. Astron. Soc.*, 455(1):1134–1143.
- Peterson, J. R. and Fabian, A. C. (2006). X-ray spectroscopy of cooling clusters. *Phys. Rep.*, 427(1):1–39.
- Peterson, J. R., Kahn, S. M., Paerels, F. B. S., Kaastra, J. S., Tamura, T., Bleeker, J. A. M., Ferrigno, C., and Jernigan, J. G. (2003). High-Resolution X-Ray Spectroscopic Constraints on Cooling-Flow Models for Clusters of Galaxies. *Astrophys. J.*, 590(1):207–224.
- Pfrommer, C. (2013). Toward a comprehensive model for feedback by active galactic nuclei: New insights from M87 observations by LOFAR, FERMI, and H.E.S.S. *Astrophys. J.*, 779(1).
- Pfrommer, C. (2020). *The Physics of Galaxy Clusters*. Lecture notes summer term 2020. master astrophysics module PHY-765, Potsdam University.
- Pfrommer, C., Chang, P., and Broderick, A. E. (2012). The cosmological impact of luminous TeV blazars. III. Implications for galaxy clusters and the formation of dwarf galaxies. *Astrophys. J.*, 752(1).
- Piffaretti, R., Kaastra, J. S., Jetzer, P., and Tamura, T. (2006). Temperature and entropy profiles of nearby cooling flow clusters observed with XMM-Newton and the effervescent heating model. *Eur. Sp. Agency, (Special Publ. ESA SP*, 2(604):699–704.

- Pizzolato, F. and Soker, N. (2006). On the Rayleigh-Taylor instability of radio bubbles in galaxy clusters. *Mon. Not. R. Astron. Soc.*, 371(4):1835–1848.
- Powell, K. G., Roe, P. L., Linde, T. J., Gombosi, T. I., and De Zeeuw, D. L. (1999). A Solution-Adaptive Upwind Scheme for Ideal Magnetohydrodynamics. *Journal of Computational Physics*, 154(2):284–309.
- Rafferty, D. A., McNamara, B. R., and Nulsen, P. E. J. (2008). The Regulation of Cooling and Star Formation in Luminous Galaxies by Active Galactic Nucleus Feedback and the Cooling-Time/Entropy Threshold for the Onset of Star Formation. *Astrophys. J.*, 687(2):899–918.
- Rafferty, D. A., McNamara, B. R., Nulsen, P. E. J., and Wise, M. W. (2006). The Feedback-regulated Growth of Black Holes and Bulges through Gas Accretion and Starbursts in Cluster Central Dominant Galaxies. *Astrophys. J.*, 652(1):216–231.
- Reynolds, C. S., McKernan, B., Fabian, A. C., Stone, J. M., and Vernaleo, J. C. (2005). Buoyant radio lobes in a viscous intracluster medium. *Mon. Not. R. Astron. Soc.*, 357(1):242–250.
- Richardson, A. S. (2019). 2019 NRL Plasma Formulary. *Nrl*, pages 1–71.
- Rosin, M. S., Schekochihin, A. A., Rincon, F., and Cowley, S. C. (2011). A non-linear theory of the parallel firehose and gyrothermal instabilities in a weakly collisional plasma. *Mon. Not. R. Astron. Soc.*, 413(1):7–38.
- Ruszkowski, M., Enßlin, T. A., Brüggen, M., Heinz, S., and Pfrommer, C. (2007). Impact of tangled magnetic fields on fossil radio bubbles. *Mon. Not. R. Astron. Soc.*, 378(2):662–672.
- Santos, J. S., Rosati, P., Tozzi, P., Böhringer, H., Ettori, S., and Bignamini, A. (2008). Astronomy Astrophysics Searching for cool core clusters at high redshift. *Astron. & Astrophys.*, 483:35–47.
- Scannapieco, E. and Brüggen, M. (2008). Subgrid Modeling of AGN-driven Turbulence in Galaxy Clusters. *Astrophys. J.*, 686(2):927–947.
- Schekochihin, A. A. and Cowley, S. C. (2007). Turbulence and magnetic fields in astrophysical plasmas. *Fluid Mech. its Appl.*, 80:85–115.
- Schekochihin, A. A., Cowley, S. C., Kulsrud, R. M., Hammett, G. W., and Sharma, P. (2005). Plasma Instabilities and Magnetic Field Growth in Clusters of Galaxies. *Astrophys. J.*, 629(1):139–142.
- Schekochihin, A. A., Cowley, S. C., Kulsrud, R. M., Rosin, M. S., and Heinemann, T. (2008). Nonlinear Growth of Firehose and Mirror Fluctuations in Astrophysical Plasmas. *Physical Review Letters*, 100(8):081301.
- Schekochihin, A. A., Cowley, S. C., Rincon, F., and Rosin, M. S. (2010). Magnetofluid dynamics of magnetized cosmic plasma: firehose and gyrothermal instabilities. *Mon. Not. R. Astron. Soc.*, 405(1):291–300.
- Schneider, P. (2015). *Extragalactic Astronomy and Cosmology: An Introduction*. Springer Berlin Heidelberg.
- Schuecker, P., Finoguenov, A., Miniati, F., Böhringer, H., and Briel, U. G. (2004). Probing turbulence in the Coma galaxy cluster. *Astronomy and Astrophysics*, 426:387–397.
- Soker, N. (2016). The jet feedback mechanism (JFM) in stars, galaxies and clusters. *New Astron. Rev.*, 75:1–23.
- Soker, N., Blanton, E. L., and Sarazin, C. L. (2002). Hot Bubbles in Cooling Flow Clusters. *Astrophys. J.*, 573(2):533–541.
- Spitzer, L. (1962). *Physics of Fully Ionized Gases*. Interscience New York, second edition.
- Springel, V. (2010). E pur si muove: Galilean-invariant cosmological hydrodynamical simulations on a moving mesh. *Mon. Not. R. Astron. Soc.*, 401(2):791–851.
- St-Onge, D. A., Kunz, M. W., Squire, J., and Schekochihin, A. A. (2020). Fluctuation dynamo in a weakly collisional plasma.
- Sternberg, A. and Soker, N. (2008). Rising jet-inflated bubbles in clusters of galaxies. *Mon. Not. R. Astron. Soc. Lett.*, 389(1):13–17.

- Subramanian, K., Shukurov, A., and Haugen, N. E. L. (2006). Evolving turbulence and magnetic fields in galaxy clusters. *Mon. Not. R. Astron. Soc.*, 366(4):1437–1454.
- Suzuki, K., Ogawa, T., Matsumoto, Y., and Matsumoto, R. (2013). Magnetohydrodynamic simulations of the formation of cold fronts in clusters of galaxies: Effects of anisotropic viscosity. *Astrophys. J.*, 768(2).
- Ueda, S., Ichinohe, Y., Molnar, S. M., Umetsu, K., and Kitayama, T. (2020). Gas Density Perturbations in the Cool Cores of CLASH Galaxy Clusters. *ApJ*, 892(2):100.
- Vazza, F., Eckert, D., Simionescu, A., Brueggen, M., and Ettori, S. (2013). Properties of gas clumps and gas clumping factor in the intra-cluster medium. *Mon. Not. R. Astron. Soc.*, 429(1):799–814.
- Vernaleo, J. C. and Reynolds, C. S. (2007). Energetic Impact of Jet-Inflated Cocoons in Relaxed Galaxy Clusters. *Astrophys. J.*, 671(1):171–180.
- Vogelsberger, M., Sijacki, D., Kereš, D., Springel, V., and Hernquist, L. (2012). Moving mesh cosmology: Numerical techniques and global statistics. *Mon. Not. R. Astron. Soc.*, 425(4):3024–3057.
- Voigt, L. M. and Fabian, A. C. (2004). Thermal conduction and reduced cooling flows in galaxy clusters. *Mon. Not. R. Astron. Soc.*, 347(4):1130–1149.
- Voit, G. M. (2005). Tracing cosmic evolution with clusters of galaxies arXiv : astro-ph / 0410173v1 7 Oct 2004. *Rev. Mod. Phys.*, 77(April):207–258.
- Voit, G. M. and Donahue, M. (2005). An Observationally Motivated Framework for AGN Heating of Cluster Cores. *Astrophys. J.*, 634(2):955–963.
- Weeren, R. J. V., Rudnick, L., Clarke, T. E., Sebastian, B., Mroczkowski, T., Fabian, A. C., Blundell, K. M., Nyland, K., Sanders, J. S., Peters, W. M., and Intema, H. T. (2020). High-resolution VLA low radio frequency observations of the Perseus cluster : radio lobes , mini-halo and bent-jet radio galaxies. *arXiv*, 17(May):1–17.
- Weinberger, R., Ehlert, K., Pfrommer, C., Pakmor, R., and Springel, V. (2017). Simulating the interaction of jets with the intracluster medium. *Mon. Not. R. Astron. Soc.*, 470(4):4530–4546.
- Weinberger, R., Springel, V., and Pakmor, R. (2020). The AREPO public code release. *The Astrophysical Journal Supplement Series*, 248(2):32.
- Werner, N., Zhuravleva, I., Canning, R. E., Allen, S. W., King, A. L., Sanders, J. S., Simionescu, A., Taylor, G. B., Morris, R. G., and Fabian, A. C. (2016). Deep Chandra study of the truncated cool core of the Ophiuchus cluster. *Mon. Not. R. Astron. Soc.*, 460(3):2752–2764.
- Wise, M. W., McNamara, B. R., Nulsen, P. E. J., Houck, J. C., and David, L. P. (2007). X-Ray Supercavities in the Hydra A Cluster and the Outburst History of the Central Galaxy's Active Nucleus. *Astrophys. J.*, 659(2):1153–1158.
- Worrall, D. (2000). X-Ray-emitting atmospheres of B2 radio galaxies. *Astrophys. J.*, 20.
- Worrall, D. M. (2009). The X-ray jets of active galaxies. *The Astronomy and Astrophysics Review*, 17:1–46.
- Xue, Y. J. and Wu, X. P. (2000). Properties of the double  $\beta$  model for intracluster gas. *Mon. Not. R. Astron. Soc.*, 318(3):715–723.
- Yang, H.-Y. K. and Reynolds, C. S. (2016a). HOW AGN JETS HEAT THE INTRACLUSTER MEDIUM—INSIGHTS FROM HYDRODYNAMIC SIMULATIONS. *Astrophys. J.*, 829(2):90.
- Yang, H.-Y. K. and Reynolds, C. S. (2016b). Interplay Among Cooling, Agn Feedback, and Anisotropic Conduction in the Cool Cores of Galaxy Clusters. *Astrophys. J.*, 818(2):181.
- Zhang, C., Churazov, E., and Schekochihin, A. A. (2018). Generation of internal waves by buoyant bubbles in galaxy clusters and heating of intracluster medium. *Mon. Not. R. Astron. Soc.*, 478(4):4785–4798.
- Zhuravleva, I., Churazov, E., Schekochihin, A. A., Allen, S. W., Arévalo, P., Fabian, A. C., Forman, W. R., Sanders, J. S., Simionescu, A., Sunyaev, R., Vikhlinin, A., and Werner, N. (2014). Turbulent heating in galaxy clusters brightest in X-rays. *Nature*, 515(7525):85–87.

- Zhuravleva, I., Churazov, E., Schekochihin, A. A., Allen, S. W., Vikhlinin, A., and Werner, N. (2019). Suppressed effective viscosity in the bulk intergalactic plasma. *Nat. Astron.*, 3(9):832–837.
- ZuHone, J. A., Markevitch, M., and Zhuravleva, I. (2016). Mapping the Gas Turbulence in the Coma Cluster: Predictions for Astro-H . *Astrophys. J.*, 817(2):110.
- ZuHone, J. A. and Roediger, E. (2016). Cold fronts: Probes of plasma astrophysics in galaxy clusters. *J. Plasma Phys.*, 82(3).
- Zwicky, F. (1933). Die Rotverschiebung von extragalaktischen Nebeln. *Helvetica Physica Acta*, 6:110–127.

---

# Acknowledgements

I would like to thank Christoph Pfrommer and Martin Pohl for supervising my thesis. I am especially grateful to Christoph Pfrommer for making this thesis possible and giving me the opportunity to work at the AIP.

I am very thankful to Thomas Berlok for his insightful support during the entire project while giving me encouraging words and helpful feedback, enduring countless meetings, guiding me in useful discussions, having patience in explaining details and showing insistence to keep my motivation.

I would like to thank Kristian Ehlert for sharing with me his Python scripts on how to implement the turbulent magnetic field and how to analyse the final HDF5 snapshots of my simulations. I could come into his office at any time to ask for help and he never evaded the following journey down the rabbit hole of *AREPO*.

I would like to thank Joseph Whittingham, Alexander Scherrmann and Fabian Emmerich for being cheerful fellow students, having friendly conversations and giving me support when needed or inviting me over.

I would like to thank the entire Cosmology group at the AIP for providing interesting talks and meetings. I have always been amazed by the profound interdisciplinary knowledge all of you have about the most difficult topics in astrophysics.

I would like to thank Christian Wohltat for helping me out in spontaneous occasions and solving with me some crucial Matplotlib related issues.

Finally, I would like to thank my family for their continuous support and the Parkour community in Potsdam for the stress releasing trainings.

---

# Statement of Academic Integrity

With this statement I - Oliver Franke - declare, that I have independently completed this Master's thesis titled "Simulating AGN-inflated bubbles with anisotropic viscosity on a moving mesh". The thoughts taken directly or indirectly from external sources are properly marked as such. This thesis was not previously submitted to another academic institution and has also not yet been published.

Potsdam, August 20, 2020

---

Oliver Franke